

Measurement of simplified template cross sections of the Higgs boson produced in association with W or Z bosons in the $H \rightarrow b\bar{b}$ decay channel in proton-proton collisions at $\sqrt{s} = 13$ TeV

A. Tumasyan *et al.**
(CMS Collaboration)

 (Received 9 December 2023; accepted 28 March 2024; published 29 May 2024)

Differential cross sections are measured for the standard model Higgs boson produced in association with vector bosons (W , Z) and decaying to a pair of b quarks. Measurements are performed within the framework of the simplified template cross sections. The analysis relies on the leptonic decays of the W and Z bosons, resulting in final states with 0, 1, or 2 electrons or muons. The Higgs boson candidates are either reconstructed from pairs of resolved b -tagged jets, or from single large-radius jets containing the particles arising from two b quarks. Proton-proton collision data at $\sqrt{s} = 13$ TeV, collected by the CMS experiment in 2016–2018 and corresponding to a total integrated luminosity of 138 fb^{-1} , are analyzed. The inclusive signal strength, defined as the product of the observed production cross section and branching fraction relative to the standard model expectation, combining all analysis categories, is found to be $\mu = 1.15^{+0.22}_{-0.20}$. This corresponds to an observed (expected) significance of 6.3 (5.6) standard deviations.

DOI: [10.1103/PhysRevD.109.092011](https://doi.org/10.1103/PhysRevD.109.092011)

I. INTRODUCTION

The discovery of a Higgs boson (H) with a mass near 125 GeV by the ATLAS [1] and CMS [2,3] Collaborations at the CERN LHC was a major milestone in the understanding of electroweak (EW) symmetry breaking in the standard model (SM) of particle physics [4–9]. Since its observation, most of the Higgs boson production modes and many decay channels predicted by the SM have been measured. In particular, decays of the Higgs boson into the $\gamma\gamma$, ZZ , WW , $\tau\tau$, and $b\bar{b}$ channels have been observed [10–21]. Higgs boson production in association with a top quark-antiquark pair ($t\bar{t}$) [22,23] has also been observed. To date, all the measured properties [24,25] are compatible with the hypothesis that this particle is the Higgs boson predicted by the SM. Evidence for the Higgs boson decaying to a pair of muons has been reported by the CMS Collaboration, which further supports compatibility with the SM hypothesis [26].

For an SM Higgs boson with a mass (m_H) of 125 GeV, the largest Yukawa coupling that is directly accessible by studying a specific Higgs boson decay channel is the coupling between the Higgs boson and b quarks. The

Yukawa couplings to fermions are proportional to the fermion masses. The Higgs boson decay into pairs of b quarks is kinematically allowed, and out of all Higgs boson decay channels, the $H \rightarrow b\bar{b}$ decay has the largest branching fraction. This decay was previously observed by the ATLAS and CMS Collaborations [21,27]. Using the data collected at $\sqrt{s} = 7, 8,$ and 13 TeV in 2011–2017, the CMS measurement of the $H \rightarrow b\bar{b}$ decay in the vector boson (V , $V = W, Z$) associated production mode (VH) had a significance of 4.8 standard deviations over the background-only hypothesis. The corresponding measured signal strength, defined as the production cross section times branching fraction relative to its SM expectation, was $\mu = 1.01 \pm 0.22$. In combination with other production modes, the measured signal strength in the $H \rightarrow b\bar{b}$ channel was 1.04 ± 0.20 , corresponding to an observed significance of 5.6 standard deviations [27].

The large size of the dataset delivered by the LHC between 2016 and 2018 permits both the ATLAS and CMS Collaborations to make detailed measurements of the kinematic properties of VH production using the $H \rightarrow b\bar{b}$ decay channel. The analysis targets the following decay channels of the W or Z boson: $Z \rightarrow \nu\nu$, $W \rightarrow \ell\nu$, and $Z \rightarrow \ell\ell$. These decay modes are referred to as 0-lepton, 1-lepton, and 2-lepton channels, respectively. The leptons considered in the analysis are electrons and muons.

The cross section measurement is performed in exclusive regions of phase space defined according to the type of vector boson, its transverse momentum $p_T(V)$, and the presence of additional jets. A standardized scheme for these

*Full author list given at the end of the article.

Published by the American Physical Society under the terms of the [Creative Commons Attribution 4.0 International license](https://creativecommons.org/licenses/by/4.0/). Further distribution of this work must maintain attribution to the author(s) and the published article's title, journal citation, and DOI. Funded by SCOAP³.

measurement regions, called bins, is given by the definition of simplified template cross sections (STXS) [28,29], which were introduced to reduce the theoretical dependence in the measurements and to allow for a straightforward comparison of theoretical models with the measurements.

While inclusive cross section measurements are suitable for establishing a given decay mode with limited sample size, using the STXS approach allows the kinematic properties of the Higgs boson production to be probed in a model-independent way. The sensitivity to the VH production STXS bins is expected to be dominated by measurements of the $H \rightarrow b\bar{b}$ decay channel. An STXS measurement in this channel was performed by the ATLAS Collaboration with data collected between 2015 and 2018. The corresponding inclusive signal strength was measured to be $1.02^{+0.18}_{-0.17}$ [30].

This paper reports the study of VH production with subsequent $H \rightarrow b\bar{b}$ decay, using the full CMS proton-proton (pp) collision dataset collected in 2016–2018 at $\sqrt{s} = 13$ TeV. The integrated luminosities are 36.3, 41.5, and 59.8 fb^{-1} for the 2016 [31], 2017 [32], and 2018 [33] data-taking periods, respectively, corresponding to a total of 138 fb^{-1} . Unlike in the previous publications [27,34,35], dedicated categories are introduced for topologies that arise when the Higgs boson is highly Lorentz-boosted so that its decay products are reconstructed as a single merged jet. A similar large-radius-jet topology was explored by the ATLAS Collaboration [36].

The paper is organized as follows. A brief description of the CMS detector and the simulated samples used in the analysis is given in Sec. II. The event reconstruction, with particular emphasis on the objects used in the measurement, is described in Sec. III. The trigger-level selection employed in the analysis is given in Sec. IV. The event selection and categorization, as well as the description of the STXS scheme, are documented in Sec. V. The sources of systematic uncertainties included in the measurement are listed in Sec. VI. The analysis strategy and results are discussed in Sec. VII with tabulated versions provided in HEPData [37]. Section VIII provides the summary of the analysis results.

II. THE CMS DETECTOR AND SIMULATED SAMPLES

The central feature of the CMS apparatus is a superconducting solenoid of 6 m internal diameter, providing a magnetic field of 3.8 T. Within the solenoid volume are a silicon pixel and strip tracker, a lead tungstate crystal electromagnetic calorimeter (ECAL), and a brass and scintillator hadron calorimeter (HCAL), each composed of a barrel and two end cap sections. Forward calorimeters extend the pseudorapidity (η) coverage provided by the barrel and endcap detectors. Muons are detected in gas-ionization chambers embedded in the steel flux-return yoke

outside the solenoid. Events of interest are selected using a two-tiered trigger system [38]. The first level, composed of custom hardware processors, uses information from the calorimeters and muon detectors to select events at a rate of around 100 kHz within a fixed time interval of about 4 μs . The second level, known as the high-level trigger, consists of a farm of processors running a version of the full event reconstruction software optimized for fast processing, and reduces the event rate to around 1 kHz before data storage. A more detailed description of the CMS detector, together with a definition of the coordinate system used and the relevant kinematic variables, can be found in Ref. [39].

Several Monte Carlo (MC) event generators are used to simulate signal and background processes. The signal processes contain Higgs bosons, with $m_H = 125$ GeV, produced in association with W or Z bosons. In this analysis, only decays of the W and Z bosons involving muons, electrons, and/or neutrinos are considered. The quark-induced ZH and WH processes are generated at next-to-leading order (NLO) using the POWHEG v2 [40–42] event generator extended with the MINLO procedure [43,44], while the gluon-induced ZH process (denoted $ggZH$) is generated at leading-order (LO) accuracy with POWHEG v2. The diboson processes ZZ , WZ , and WW are simulated with MadGraph 5_aMC@NLO [45] v2.2.2 (v2.4.2) in 2016 (2017 and 2018) simulations at NLO using the FxFx merging scheme [46] with up to two additional partons. For the analysis of 2017 and 2018 data, the same generator with NLO accuracy is used to simulate $W + \text{jets}$ and $Z + \text{jets}$ processes. For the analysis of 2016 data, LO accurate MadGraph simulations with the MLM matching scheme [47] are used to simulate $W + \text{jets}$ and $Z + \text{jets}$ events, in inclusive and b -quark-enriched configurations. Corrections at NLO and next-to-NLO (NNLO) accuracy are applied to the 2016 LO $W + \text{jets}$ and $Z + \text{jets}$ event samples to achieve NNLO precision in shape and normalization. The NLO corrections are derived from simulation, while the NNLO corrections are obtained from theoretical calculations [48]. While the NLO samples provide a more precise modeling of the kinematic properties of the $V + \text{jets}$ processes, and are used for analyzing the 2017 and 2018 datasets, the corrections for the LO samples used in the analysis of the 2016 data are well validated. The production of simulated samples at NLO requires more computing resources than the production of samples at LO, which means the number of events in the NLO samples is limited. Thus, the LO samples are used in the 2016 analysis to reduce the uncertainty in the measurement arising from the limited size of the simulated samples. NLO $V + \text{jets}$ MC samples are produced in nonoverlapping bins in jet multiplicity and $p_T(V)$, which are then merged to maximize the statistical power of the analysis. Two or more samples contributing to overlapping regions of the phase space are reweighted, such that the total cross section of a given process is conserved. The simulated $W + \text{jets}$ and

Z + jets samples at NLO are additionally corrected differentially in the angular momentum separation between jets [$\Delta R(\text{jj})$], in the region $\Delta R(\text{jj}) < 1$. This correction is needed to account for a shape mismodeling observed in the region $\Delta R(\text{jj}) < 1$. The correction improves the agreement between data and the NLO V + jets predictions. The reweighting is derived for V + jets events and is parametrized as flavor-agnostic, hence one single correction is derived for the V + jets processes, regardless of the jet flavor. This flavor-agnostic parametrization is justified because of the observation that the shape corrections are consistent across flavors of additional jets. The simulation-to-data reweighting is propagated to V + jets events in all analysis regions. Shape-altering uncertainties associated with this correction are uncorrelated across analysis channels, and will be discussed in Sec. VI.

Samples of $t\bar{t}$ events, as well as those of single top quark events produced in the t channel, are generated with POWHEG v2. Samples of single top quark events produced in the tW and s channels are generated with POWHEG v1.

The production cross sections used to normalize the simulated samples of signal and V + jets events are rescaled to NNLO quantum chromodynamic (QCD) predictions, inclusively in $p_T(V)$, and NLO EW accuracy, combining the results from Refs. [49–51], VH@NNLO [51,52], and HAWK v2.0 [53] generators, as described in Ref. [28]. The NLO EW correction is applied as a function of $p_T(V)$. The production cross section for $t\bar{t}$ events is calculated at NNLO with next-to-next-to-leading-logarithmic (NNLL) precision obtained using TOP++ v2.0 [54]. The parton distribution functions (PDFs) used to produce the NLO samples in the 2017–2018 analyses are from the NNLO NNPDF3.1 set [55], while the LO NNPDF3.0 set is used for the LO samples. For parton showering and hadronization, all simulated samples are interfaced with PYTHIA 8.2 [56]. The PYTHIA parameters for the underlying event description correspond to the CUETP8M1 tune for the samples compatible with the 2016 dataset, and to the CP5 tune for the simulation corresponding to the 2017 and 2018 datasets. These tunes were derived in Ref. [57] based on the work described in Ref. [58]. For all processes, the detector response is simulated with a detailed description of the CMS detector, based on the Geant4 package [59]. The event reconstruction is performed with the same algorithms as for data. Additional interactions in the same or nearby bunch crossings, referred to as pileup (PU), are generated with PYTHIA and added to the simulated samples. The simulated events are weighted such that the PU distribution in the simulation matches the one observed in data.

III. EVENT RECONSTRUCTION

Events are reconstructed using a particle-flow (PF) algorithm [60], which aims to reconstruct and identify each individual particle in an event (PF candidate) with an optimized combination of information from the various

elements of the CMS detector. The energy of photons is obtained from the ECAL measurement. The energy of electrons is determined from a combination of the electron momentum at the primary interaction vertex as determined by the tracker, the energy of the corresponding ECAL cluster, and the energy sum of all bremsstrahlung photons spatially compatible with originating from the electron track. The energy of muons is obtained from the curvature of the corresponding track. The energy of charged hadrons is determined from a combination of their momentum measured in the tracker and the matching ECAL and HCAL energy deposits, corrected for the effect of hadronic showers on the calorimeter response. Finally, the energy of neutral hadrons is obtained from the corresponding corrected ECAL and HCAL energies. Events that are found to be affected by reconstruction failures and detector malfunctions are identified and rejected. Correction factors are applied to all reconstructed objects and used to equalize the reconstruction and the identification efficiencies in data and simulation.

The primary vertex (PV) is taken to be the vertex corresponding to the hardest scattering in the event, evaluated using tracking information alone, as described in Ref. [61]. The PV position is reconstructed using tracks clustered with the deterministic annealing algorithm [62]. The reconstructed PV is required to have a z position within 24 cm of the nominal detector center, and a radial position within 2 cm of the beam axis. Displaced tracks originating from b hadron decays are associated with secondary vertices.

W and Z bosons are reconstructed using charged leptons and missing transverse momentum (\vec{p}_T^{miss}). With two opposite-charge, same-flavor leptons, a full Z boson reconstruction is performed, which defines the 2-lepton channel. With one charged lepton and interpreting the missing transverse momentum in the event as the transverse momentum of a neutrino, the transverse momentum of the W boson candidate can be reconstructed, which defines the 1-lepton channel. In events without charged leptons, the large missing transverse momentum is used to estimate the $Z(\nu\nu)$ boson transverse momentum directly. This defines the 0-lepton channel.

Electrons require the matching of a set of ECAL clusters, denoted as superclusters, to a track in the silicon tracker. The electron reconstruction is performed with the Gaussian sum filter algorithm [63]. Electrons are preselected by requiring $p_T > 7$ GeV, $|\eta| < 2.4$, $d_{xy} < 0.05$ cm and $d_z < 0.2$ cm, where d_{xy} and d_z are the transverse and longitudinal impact parameters associated with the electron tracks, respectively.

A tighter identification is then performed using a multivariate approach (MVA ID). In addition, a set of offline requirements on ECAL-based electron quantities is applied. Two selections on the MVA ID discriminant are used, defining two different working points based on the

expected electron identification efficiency of either 90% (loose working point) or 80% (tight working point). The loose working point is used when counting the number of additional leptons beyond the selected muons and electrons in each event, as well as for the event selection of the $Z(ee)H$ channel. The tight working point is required to select events in the $W(e\nu)H$ channel. The electron p_T threshold in the $W(e\nu)H$ channel is 30 GeV. For the $Z(ee)H$ channel, the thresholds are 25 and 17 GeV for the two electrons. The working points and isolation requirements for the 2-lepton channel are generally looser than in the 1-lepton channel because requiring two leptons significantly reduces the background from QCD multijet events. In the 1-lepton channel, tighter requirements are needed to reduce the multijet background. After applying the analysis selection, the QCD multijet background is found to be negligible.

Muons are reconstructed from the combined fit of the tracker and muon detector signals [64]. They are preselected by requiring the following conditions: $p_T > 5$ GeV, $|\eta| < 2.4$, $d_{xy} < 0.5$ cm, $d_z < 1.0$ cm. Two working points corresponding to tight and loose muon identification requirements are utilized to reduce the fraction of other particles misidentified as muons. These working points depend on several of the following identification criteria: the number of hits in the tracker and muon system, the fit quality of the extrapolated muon track, and its consistency with the reconstructed PV. The muon p_T threshold in the $W(\mu\nu)H$ channel is 25 GeV, and 25 and 15 GeV in the $Z(\mu\mu)H$ channel.

The isolation of a lepton is defined relative to its momentum by summing the p_T of PF candidates, excluding the lepton itself, in geometrical cones around the lepton track direction at the event vertex. The cone size is expressed in terms of $\Delta R = \sqrt{(\Delta\phi)^2 + (\Delta\eta)^2}$, where $\Delta\phi$ ($\Delta\eta$) is the difference in the azimuthal angle (pseudorapidity) from the center of the cone to its edge. The lepton isolation criteria reject most of the major background consisting of nonprompt leptons produced in jets. The isolation cone for muons and electrons is $\Delta R = 0.3$, and the ratio of the sum of each particle's p_T within the cone to the lepton p_T must be smaller than 0.06.

Jets are reconstructed from PF candidates using the anti- k_T clustering algorithm with a distance parameter of 0.4 (AK4 jets) [65]. Jet momentum is determined as the vectorial sum of all particle momenta in the jet, and is found from simulation to be, on average, within 5–10% of the true momentum over the entire p_T spectrum and detector acceptance.

Pileup interactions can contribute additional tracks and calorimetric energy depositions to the event, increasing the apparent jet momentum. To mitigate this effect, tracks identified to be originating from PU vertices are discarded and an offset correction [65] is applied to correct for remaining contributions.

Jet energy corrections are derived from simulation studies so that the average measured energy of jets is equal to that of particle-level jets. In situ measurements of the momentum balance in dijet, photon + jet, Z + jet, and multijet events are used to determine any residual differences between the jet energy scale (JES) in data and simulation, and appropriate corrections are made [65]. Additional selection criteria are applied to each jet to remove jets potentially dominated by instrumental effects or reconstruction failures. Jets that overlap geometrically ($\Delta R < 0.4$) with preselected electrons or muons are discarded. Only jets with $|\eta| < 2.5$ are considered. In the WH and $Z(\nu\nu)H$ channels, a minimum threshold of jet $p_T > 25$ GeV is used, while a looser selection ($p_T > 20$ GeV) is applied in the $Z(\ell\ell)H$ channel.

The jet energy resolution (JER) is about 15–20% at 20 GeV, 10% at 100 GeV, and 5% at 1 TeV, and the jet energies in simulation are smeared to ensure their resolutions match those of jets in data [65].

Jets from final-state radiation (FSR), exceeding 20 GeV in momentum and fulfilling jet quality criteria are recovered by an FSR recovery algorithm, which adds the momenta of jets close to the Higgs boson candidate in the dijet mass calculation. The FSR recovery algorithm is applied to all analysis channels.

A reweighting of the additional jet multiplicity spectrum in simulation is applied to the NLO W + jets and Z + jets samples used in the analysis of the 2017 and 2018 datasets. Here, additional jets are those jets that are retained in the analysis selection, but that do not stem from the Higgs boson candidate decay. This reweighting of the additional jet multiplicity is parametrized as a function of $p_T(V)$ and achieves improved modeling of the observed additional jet multiplicity distribution from simulation compared to data. Several shape-altering systematic uncertainties are associated with this reweighting, which will be discussed in Sec. VI.

Jets that originate from the hadronization of b quarks are identified by means of an algorithm based on a deep neural network (DNN), named DEEPCSV [66]. This DNN has several probability outputs for jets resulting from quarks of different flavors. The algorithm provides a continuous discriminant output combining the information from track impact parameters and identified secondary vertices within jets, and from low- p_T leptons produced by heavy-flavor quark decays present in the jet. A jet with a DEEPCSV discriminant value above a certain threshold is considered to be from the decay of a b hadron, called a b -tagged jet. The efficiency for tagging b jets and the rate at which other jets are misidentified as b jets depend on the chosen threshold of the DEEPCSV discriminant. The efficiency and the misidentification rate are both parametrized as functions of the jet p_T and η . The loose (tight) threshold has the highest (lowest) efficiency for tagging b jets, while allowing the most (least) contamination from light, i.e., u ,

d , s , and gluon (g) jets, as well as c jets. The working points are defined such that a specific target for the misidentification (mistag) rate is achieved: 10, 1.0, and 0.1% for the loose, medium, and tight working points, respectively. Each channel is optimized separately, and results in the same selection: the leading b jet candidate in b tagging discriminant score must pass the medium identification working point of the DEEPCSV algorithm. For the next-to-highest b tagging discriminant score (subleading) b jet candidate, the optimal selection requires the loose working point of the DEEPCSV discriminant. Along with these two b -tagged jets associated with the Higgs boson candidate reconstruction, additional b -tagged jets can be present in the event. These jets are included in the analysis as discussed in Sec. V. The b tagging selections for all three channels will be discussed in more detail in Sec. V.

Some b tagging inputs are used in the training of the multivariate discriminants employed in the analysis signal region (SR) to separate signal from background events. The b tagging discriminant is corrected to equalize the efficiency in data and simulation as a function of the b tagging score and the kinematic properties of each jet. An index with an integer value between 0 and 3 referring to the b tagging working point requirement that the jet fulfills is used as one of the inputs for deriving the signal-versus-background discriminants.

The dijet invariant mass resolution is computed by applying a multivariate regression analysis using a DNN trained on simulated b jets stemming from $t\bar{t}$ events [67]. The training includes input features that describe the jet energy and direction, as well as properties of the secondary vertices of the jets. Information about tracks associated with jets, jet constituents, low- p_T electrons and muons in the jet associated with semileptonic B hadron decays is also used. The b jet energy regression improves the precision of the jet four-vectors, which leads to a 10%–15% improvement in the dijet invariant mass resolution, depending on the p_T of the reconstructed Higgs boson candidate. The momenta of the Higgs boson candidate jets are corrected by the application of the b jet energy regression described above, unless otherwise specified. After the application of the regression, a dedicated smearing is applied to the b jet energy so that the dijet invariant mass resolution in simulation will match the performance in data. The smearing parameters are extracted in events where a jet recoils against a Z boson that decays into leptons. Because the Z boson p_T is balanced with the jet p_T , and given that the lepton momentum measurement is precise, the ratio of the reconstructed jet momentum (p_T^j) to the Z boson momentum ($p_T^{\ell\ell}$) enables a precise measurement of the jet momentum and energy. The distribution of the energy difference between the p_T balance procedure and the b jet energy regression is used to estimate the b jet energy regression scale and resolution corrections and

uncertainties. The selected events are divided into four regions of $\alpha = p_T^j/p_T^{\ell\ell}$, and this procedure is applied in each α bin.

In signal events where the Higgs boson has a p_T exceeding 250 GeV, two jets reconstructed with the AK4 clustering [68] algorithm will begin to overlap as the opening angle between the jets shrinks. Therefore, these events are reconstructed using a single large radius of 0.8, producing what are termed AK8 jets. The modified mass drop tagger algorithm (soft-drop algorithm) [69] is applied to remove soft and wide-angle radiation. This algorithm identifies two hard AK4 subjets within the AK8 jet. The mass of the AK8 jet, upon application of the soft-drop algorithm (m_{SD}), is used as discriminating variable in the analysis. The four-momenta of the two subjets are used to calculate the kinematic properties of their corresponding AK8 jet.

The DEEPAK8 algorithm [70] is used to tag boosted $H \rightarrow b\bar{b}$ topologies, exploiting AK8 jet ($\Delta R = 0.8$) reconstruction. The tagger architecture is based on a set of convolutional kernels spanning multiple candidates. It makes use of a multioutput feed-forward neural network with low-level input features (PF candidates), in addition to the traditional observables of the boosted-jet environment (tracks, jets, and secondary vertices).

Ten features for each charged and neutral PF candidate are passed to one of these convolutional kernels, ordered in candidate momentum, to learn the jet substructure. The flavor content of the jet is learned by two other kernels. One of these uses only charged constituents of the jet, sorted by the displacement with respect to the PV, while the other one uses secondary vertices. The DEEPAK8 algorithm is decorrelated from the mass of the AK8 jet, which is included in the training of the network. The level of decorrelation is such that no accumulation of events in mass is observed even for very small values of the background mistag rate. This means that the AK8 jet mass shape associated with the background does not become similar to that of the signal after selection with the DEEPAK8 tagger. The DEEPAK8 algorithm aims to classify a variety of resonances in multiple decay modes. It provides separation for the Lorentz-boosted $H \rightarrow b\bar{b}$ signal against several background outputs: merged light jets, top quark jets, and QCD multijets. Scale factors are used to correct the simulation to account for differences in efficiency with respect to the data. These scale factors are measured in highly-boosted gluon splitting into $b\bar{b}$ events. They are applied to the $H \rightarrow b\bar{b}$ boosted signal output node. The scale factors are parametrized as a function of the AK8 jet p_T and η , and are available for two working points, as discussed in Sec. V.

The value of \vec{p}_T^{miss} is crucial in the reconstruction of the $W \rightarrow \ell\nu$ and $Z \rightarrow \nu\nu$ decays. The \vec{p}_T^{miss} is computed as the negative vector \vec{p}_T sum of all the PF candidates in an event, and its magnitude is denoted as p_T^{miss} [71]. The calculation

of \vec{p}_T^{miss} is modified to account for corrections to the energy scale of the reconstructed jets in the event. Track-based missing transverse momentum, denoted as $p_{T,\text{trk}}^{\text{miss}}$, is also used in the analysis. Only tracks that have a p_T above a minimum momentum threshold (2 GeV) and an impact parameter consistent with the PV are considered in the vectorial sum. The tracks are also required to pass quality requirements, which were designed to limit the contribution from misreconstructed tracks. The estimation of \vec{p}_T^{miss} in simulated events is improved by correcting it for the difference between raw and calibrated jets, including scale and resolution corrections. In addition, a set of recommended filters to remove known issues related to instrumental noise and problematic events is applied [71].

In background event topologies, such as $t\bar{t}$ events, there is additional low-energy jet activity in the event (soft jets). A collection of additional tracks (or PF candidates) is built by requiring $p_T > 300$ MeV, $d_z < 2$ mm, a “high-purity” quality identification, and not be associated with either the leptons from the vector boson decay nor with the two selected b -tagged jets in the event. A collection of soft jets is clustered from these tracks using the anti- k_T clustering algorithm with a distance parameter of $\Delta R < 0.4$. The soft activity with a p_T threshold at 5 GeV is used as a discriminant variable for analysis channels where its modeling in simulation is satisfactory, both in the resolved and boosted topologies, as discussed in Sec. V.

IV. TRIGGER-LEVEL SELECTION

Several triggers are used to collect events containing final-state particles consistent with the signal processes considered. The trigger selection focuses on the final state of the W or Z boson produced in association with the Higgs boson. The triggers used to select events in the 0-lepton channel make use of p_T^{miss} and missing hadronic transverse momentum, H_T^{miss} . These quantities are derived from the reconstructed objects as identified by the PF algorithm. Online, H_T^{miss} is defined as the magnitude of the negative vector \vec{p}_T sum of all reconstructed jets with $p_T > 20$ GeV and $|\eta| < 2.5$. The main triggers used in each of the data-taking periods require the same threshold on p_T^{miss} and H_T^{miss} . This threshold is 110 GeV in 2016, and 120 GeV in the 2017 and 2018 data-taking periods. In the 1-lepton channel, single-lepton triggers are used. The p_T threshold for electrons is 27 GeV in the 2016 data-taking period, rising to 32 GeV in 2017–2018. For muons, the p_T threshold is 24 GeV in the 2016 and 2018 data-taking periods, and is increased to 27 GeV in 2017. Dilepton triggers are used to select events in the 2-lepton channel. The p_T thresholds for electrons are 23 and 12 GeV in all data-taking periods. For muons, the p_T thresholds are 17 and 8 GeV in all data-taking periods; the triggers used in 2017 and 2018 differ from those used in 2016 by the additional requirement that the dimuon invariant mass must

be greater than 3.8 GeV. In addition to the p_T thresholds, the triggers require the leptons to pass stringent identification criteria. The trigger-level leptons are also required to be isolated from other tracks and energy deposits in the calorimeters.

V. EVENT SELECTION AND MULTIVARIATE DISCRIMINANTS FOR SIGNAL EXTRACTION

Though there are numerous features that differ between the three lepton channels and the $b\bar{b}$ reconstruction topologies, a unified analysis strategy is used.

Three control regions (CRs), each enriched in one of the three primary backgrounds: $t\bar{t}$, V + light-quark jets, and V + b jets, are defined for every channel and b quark reconstruction topology. The jet flavor in the V + jets processes (V + $b\bar{b}$ jets, V + b jets, V + c jets and V + light-quark jets) is defined based on the presence of the corresponding hadrons at generator-level with transverse momentum exceeding 25 GeV and $|\eta| < 2.5$. Templates derived from simulation are fitted to the data with the normalizations of the three primary backgrounds left unconstrained and incorporating several systematic uncertainties that are allowed to modify the shapes. The SRs are defined by requiring the dijet invariant mass to be in the range 90–150 GeV and making a relatively tight selection on the multivariate quark flavor discriminant that target two b quarks. The selection values on the multivariate quark flavor discriminants for the SR definitions are reported in Tables I–III for the 0-lepton, 1-lepton, and 2-lepton channels, respectively. The fitted observables in the SRs are all DNN outputs, binned such that all bins contain roughly equal expected signal yields. The observables used in the CRs vary between the channels, and are selected to constrain particular features of the background model. All SRs and CRs are fitted simultaneously to extract the background shapes, background normalizations, and signal strengths.

The requirement of an identified boosted W or Z bosons in the signal events suppresses backgrounds from QCD multijet events, while also providing an efficient trigger path when the W or Z boson decays to charged leptons. Requiring a large boost provides additional advantages. It further reduces the large backgrounds from W and Z production in association with jets, helps to suppress the large background from top quark production in the signal channels including neutrinos, and generally improves the invariant mass resolution of the reconstructed Higgs boson candidates. Therefore, in addition to the analysis targeting *resolved* events where the b jets from the decay of the Higgs boson candidate are reconstructed as separate AK4 jets, we also include *boosted* events where the b jets from the decay of the Higgs boson candidates are both contained in a large-radius jet reconstructed with the AK8 algorithm.

The boosted analysis only considers events with $p_T(V) > 250$ GeV. The SRs and CRs for these analyses

TABLE I. Definition of the SR and CRs for the resolved selection in the 0-lepton channel. If the same selection is applied in all SRs and CRs, this is indicated by the \div symbol in the latter. If no selection is applied, this is indicated by the \dots symbol. The $M(\text{jj})$ and momenta variables have units of GeV.

Variable	SR	$Z + b$ jets	$Z + \text{light-quark jets}$	$t\bar{t}$
Common selection:				
$\min(p_T^{\text{miss}}, H_T^{\text{miss}})$	>100	\div	\div	\div
p_T^{miss}	>170	\div	\div	\div
$p_T(j_1)$	>60	\div	\div	\div
$p_T(j_2)$	>35	\div	\div	\div
$p_T(\text{jj})$	>120	\div	\div	\div
$\Delta\phi(Z, \text{jj})$	>2.0	\div	\div	\div
$\Delta\phi(\vec{p}_T^{\text{miss}}, j)$	>0.5	\div	\div	\div
SR/CR difference:				
N_{aj}	<2	<2	<2	≥ 2
$M(\text{jj})$	$\in [90-150]$	$\notin [90-150]$ and <250	<250	<250
$\text{btag}(j_1)$	$>\text{medium}$	$>\text{medium}$	$<\text{medium}$	$>\text{medium}$
$\text{btag}(j_2)$	$>\text{loose}$	$>\text{loose}$	$<\text{loose}$	$>\text{loose}$
$\Delta\phi(\vec{p}_T^{\text{miss}}, \vec{p}_T^{\text{miss, trk}})$	<0.5	<0.5	<0.5	\dots
$\min \Delta\phi(\vec{p}_T^{\text{miss}}, j)$	\dots	\dots	\dots	$<\pi/2$

TABLE II. Definition of the SR and CRs for the resolved selection of the 1-lepton, channel. If the same selection is applied in all SRs and CRs, this is indicated by the \div symbol in the latter. If no selection is applied, this is indicated by the \dots symbol. The $M(\text{jj})$ and momenta variables have units of GeV.

Variable	SR	$W + b$ jets	$W + \text{light-quark jets}$	$t\bar{t}$
Common selection:				
$p_T(\text{jj})$	>100	\div	\div	\div
$p_T(V)$	>150	\div	\div	\div
N_{al}	<1	\div	\div	\div
$p_T(j_1)$	>25	\div	\div	\div
$p_T(j_2)$	>25	\div	\div	\div
$\Delta\phi(\text{lep}, \vec{p}_T^{\text{miss}})$	<2	\div	\div	\div
SR/CR difference:				
$\text{btag}(j_1)$	$>\text{medium}$	$>\text{medium}$	$[\text{loose-medium}]$	$>\text{tight}$
$\text{btag}(j_2)$	$>\text{loose}$	$>\text{loose}$	\dots	\dots
$M(\text{jj})$	$\in [90-150]$	$\in [150-250]$ and <90	<250	<250
N_{aj}	<2	<2	\dots	≥ 2
$\frac{p_T^{\text{miss}}}{\sigma(p_T^{\text{miss}})}$	>2	>2	>2	\dots
$\Delta\phi(W, \text{jj})$	>2.5	>2.5	\dots	\dots

TABLE III. Definition of the SR and CRs for the resolved selection in the 2-lepton channel. If the same selection is applied in all SRs and CRs, this is indicated by the \div symbol in the latter. If no selection is applied, this is indicated by the \dots symbol. The $M(\text{jj})$, $M(V)$, and momenta variables have units of GeV.

Variable	SR	$Z + b$ jets	$Z + \text{light-quark jets}$	$t\bar{t}$
$p_T(V)$	>75	\div	\div	\div
$\text{btag}(j_1)$	$>\text{medium}$	$>\text{medium}$	$<\text{loose}$	$>\text{tight}$
$\text{btag}(j_2)$	$>\text{loose}$	$>\text{loose}$	$<\text{loose}$	$>\text{loose}$
$M(V)$	$\in [75-105]$	$\in [85-97]$	$\in [75-105]$	$\in [10-75]$ and >120
$M(\text{jj})$	$\in [90-150]$	$\notin [90-150]$ and <250	$\in [90-150]$	<250
$\Delta\phi(Z, \text{jj})$	>2.5	>2.5	>2.5	\dots

are optimized separately for the three analysis channels (0-, 1-, and 2-lepton). Sections VB and VC describe the main features of the resolved and boosted analyses.

Some of the events with $p_T(V) > 250$ GeV can be reconstructed in both the resolved and boosted topologies. We refer to these as overlap events in what follows. There are four categories that overlap events can enter, depending on whether they are resolved or boosted, and whether they belong to the SRs or the CRs. By studying all possible permutations in simulation, the following priority ranking was selected: resolved SRs, boosted SRs, resolved CRs, and boosted CRs. The reason for this choice is that the resolved SRs provide more sensitivity, gauged as the uncertainty in the signal strength extracted using an Asimov dataset, to the signal than the boosted SRs. Overlap events that would be placed either in a resolved CR or a boosted SR are assigned to the boosted SR to improve the sensitivity of the analysis. This ranking minimizes the expected uncertainties in the STXS measurements and ensures that events satisfying both resolved and boosted selection criteria are used only once.

A. Subcategorization in STXS bins

In all channels, additional subcategorizations are employed to maximize the signal sensitivity to the different STXS bins. The STXS categorization employed in the analysis is shown in Fig. 1. The STXS binning for the V (leptonic)H process [29] uses a division into three production modes: WH , $q\bar{q} \rightarrow ZH$, and $gg \rightarrow ZH$. For each of these production modes, the STXS classification defines bins in $p_T(V)$: $[0, 75)$, $[75, 150)$, $[150, 250)$, $[250, 400)$, >400 GeV.

The $[150, 250)$ GeV $p_T(V)$ STXS bin is split into two; one bin without any additional jets and another bin with additional jets. This categorization constitutes the STXS

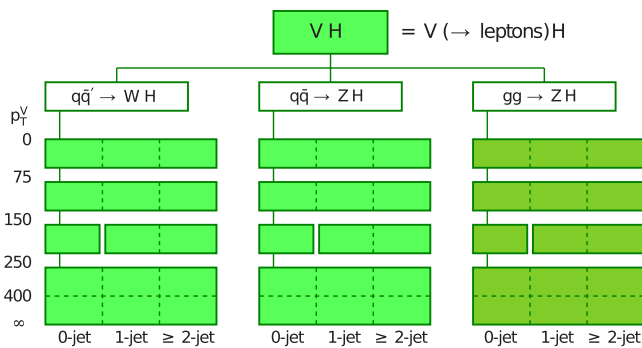


FIG. 1. Overview of the STXS bins for the three VH production modes [29]. The vertical axis reflects the $p_T(V)$ bin ranges and the horizontal axis the number of additional jets. The general bin definitions are indicated by the green boxes. No distinction is made between gluon- and quark-induced production modes in the analysis. As mentioned in Sec. VA, some STXS bins are not explicitly targeted by the analysis: contributions from these bins are fixed to their SM expectations.

classification, that is, the generator-level division of events into STXS bins. Not all of these bins are accessible in the analysis. The gluon- and quark-induced ZH production modes are merged because the sensitivity to the separate processes is small with the currently available dataset. In addition, the two exclusive jet bins for the WH process are merged because of the low sensitivity to the bin with additional jets. Apart from bins that are merged, there are also STXS bins that are not within the analysis selection acceptance. This concerns the lowest $p_T(V)$ bin, $[0, 75)$ GeV, for all production processes, and the $[75, 150)$ GeV bin for the WH process. Negligible contributions from these bins can appear in the analysis because generator-level quantities used to define the STXS bins do not exactly match their reconstruction-level equivalents. Where these bins do contribute to the analysis, their rates are fixed to the SM expectations. To target the STXS bins, we define corresponding reconstruction-level categories, constituting the subcategorization of the five channels considered in the measurement.

- (i) For the 0-lepton channel, we define three categories in reconstructed $p_T(V)$: $[75, 250]$ GeV, $[250, 400)$ GeV, and > 400 GeV.
- (ii) For the 2-lepton channel, we define four categories in reconstructed $p_T(V)$: $[75, 150)$ GeV, $[150, 250)$ GeV, $[250, 400)$ GeV, and > 400 GeV.
- (iii) In the 0- and 2-lepton channels, the $150 < p_T(V) < 250$ GeV category is further subdivided into a subcategory without any additional jets and another with at least one additional jet.
- (iv) For the 1-lepton channel, we define three categories in reconstructed $p_T(V)$: $[150, 250)$ GeV, $[250, 400)$ GeV, and > 400 GeV. There is no further subdivision into additional jet categories.

B. Analysis of the resolved jet topology

1. Analysis of the 0-lepton channel

The event topology of the 0-lepton channel is characterized by the presence of large p_T^{miss} due to the $Z \rightarrow \nu\bar{\nu}$ decay and a pair of b jets from the Higgs boson decay recoiling against the Z . Additional jet activity (N_{aj}) is expected to be low, and no high- p_T leptons should be present. Events in the 0-lepton channel are selected using the high-level trigger paths described in Sec. IV. The p_T^{miss} is required to be larger than 170 GeV. As a result of the trigger acceptance, we require $\min(p_T^{\text{miss}}, H_T^{\text{miss}})$ to exceed 100 GeV. The Higgs boson candidate is reconstructed using the two jets with $|\eta| < 2.5$ that have the highest b tagging score. The leading and subleading b jet associated with the Higgs boson candidate, denoted with the suffixes j_1 and j_2 , must have $p_T > 60$ and 35 GeV, respectively. Since the Higgs boson recoils against the Z boson, we require the difference in azimuthal angle between the jj system and the Z boson to satisfy $\Delta\phi(Z, jj) > 2.0$. We also

demand the invariant mass of the dijet system to be in the range 50–500 GeV and have $p_T > 120$ GeV. Events containing at least one isolated lepton with $p_T > 15$ GeV in the central region ($|\eta| < 2.5$) are rejected. To reduce the QCD multijet background, a requirement of $\Delta\phi(\vec{p}_T^{\text{miss}}, j) > 0.5$ is applied for all jets with $p_T > 30$ GeV for both the SR and CRs. This means that events with any energetic jets close to \vec{p}_T^{miss} in azimuth are not considered. Events are split into four orthogonal categories, one SR and three CRs. The selections used for the SR, as well as for the CRs enriched in the main background processes ($Z + b$ jets, $Z + \text{light-quark jets}$, and $t\bar{t}$), are summarized in Table I. The notation $\text{btag}(j_1)$ [$\text{btag}(j_2)$] $>$ ($<$) medium (loose) indicates that the b tagging score associated with the leading (subleading) jet of the Higgs boson candidate is required to be larger (smaller) than the medium (loose) b tagging working point.

2. Analysis of the 1-lepton channel

The topology of the 1-lepton, events is characterized by the presence of a single isolated lepton from the decay of the W boson recoiling against two b jets from the decay of the Higgs boson. The presence of a single isolated lepton provides a trigger path for this channel. The Higgs boson is reconstructed using the two jets, with $p_T > 25$ GeV, that have the highest b tag scores, denoted with the suffixes j_1 and j_2 . Only jets with $|\eta| < 2.5$ are considered. We require the Higgs and W boson candidates to have $p_T > 100$ and 150 GeV, respectively. An additional requirement on the ratio of p_T^{miss} to its uncertainty, $p_T^{\text{miss}}/\sigma(p_T^{\text{miss}})$, is applied to the CRs enriched in $W + b$ and $W + \text{light-quark jets}$ as well as to the SR. Events are not considered if they contain additional leptons (N_{al}) with $|\eta| < 2.5$ and $p_T > 25$ GeV. The selected events are split into four orthogonal categories, one SR and three CRs. The selections used for the SR, as well as for the CRs enriched in the main background processes ($W + b$ jets, $W + \text{light-quark jets}$, and $t\bar{t}$), are summarized in Table II. The notation $\text{btag}(j_1)$ [$\text{btag}(j_2)$] $>$ ($<$) loose, medium, or tight indicates that the b tagging score associated with the leading (subleading) jet of the Higgs boson candidate is required to be larger (smaller) than the corresponding loose, medium, or tight b tagging working point. The notation [loose-medium] indicates that the leading jet associated with the Higgs boson candidate is required to have a b tagging score in the range loose–medium b tagging working point.

3. Analysis of the 2-lepton channel

The topology of the signal events in the 2-lepton channel is characterized by the presence of two isolated leptons from the decay of the Z boson, recoiling against two b jets from the decay of the Higgs boson. Figure 2 shows the simulated invariant mass for signal events (without any additional recoiling jet) generated with $m_H = 125$ GeV in

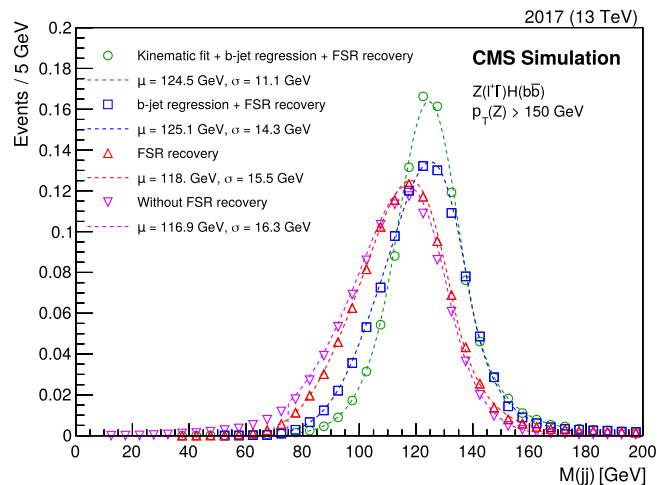


FIG. 2. Dijet invariant mass distributions in samples of simulated (2017 simulation) signal events passing the 2-lepton channel requirements without any additional recoiling jet. Distributions are shown without the usage of the FSR recovery algorithm (purple triangles), before (red triangles) and after (blue squares) the energy corrections from the b jet regression are applied, and when a kinematic fit procedure (green circles) is used in addition to them. The fitted mean and width of the core of the distribution, obtained by fitting a Bukin function [72], are displayed in the figure. The statistical uncertainties are smaller than the marker height.

the 2-lepton channel using the FSR recovery algorithm mentioned in Sec. III, along with the addition of the b jet energy regression (discussed in Sec. III), and a kinematic fit. Since there is no genuine \vec{p}_T^{miss} in the hard-scattering process for this event topology, a kinematic fit is performed to improve the resolution of the dijet invariant mass. In this fit, the mass of the dilepton system is constrained to the Z boson mass (PDG), while the total p_T of all the particles must sum to zero. This kinematic fit imposes a balance between the Z boson p_T , which is expected to be well measured because of the good momentum resolution for high- p_T leptons, and the vectorial sum of the jet momenta. The objects used in the fit are the two b -tagged jets that form the Higgs boson candidate after application of the b jet energy regression, and the FSR recovery algorithm, two lepton candidates, and up to one jet produced by initial-state radiation (ISR). Only jets with $|\eta| < 2.5$ are included in the analysis. As shown in Fig. 2, a large improvement in resolution in the region of the mass peak is achieved when the kinematic fit, the b jet energy regression, and the FSR recovery algorithms are employed together.

The Higgs boson is reconstructed using the two highest b tagging score jets, denoted with the suffixes j_1 and j_2 , that have $p_T > 20$ GeV, and $p_T(V)$ is required to exceed 75 GeV. The selections used to define the SR and CRs, which are enriched in the main background processes ($Z + b$ jets, $Z + \text{light-quark jets}$, $t\bar{t}$) are summarized in Table III. Similarly to the 0- and 1-lepton channels, the $t\bar{t}$

CR is very pure in $t\bar{t}$ events. The additional requirement that the dilepton invariant mass lie in the Z boson mass window ensures the Z + jets purity in the corresponding regions is high. The notation $\text{btag}(j_1)$ [$\text{btag}(j_2)$] $>$ ($<$) loose, medium, or tight indicates that the b tagging score associated with the leading (subleading) jet of the Higgs boson candidate is required to be larger (smaller) than the corresponding loose, medium, or tight b tagging working point.

4. Multivariate discriminants in the SR and the heavy-flavor CRs

In order to improve the separation between signal and background, a DNN classifier trained to discriminate the VH , $H \rightarrow b\bar{b}$ signal against all background processes is used for all the channels. The same network architecture is used for both the DNN signal/background classifier and the DNN multiclass background classifier discussed later in this section. A DNN classifier with six hidden fully connected layers is trained, with each layer containing 512, 256, 128, 64, 64, and 64 nodes [73]. The final layer is a softmax layer [73], giving the probability for an event to be in a particular

class. The classifier is trained to minimize the cross-entropy loss function [73] using the Adam optimizer algorithm [74] trained on a minibatch of size 1024.

The input features used in the DNN training encompass the kinematic properties of the final state: the masses, momenta, and angles of the jets, dijet, vector boson candidate, and leptons. The additional reconstructed jet multiplicity is also used. While many potentially discriminating variables were considered, variables that did not contribute to the analysis sensitivity were dropped. The modeling of these variables in the simulation is also inspected. When the modeling of such variables is observed to be unsatisfactory, the variables are removed from the input feature list of the DNN training.

The full list of input variables is shown in Table IV for the 0-, 1-, and 2-lepton channels. These variables are used as inputs to the DNN trainings in all the STXS categories in which the DNN trainings are performed separately. To evaluate the recoil jet multiplicity, used as an input variable in the DNN training for the 2-lepton channel, recoil jets are identified as ISR jets. They must have $p_T > 20$ GeV, pass reconstruction quality requirements, and cannot be part of the Higgs boson candidate or one of the FSR jets.

TABLE IV. Input variables used for the DNN training in the resolved SR of the 0-, 1-, and 2-lepton channels. Reconstructed jets associated with the Higgs boson candidate are classified as leading (labeled with suffix j_1) and subleading (labeled with suffix j_2) based on their b tag score.

Variable	Description	0-lepton	1-lepton,	2-lepton
$M(\text{jj})$	Dijet invariant mass	✓	✓	✓
$p_T(\text{jj})$	Dijet transverse momentum	✓	✓	✓
\vec{p}_T^{miss}	Missing transverse momentum	✓	✓	✓
$M_t(V)$	Transverse mass of the vector boson		✓	
$p_T(V)$	Transverse momentum of the vector boson		✓	✓
$p_T(\text{jj})/p_T(V)$	Ratio of transverse momenta of the dijet system and the vector boson		✓	✓
$\Delta\phi(V, \text{jj})$	Azimuthal angle between the vector boson and the dijet directions	✓	✓	✓
$\text{btag}(j_1)$	b tagging score of leading jet	✓	✓	✓
$\text{btag}(j_2)$	b tagging score of subleading jet	✓	✓	✓
$\Delta\eta(\text{jj})$	Pseudorapidity difference between leading and subleading jet	✓	✓	✓
$\Delta\phi(\text{jj})$	Azimuthal angle between leading and subleading jet	✓	✓	✓
$p_T^{\text{max}}(j_1, j_2)$	Maximum transverse momentum of jet between leading and subleading jet	✓	✓	
SA5	Number of soft-track jets with momentum greater than 5 GeV	✓		✓
N_{aj}	Number of additional jets	✓	✓	
$\text{btag}_{\text{max}}(\text{add})$	Maximum b tagging discriminant score among additional jets	✓		
$p_T^{\text{max}}(\text{add})$	Maximum transverse momentum among additional jets	✓		
$\Delta\phi(\text{jet}, \vec{p}_T^{\text{miss}})$	Azimuthal angle between additional jet and \vec{p}_T^{miss}	✓		
$\Delta\phi(\text{lep}, \vec{p}_T^{\text{miss}})$	Azimuthal angle between lepton and \vec{p}_T^{miss}		✓	
M_t	Reconstructed top quark mass		✓	
$p_T(j_1)$	Transverse momentum of leading jet			✓
$p_T(j_2)$	Transverse momentum of subleading jet			✓
$M(V)$	Reconstructed vector boson mass			✓
$\Delta R(V, \text{jj})$	Angular separation between the vector boson and the dijet system			✓
$\Delta R(V, \text{jj})$ (kin)	Angular separation between the vector boson and the dijet system (reconstructed after kinematic fit)			✓
$\sigma(M(\text{jj}))$	Resolution of dijet invariant mass			✓
N_{rec}	Number of recoil jets			✓

Among the most discriminating variables for all channels are $M(jj)$, $p_T(V)$, the number of additional jets, and the angular separation between the two jets forming the Higgs boson candidate. To estimate the feature importance for the DNN training, the classifier is retrained sampling from the distribution of all possible feature combinations. The relative feature importance is defined using the approximate median significance metric [73]. All trainings are repeated 10 times to average out fluctuations from randomized initial weights and the stochastic gradient descent. The mean value of the estimated significance is used to compare with the baseline. In the 2-lepton channel, both regressed variables and variables evaluated after the kinematic fit are employed. The b tagging status of the jets is exploited by using the DEEPCSV working point information. The trainings are performed in categories defined to target particular STXS bins for all channels, and the subsequent evaluation is performed for the same STXS bins. In the 0- and 1-lepton channels, a multiclass DNN (HFDNN) is trained in the heavy-flavor $Z + b$ and $W + b$ CRs, to separate the different $V + \text{jets}$ components (vector boson production associated with light-quark, c , and b jets), single top quark, and $t\bar{t}$ backgrounds. The same input features and DNN architecture as for the signal/background classification are used (as shown in Table IV). Instead of labels for the signal/background classification, the output of the DNN is an m -dimensional vector of probabilities for the m background classes. Figure 3 shows the HFDNN discriminants in the 0- and 1-lepton heavy-flavor CRs, after a maximum likelihood fit to the data. This is a simultaneous fit of all SRs and CRs in the analysis.

The DNN score is used as a discriminating variable in each resolved SR, while different strategies are used in the resolved CRs, as discussed in Sec. VII.

C. Analysis of the large-radius jet topology

The boosted topology is included in the measurement in addition to the resolved analysis and targets the two STXS $p_T(V)$ bins above 250 GeV (i.e., 250–400 GeV and > 400 GeV). In the boosted event categories a single AK8 jet is used to reconstruct the Higgs boson candidate, with the DEEPAK8 $b\bar{b}$ tagging algorithm applied to the Higgs boson candidate decay products. This accounts for the kinematic properties of the event in the region where the two AK4 jets start to overlap.

An important feature of the analysis is the usage of the $b\bar{b}$ tagging algorithm, both as a selection variable to define SR and CRs, and as a discriminating input feature of the MVA discriminant trained in the SR. The output of the discriminant node against light-quark jets of the DEEPAK8 algorithm (DeepAK8bbVsLight) is used in this measurement, since it is observed to provide the highest sensitivity for signal/background separation in the boosted analysis region. The $H \rightarrow b\bar{b}$ boosted signal output node is calibrated by performing data and simulation efficiency

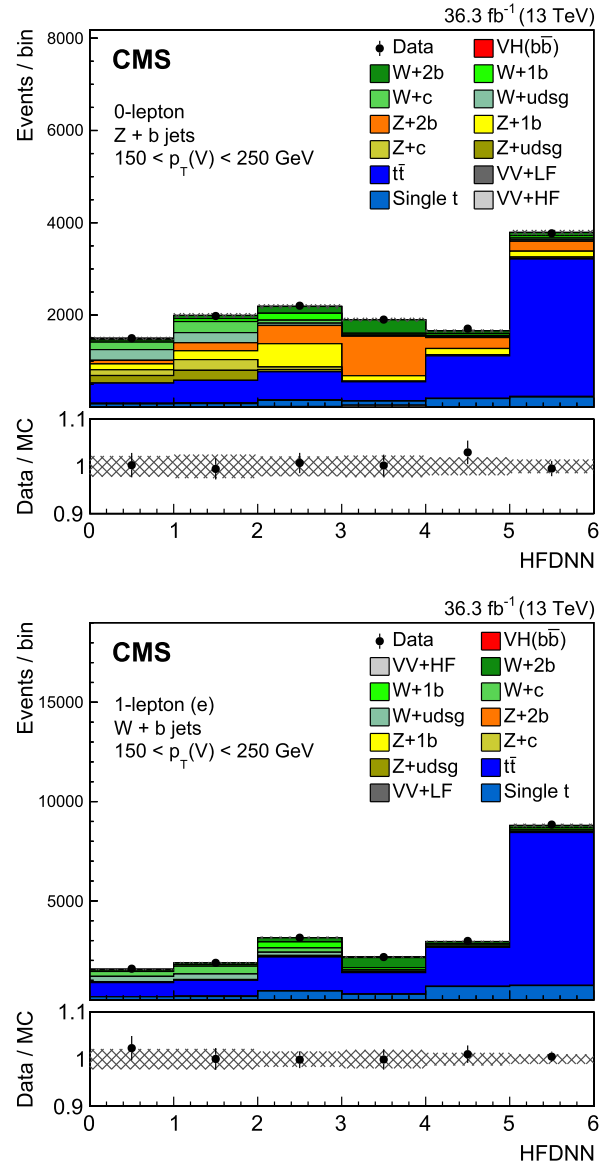


FIG. 3. Distribution of the HFDNN scores in the 0-lepton (upper) and 1-lepton, (lower) $Z + b$ and $W + b$ heavy-flavor CRs for the 2016 dataset, after the fit to data. The output nodes target enrichment in the $V + \text{light-quark}$ (first bin), $V + c$ (second bin), $V + b$ (third bin), $V + b\bar{b}$ (fourth bin), single top quark (fifth bin), and $t\bar{t}$ (sixth bin) backgrounds. The lower plots display the ratio of the data to the MC expectations. The vertical bars on the points represent the statistical uncertainty in the ratio, and the hatched area shows the MC uncertainty.

measurements, as described in Sec. III. The corresponding uncertainties are used as prior constraints in the fit. No external efficiency measurements are available for high-momentum light-quark, c , and b jets stemming from top quark decays. These components are dominant in the $V + \text{light-quark}$ jets, $V + b$ jets, and $t\bar{t}$ analysis CRs. Therefore, the normalizations of these processes are extracted *in situ* in the combined fit by including

unconstrained parameters that scale the normalizations of these processes in the CRs, as discussed in Sec. VII.

The SRs and CRs for the 0-, 1-, and 2-lepton channels are defined separately. In addition to the application of the baseline event selection defining the lepton channels discussed in Sec. VB for the resolved analysis, the common preselection valid for all channels in the large-radius jet topology requires $m_{SD} > 50$ GeV, $p_T(H) > 250$ GeV, and $p_T(V) > 250$ GeV. Only jets with $|\eta| < 2.5$ are considered. We define three CRs, enriched in the main background processes ($V + b$ jets, $V +$ light-quark jets, and $t\bar{t}$), and one SR for the extraction of the boosted $H \rightarrow b\bar{b}$ signal. To enrich the SR and CRs in $t\bar{t}$ and $V + b$ jets processes, the DEEPAK8 discriminant must be larger than 0.8. For the light-quark jets region, the complementary requirement (< 0.8) is used. The value of 0.8 was optimized to retain most of the signal while minimizing the background contamination. In the 0- and 1-lepton channels, events in the $t\bar{t}$ CRs are selected if they have at least one AK4 b -tagged jet, identified using the medium DEEPCSV working point. No additional leptons are allowed in SR and CRs. The dijet soft-drop mass must be in the range 90–150 GeV for the SR, outside this range for the $V + b$ jets CR, and above 50 GeV for the $V +$ light-quark jets and $t\bar{t}$ CRs. Since all of the Z boson decay products are visible in the 2-lepton final state, $M(V)$ must be in the range 75–105 GeV for the SR, $Z + b$ jets, and $Z +$ light-quark jets CRs, and outside this range for the $t\bar{t}$ CR. Table V summarizes the SR and CR selections in the boosted analysis.

1. Multivariate discriminant in the SR for the boosted topology

Boosted decision trees (BDTs) were trained in the SRs for the 0-, 1-, and 2-lepton channels to separate the boosted

Higgs boson decay signal from the sum of all background processes. Input variable optimizations, as well as over-training checks, were performed. The input features of the BDT training take into account the kinematic properties of the event and include observables related to the AK8 jet candidate, such as its soft-drop mass and p_T . The invariant mass of the dijet system, as well as additional variables used for the DNN training in the resolved topology, are also added for events in the overlap region between the boosted and resolved analyses. For purely boosted events, these variables are set to default values in the BDT training and are not considered further. This training strategy is found to improve the BDT sensitivity by approximately 25% as a result of the very good $M(jj)$ resolution. Additionally, the properties of the reconstructed vector boson recoiling against the Higgs boson candidate, and the DEEPAK8 output node against light-quark-jet discrimination, are used as inputs in the training. The inclusion of the DEEPAK8 discriminant in the BDT training leads to an improvement of around 30% in the expected sensitivity in this region. Because the data-to-simulation corrections for the DEEPAK8 tagger are extracted for fixed operating points of the DEEPAK8 discriminant and do not correct the full shape of the output, binned working point values of the discriminant are used in the training instead of its full shape. The definition of the optimal working point used in the training is found from a scan of the expected sensitivity when varying the choice of the DEEPAK8 working point. For each configuration, a dedicated BDT is trained. The BDT score is used as the fitted variable in the boosted SR, while the DEEPAK8 output node is used in the boosted CRs. The $V + b$ jets, $V +$ light-quark jets and $t\bar{t}$ CRs make use of two bins in b tagging score. The bin boundaries correspond to the b tagging working points: [0.8, 0.97, 1]. The $V +$ light-quark jets CR uses two bins in the complementary region, [0, 0.4, 0.8].

TABLE V. Selection criteria for the SR and CRs in the boosted topology for 0-, 1-, and 2-lepton channels. The DeepAK8bbVsLight designation represents the DEEPAK8 discriminant for the light-quark flavor discrimination node. The $M(jj)$ and $M(V)$ variables have units of GeV.

Variable	SR	$V + b$ jets	$V +$ light-quark jets	$t\bar{t}$
0-lepton				
DeepAK8bbVsLight	> 0.8	> 0.8	< 0.8	> 0.8
$M(jj)$	$\in [90-150]$	$\in [50-90]$ or $\in [150-250]$	> 50	> 50
N_{al}	$= 0$	$= 0$	$= 0$	$= 0$
N_{aj}	$= 0$	$= 0$	$= 0$	> 0
1-lepton				
DeepAK8bbVsLight	> 0.8	> 0.8	< 0.8	> 0.8
$M(jj)$	$\in [90-150]$	$\in [50-90]$ or $\in [150-250]$	> 50	> 50
N_{al}	$= 0$	$= 0$	$= 0$	$= 0$
N_{aj}	$= 0$	$= 0$	$= 0$	> 0
2-lepton				
DeepAK8bbVsLight	> 0.8	> 0.8	< 0.8	> 0.8
$M(jj)$	$\in [90-150]$	$\in [50-90]$ or $\in [150-250]$	$\in [90-150]$	> 50
$M(V)$	$\in [75-105]$	$\in [75-105]$	$\in [75-105]$	$\notin [75-105]$

VI. SYSTEMATIC UNCERTAINTIES

Several systematic uncertainties affect the normalizations of the simulated signal and background processes, as well as the shapes of the multivariate discriminants fitted in the SRs.

The theoretical uncertainty in the $H \rightarrow b\bar{b}$ branching fraction is 0.5% [28]. Theoretical uncertainties in the inclusive production cross sections are derived from factorization (μ_F) and renormalization (μ_R) scale variations and amount to 0.7, 0.6, and 25% for the WH , quark-induced ZH , and gluon-induced ZH processes, respectively [28]. Migration uncertainties between the STXS bins are evaluated by studying the effect on the total cross section above each $p_T(V)$ and N_{aj} boundary by varying μ_F and μ_R individually up and down by a factor of two around their default values and neglecting the largest variations. The largest change is used as the absolute uncertainty from this source. This change is then employed to increase the process normalization in STXS bins above the given $p_T(V)$ or N_{aj} boundary, and decreasing it in the bins below. These uncertainties are in the range of 3–11 and 30–40% for the quark- and gluon-induced processes, respectively, depending on the STXS bin considered. The gluon-induced process uncertainty is larger than for the quark-induced process because of the larger bin migration in the former case. Acceptance effects within each STXS bin are taken into account by varying μ_F and μ_R , including a normalization factor to ensure these variations do not change the overall cross section of that particular STXS bin.

Theoretical uncertainties due to the choice of PDFs and the value of the strong coupling constant are derived for each signal and background process following the recommendations given in Ref. [75] and are fully correlated across data-taking years. They are 1.9% for the quark-induced ZH and WH processes, and 2.4% for the gluon-induced ZH process. Uncertainties coming from the variations of μ_F and μ_R are applied to all background processes and are fully correlated across data-taking years. The NLO EW corrections to the ZH and WH processes have a 2% systematic uncertainty [28]. The uncertainties in the diboson and single top quark production cross sections in the high- $p_T(V)$ region are both set to 15%. These uncertainties are derived from CMS measurements of these processes [76,77]. However, they are increased to account for the difference in the phase space between the present analysis and the previous measurement.

The shapes of various distributions of the $V + jet$ processes are derived by comparing simulation to data in control regions. The uncertainties affecting the $V + jets$ processes impact both the process normalization and the shape of the distributions. The reweighting in the number of additional jets, discussed in Sec. III, is derived from the data-to-simulation ratio in the 2-lepton $Z + b$ CR as a function of the number of additional jets and $p_T(V)$, which is shown in Fig. 4 (left panel). The full value of the weight

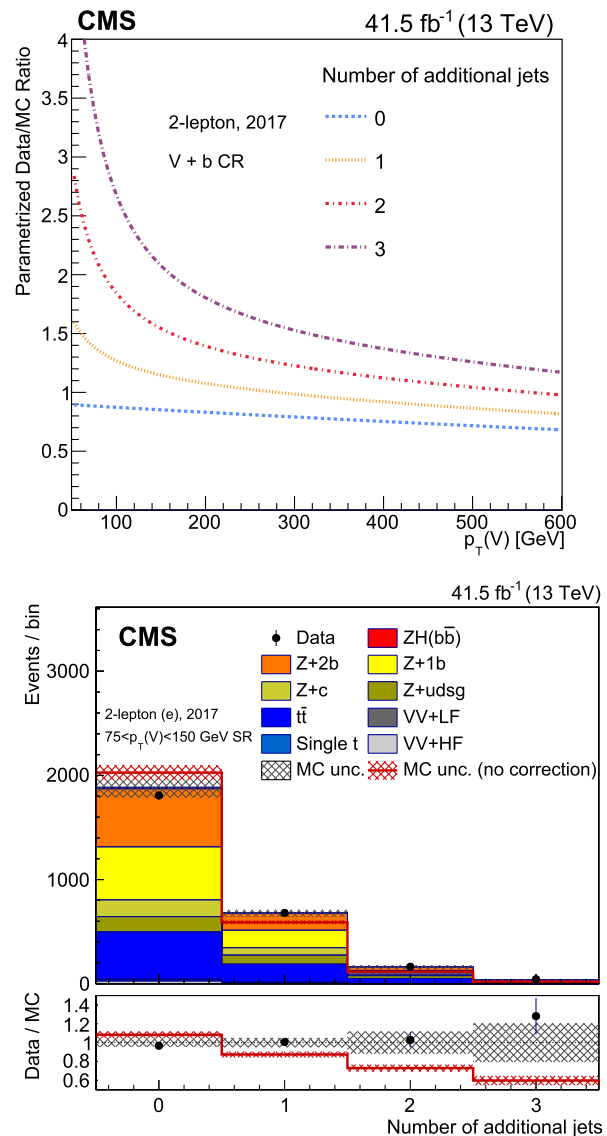


FIG. 4. The data-to-simulation ratio in the 2-lepton $Z + b$ CR is parametrized as a two-dimensional function of the number of additional jets and $p_T(V)$. The values of the parametrization are shown as a function of these variables in the upper panel. The distribution of the number of additional jets in the low- $p_T(V)$ STXS SR of the 2-lepton channel with (histogram) and without (red line) the application of the reweighting correction and associated systematic uncertainty is shown in the lower panel for the 2017 dataset, after the likelihood fit to data. In the ratio pad, the hatched bands associated with the corrected (gray) and noncorrected (red) number of additional jets indicate the systematic uncertainty in the sum of the signal and background templates.

is used as the shape uncertainty associated with the reweighting. The uncertainties are treated as uncorrelated between data-taking years and across background processes to account for differences in the level of mismodeling between processes and data-taking periods. Figure 4 (right panel) shows an example distribution, after the likelihood

fit to data, of the noncorrected and the corrected number of additional jets, for the 2017 dataset in the low- $p_T(V)$ STXS region SR (2-lepton channel).

The shape uncertainty associated with the number of additional jets reweighting correction, which is the full value of the weight, is included in the hatched gray band. Therefore, its size is significantly larger than the overall uncertainty associated with the noncorrected number of additional jets. The statistical uncertainty in the data yields is not included in the hatched bands and is present in the error bar associated with the data points in the ratio panel. The reweighting model, discussed in Sec. III, significantly improves the description of the data by the simulation in this observable. It also provides an additional uncertainty in this distribution.

Regarding the reweighting of the jet angular separation observable in the $\Delta R(jj) < 1$ region discussed in Sec. II, shape variations are derived by extracting the statistical uncertainties of the $\Delta R(jj)$ templates in data and simulation used for the reweighting procedure for each $V + \text{jets}$ process. These shape uncertainties are treated as uncorrelated across analysis channels, STXS categories and data-taking periods. Normalization uncertainties in the NLO EW and NNLO QCD corrections applied to the high- $p_T(V)$ region in the signal and $V + \text{jets}$ samples are estimated as 2 and 5% for the NLO EW and NNLO QCD corrections, respectively.

The uncertainty in the integrated luminosity measurement is 1.2, 2.3, and 2.5% in the 2016, 2017, and 2018 data-taking periods, respectively [31–33]. These uncertainties are treated as partially correlated between the three data-taking years. A 4.6% uncertainty in the total inelastic cross section [78], used to evaluate the PU profile in data for reweighting to the simulated PU profile, is applied.

The corrections applied to simulated samples to account for differences in the electron and muon trigger, reconstruction, and identification efficiencies with respect to data are affected by systematic uncertainties. These uncertainties originate from choices made in the efficiency measurement method, the selection applied to the leptons, and the limited size of the simulated samples used in the measurement. They depend on the lepton p_T and η , and affect the process normalizations by 1–2%. An uncertainty in the p_T^{miss} trigger efficiency correction is included in the model and has a $\approx 1\%$ effect.

Uncertainties in the b tagging efficiency and misidentification rate measurements used in the analysis of the resolved topology depend on the jet flavor, and the p_T and η of the jet. These uncertainties are split into 9 independent sources and 15 p_T and η bins, and treated as uncorrelated between the three data-taking periods. For the $b\bar{b}$ tagging efficiencies used in the analysis of the boosted topology, uncertainties are provided for the $H \rightarrow b\bar{b}$ signal output node of the DeepAK8 discriminant. They account for the limited size of the simulated samples available for the

calibration; the relative uncertainty in the fraction of boosted jet contributions present in the calibration; and for the normalizations of these contributions. The $b\bar{b}$ tagging uncertainties are uncorrelated between the efficiency working points and are parametrized in regions of jet p_T (200–300, 300–400, 400–500, 500–600, >600) GeV.

Uncertainties in the JES and JER depend on the p_T and η of the jets, and affect the kinematic properties of resolved and boosted jets, as well as the p_T^{miss} in the event. The uncertainties in the JES are split into independent sources [65] accounting for different experimental effects. Some of these uncertainty sources are correlated between the different data-taking periods, e.g., when that uncertainty component depends on the size of the available data sample. For b -tagged jets, to which the previously described b jet energy regression is applied, dedicated uncertainties in the JES and JER corrections are applied, as discussed in Sec. III.

Uncertainties affecting the shape of the $p_T(V)$ spectrum are taken into account. The discriminants used for the signal extraction in the resolved and boosted SRs are $p_T(V)$ -dependent and $p_T(V)$ represents an important source of discrimination between signal and background, as discussed in Secs. VB4 and VC. Additionally, the STXS categorization is based on $p_T(V)$, as described in Sec. VA. Because the shape of the $p_T(V)$ spectrum is used in the fit model, the parameters that scale the background process normalizations are parametrized continuously in $p_T(V)$ rather than in individual STXS bins. To account for differences between adjacent categories, uncertainties in the p_T shapes are defined for each $p_T(V)$ boundary. These $p_T(V)$ uncertainties are parametrized with linear variation shape uncertainties are anticorrelated, following the STXS categorization at the $p_T(V)$ boundaries of 150 GeV (2-lepton channel only) and 250 GeV (all channels) for all processes. These uncertainties are also considered as uncorrelated across lepton channels, background processes, and data-taking eras. They are implemented with large prior constraints in the fit model to mimic freely floating flat prior uncertainties and are significantly constrained by the fit to data.

In addition to the $p_T(V)$ -based uncertainties, freely floating parameters that scale the normalizations of the main background components, i.e., production of a vector boson associated with heavy (b , c) or light-quark jets and $t\bar{t}$, are included in the fit as described in Sec. VII. These parameters are constrained in the dedicated background-enriched regions discussed in Sec. V, i.e., $V + b$ jets, $V + \text{light-quark jets}$, and $t\bar{t}$. The parameters that scale the process normalizations are treated as uncorrelated between lepton flavors (e , μ).

To account for the finite sizes of the simulated samples, each bin of the simulated signal-plus-background template is allowed to vary within its statistical uncertainty, independently from the other bins in the distribution,

TABLE VI. Discriminating variables fitted in each SR and CR. The DeepAK8bbVsLight designation represents the DEEPAK8 discriminant for the light-quark flavor discrimination node.

	SR	$t\bar{t}$ CR	V + light-quark jets CR	V + b jets CR
0-lepton, resolved	DNN	$p_T(V)$	$p_T(V)$	HFDNN
0-lepton, boosted	BDT	DeepAK8bbVsLight	DeepAK8bbVsLight	DeepAK8bbVsLight
1-lepton, resolved	DNN	$p_T(V)$	$p_T(V)$	HFDNN
1-lepton, boosted	BDT	DeepAK8bbVsLight	DeepAK8bbVsLight	DeepAK8bbVsLight
2-lepton, resolved	DNN	$p_T(V)$	$p_T(V)$	DEEPCSV scores
2-lepton, boosted	BDT	DeepAK8bbVsLight	DeepAK8bbVsLight	DeepAK8bbVsLight

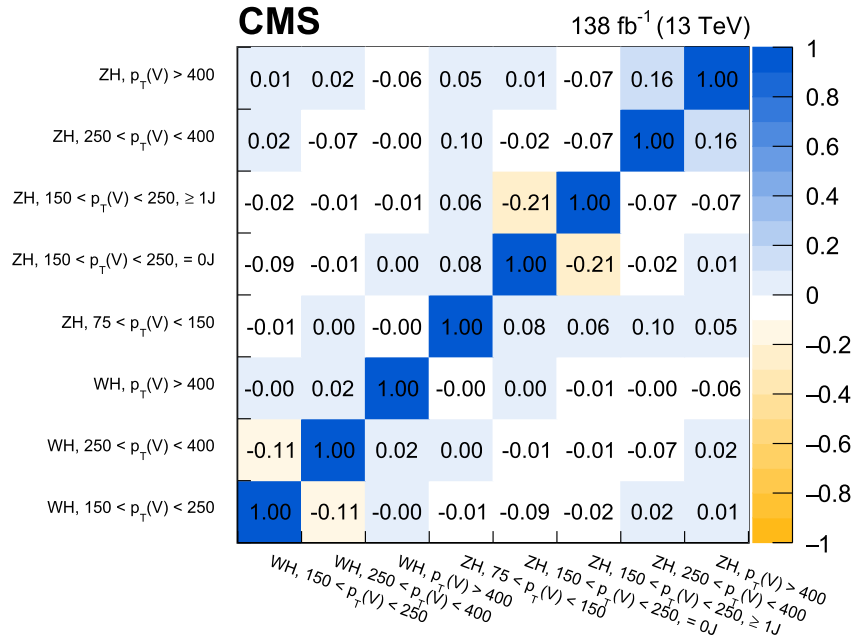


FIG. 5. Correlation matrix of the parameters of interest in the STXS measurement. The vector boson momenta have units of GeV.

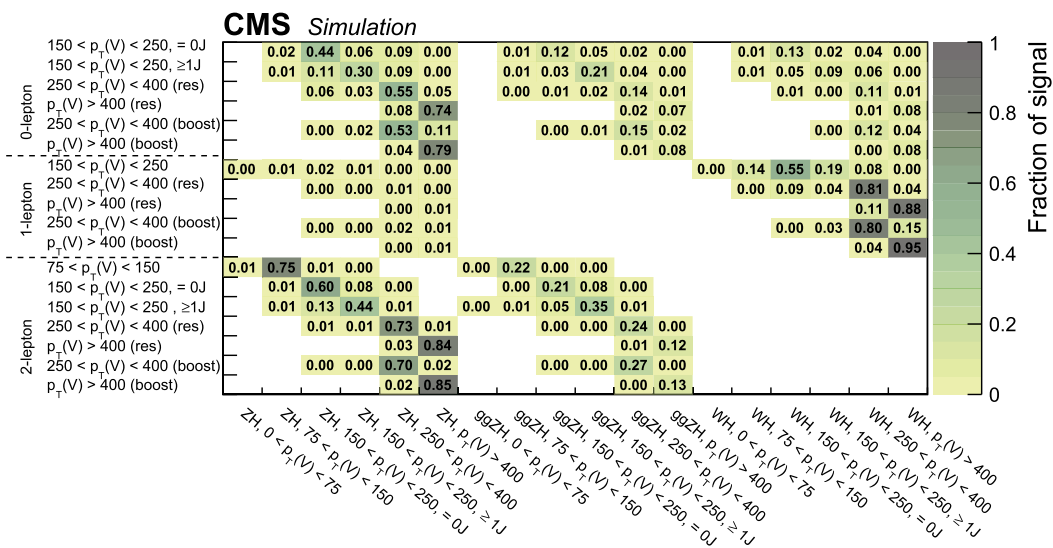


FIG. 6. Contributions of the different STXS signal bins as a fraction of the total signal yield in each SR. The vector boson momenta have units of GeV.

following the Barlow–Beeston “light” approach [79]. The impact of the systematic uncertainties in the measured cross sections in the different STXS bins is discussed in Sec. VII.

VII. ANALYSIS RESULTS

The analysis targets the measurement of the Higgs boson signal strength using VH production with a subsequent $H \rightarrow b\bar{b}$ decay and interprets the results in terms of the STXS categorization for the $V(\text{leptonic})H$ process, as discussed in Sec. VA. Results are extracted from a simultaneous maximum likelihood fit of the signal-plus-background model to the data distributions in all SRs and CRs, based on the templates detailed in Table VI.

In the resolved and boosted SRs, the DNN and BDT classifiers presented in Sec. V are employed. The variable used in the resolved CRs depends on the channel. In the 0- and 1-lepton channels, the multiclassifier DNN described in Sec. VB is employed in the $V + b$ jets CR, while $p_T(V)$ is used in the $t\bar{t}$ and $V + \text{light-quark jets}$ CRs. In the 2-lepton channel, the fitted variable in the $V + b$ jets CR is the score of the DEEPCSV discriminant, binned to align with the established working points, while the remaining CRs use $p_T(V)$ as in the 0- and 1-lepton channels. In the boosted CRs, the DEEPAK8 discriminant for the light-quark jet discrimination node (DeepAK8bbVsLight) is used in conjunction with the selection requirement described in Sec. VC. For the $V + b$ jets and $t\bar{t}$ CRs, the DEEPAK8 discriminant is tagged as in the SR, while for the $V + \text{light-quark jets}$ CR, the DEEPAK8 discriminant is required to be < 0.8 .

The analysis regions are partitioned into categories targeting specific STXS bins in order to maximize the sensitivity to the different STXS bin signals, as discussed in Sec. V. The shapes and normalizations of all distributions for the signal and background components are allowed to vary within the systematic uncertainties described in Sec. VI. These uncertainties are treated as independent nuisance parameters in the fit to the data. For the nuisance parameters with shape-altering effects, alternative templates that correspond to a variation of ± 1 standard deviation of the associated nuisance parameter are used.

To reduce the effects from statistical fluctuations on these alternative templates in the SRs, a smoothing technique is applied to templates exhibiting the largest fluctuations with respect to the nominal templates. The normalization of the systematic variation is fixed, and the ratio of the template with respect to the nominal is smoothed. The uncertainty sources that show the largest fraction of bin-to-bin fluctuations are the JES, JER, and PU uncertainties. For those uncertainties, the smoothing procedure is applied to all processes in the analysis SRs. Freely floating parameters, termed process scale factors, accounting for the difference in normalization between simulation and data for the main background processes, namely $t\bar{t}$, $V + \text{udsg}$, $V + c$, $V + b$,

and $V + b\bar{b}$, are constrained in the CRs and SRs. These process scale factors are correlated across lepton channels. In the 0- and 2-lepton channels, the $V + b$ and $V + b\bar{b}$ components are split by employing freely floating parameters. In the 1-lepton channel, a freely floating parameter for the $V + b\bar{b}$ process is used in addition to a prior constraint that governs the ratio of $V + b$ to $V + b\bar{b}$. This implementation is employed because the number of $V + b$ events in the

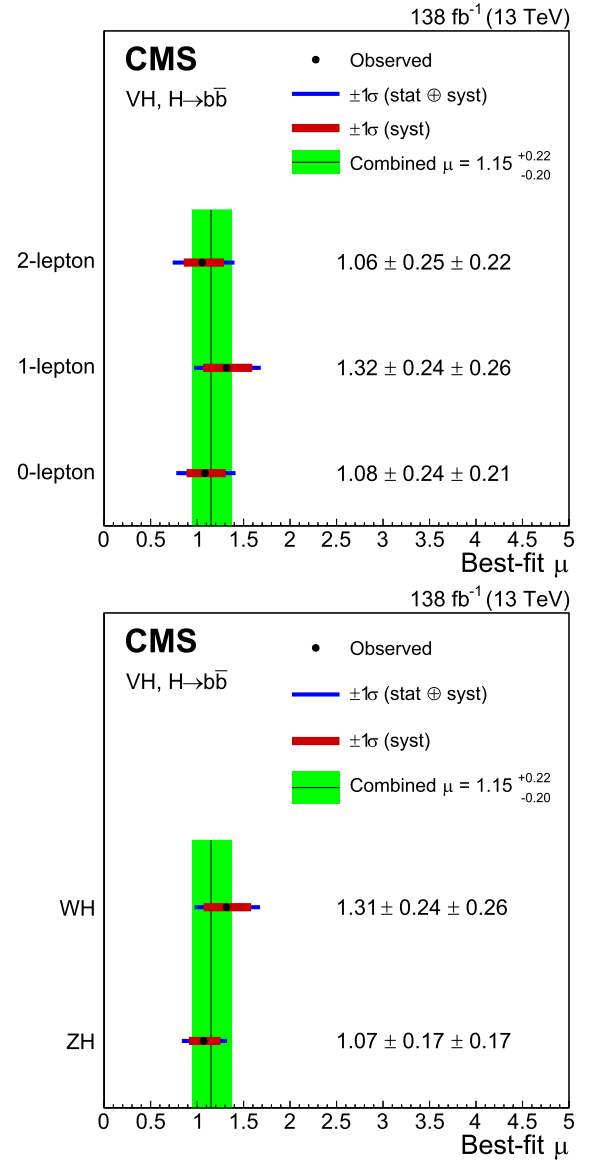


FIG. 7. Signal strengths (points) for the 0-, 1-, and 2-lepton channels (upper) and the ZH and WH production modes (lower). The horizontal red and blue bars on the points represent the systematic and total uncertainties, respectively. The combined inclusive signal strength is shown by the vertical line, with the green band giving the 68% confidence interval. The results combine the 2016–2018 data-taking years. The first and the second uncertainty values correspond to the statistical and systematic uncertainties, respectively.

1-lepton, channel is limited due to the tight b tagging requirement applied in the selection.

To allow for shape uncertainties of the $p_T(V)$ spectrum predictions in the categories targeting different STXS bins, linear variations as a function of the reconstructed $p_T(V)$ are created, as discussed in Sec. VI. Process scale factors correcting for the normalization difference between

simulation and data for the main background processes are employed, together with this $p_T(V)$ -based uncertainty, to correct the shape of the $p_T(V)$ spectrum in simulation to match data.

Additional unconstrained parameters, used to measure flavor tagging scale factors *in situ* in the boosted analysis regions, are employed to account for the (mis)tagging

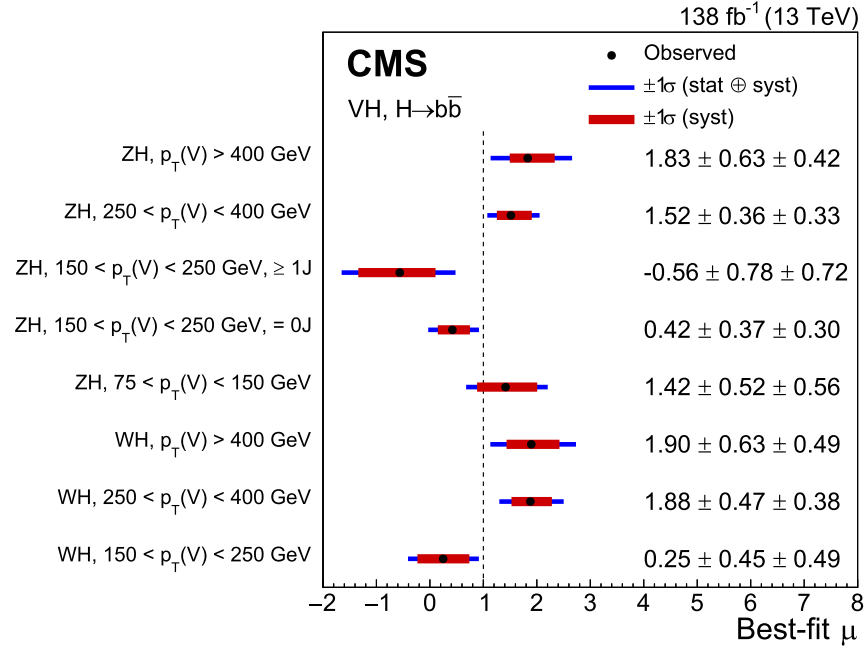


FIG. 8. STXS signal strengths from the analysis of the 2016–2018 data. The vertical dashed line corresponds to the SM value of the signal strength. The first and the second uncertainty values correspond to the statistical and systematic uncertainties, respectively.

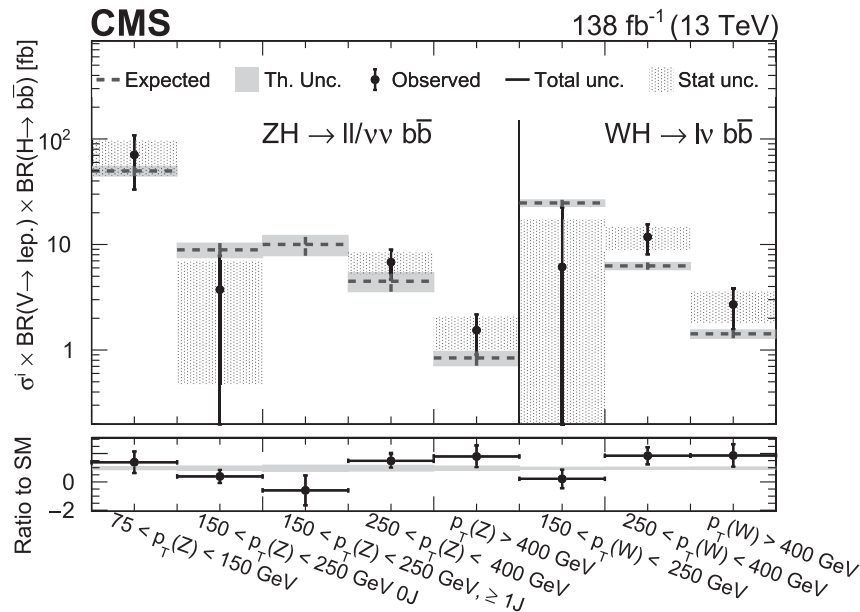


FIG. 9. Measured values of $\sigma\mathcal{B}$, defined as the product of the VH production cross sections multiplied by the branching fractions of $V \rightarrow$ leptons and $H \rightarrow b\bar{b}$, evaluated in the same STXS bins as for the signal strengths, combining all years. In the lower panel, the ratio of the observed results, with associated uncertainties, to the SM expectations is shown. If the observed signal strength for a given STXS bin is negative, no value is plotted for $\sigma\mathcal{B}$ in the upper panel.

TABLE VII. Predicted and measured values of the product of the cross section and branching fractions in the V (leptonic)H STXS process scheme. The SM predictions for each bin are calculated using the inclusive values reported in Ref. [28]. The uncertainties shown are the combined statistical and systematic components.

STXS bin	Expected $\sigma\mathcal{B}$ [fb]	Observed $\sigma\mathcal{B}$ [fb]	Best-fit μ
ZH $75 < p_T(Z) < 150$ GeV	50.0 ± 5.3	71 ± 38	1.4 ± 0.8
ZH $150 < p_T(Z) < 250$ GeV 0 jets	9.0 ± 1.4	3.8 ± 4.1	0.4 ± 0.5
ZH $150 < p_T(Z) < 250$ GeV ≥ 1 jets	10.1 ± 2.2	< 0	-0.6 ± 1.0
ZH $250 < p_T(Z) < 400$ GeV	4.5 ± 0.9	6.9 ± 2.2	1.5 ± 0.5
ZH $p_T(Z) > 400$ GeV	0.9 ± 0.1	1.6 ± 0.6	1.8 ± 0.8
WH $150 < p_T(W) < 250$ GeV	24.9 ± 1.8	6 ± 16	0.2 ± 0.7
WH $250 < p_T(W) < 400$ GeV	6.3 ± 0.5	11.9 ± 3.8	1.9 ± 0.6
WH $p_T(W) > 400$ GeV	1.4 ± 0.1	2.7 ± 1.1	1.9 ± 0.8

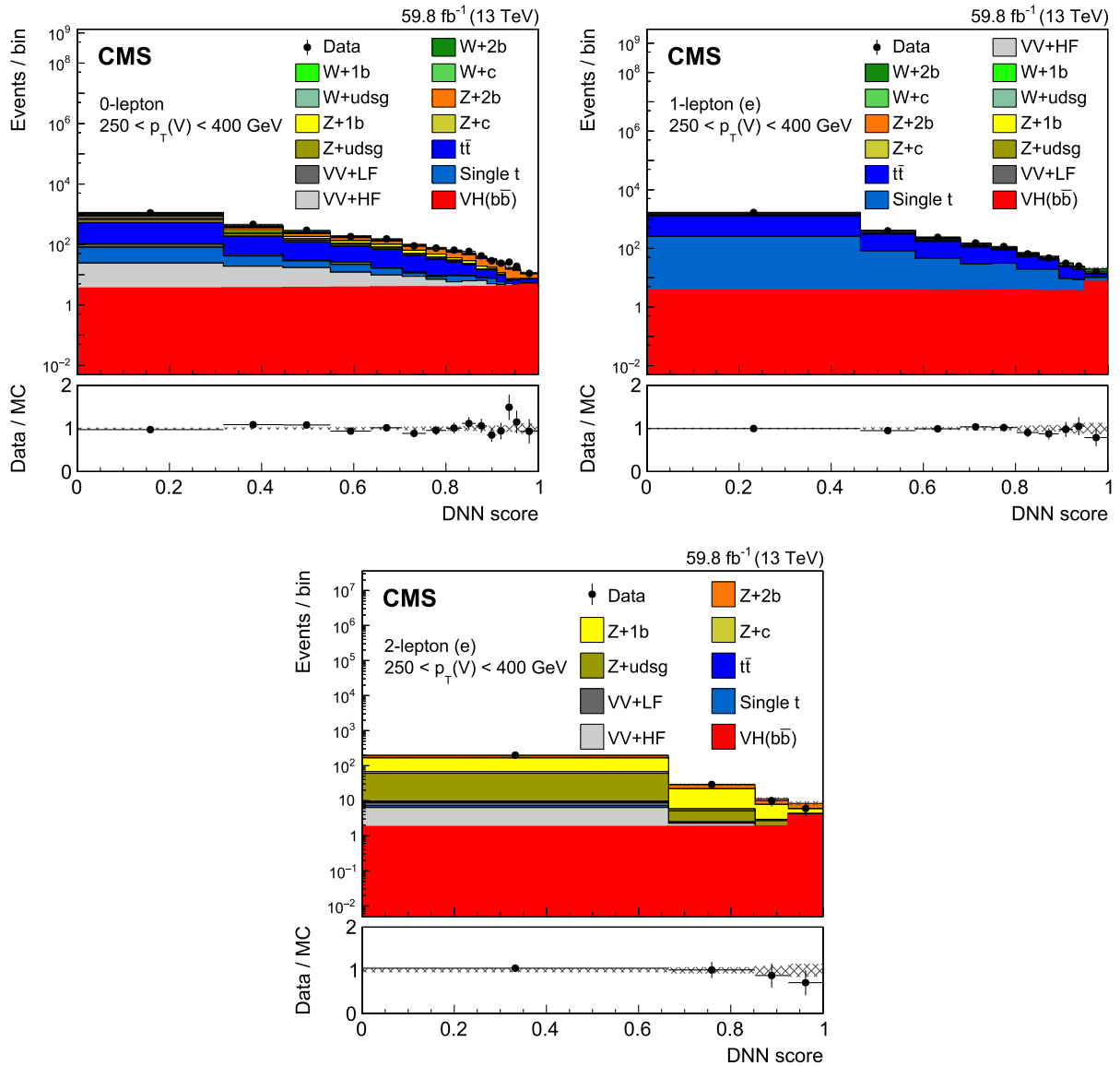


FIG. 10. Post-fit distributions of the DNN discriminant in the $250 < p_T(V) < 400$ GeV category of the 0-lepton (top left), 1-lepton (top right) and 2-lepton (bottom) channels for the electron final state using the 2018 dataset. The background contributions after the maximum likelihood fit are shown as filled histograms. The Higgs boson signal is also shown as a filled histogram, and is normalized to the signal strength shown in Fig. 8. The hatched band indicates the combined statistical and systematic uncertainty in the sum of the signal and background templates. The ratio of the data to the sum of the fitted signal and background is shown in the lower panel. The distributions that enter the maximum likelihood fit use the same binning as shown here.

efficiency difference between data and simulation for high-momentum light-quark, c , and b jets. The procedure is described in more detail in Sec. V C. These parameters are treated as fully correlated between channels, and are not correlated with the background process scale factors. As discussed in Sec. VI, the process scale factors and *in situ* flavor tagging scale factors are fully uncorrelated between lepton flavors.

Figure 5 shows the correlation matrix of the signal strengths split by STXS bin for the analysis of all data-taking years combined. As expected (see Sec. V A), the signal strengths for the medium $p_T(V)$ STXS bins with 0 and at least 1 jet exhibit the largest correlation (-21%). The fractional contribution of each STXS bin to the total signal in each category is shown in Fig. 6. The signal purity is higher in the 2-lepton channel than in the 0- and 1-lepton channels.

The inclusive signal strength extracted from a simultaneous maximum likelihood fit of the SRs and CRs, combining all three data-taking years, is $\mu = 1.15^{+0.22}_{-0.20}$, where the uncertainties include both the statistical and systematic components. The individual signal strengths are $\mu = 1.43 \pm 0.37$, $\mu = 0.68 \pm 0.36$, and $\mu = 1.23 \pm 0.30$ for the 2016, 2017, and 2018 data-taking years, respectively. Figure 7 shows the signal strengths per analysis channel, as well as the signal strengths split by production mode (ZH or WH). The p -value compatibility of the individual deviations of the three analysis channels from the SM expectation ($\mu = 1$) is 64%, while the p -value compatibility of the three analysis channels with the inclusive $VH, H \rightarrow b\bar{b}$ signal strength is 84%.

The measured signal strengths in the different STXS bins, fitting all data-taking years (2016–2018) are shown in Fig. 8. These results are interpreted in Fig. 9 as $\sigma\mathcal{B}$, the product of the production cross sections and the branching fractions for $V \rightarrow$ leptons and $H \rightarrow b\bar{b}$. To convert the results to measurements of the production cross section alone, theoretical uncertainties that modify the overall cross section of the individual STXS bins, or the inclusive cross section, are removed from the fit. These measured cross sections, along with the SM predictions, are given in Table VII. The local inclusive observed (expected) significance of the measured ZH and WH signals, over the background-only expectation, is found to be 6.3 (5.6) standard deviations when taking into account all three data-taking years. Examples of post-fit distributions of the DNN output scores in the SRs of the 2018 dataset are shown in Fig. 10 for the 0-, 1-, and 2-lepton channels in the category targeting the $250 < p_T(V) < 400$ GeV STXS bin. Figure 11 shows the distribution of events in all channels, sorted according to the observed value of $\log_{10}(S/B)$, for the three data-taking years combined; here, the signal (S) and background (B) yields are determined from the discriminant scores used in the resolved and boosted analyses.

Table VIII shows the contribution, in terms of absolute uncertainties, to the uncertainty in the measured inclusive

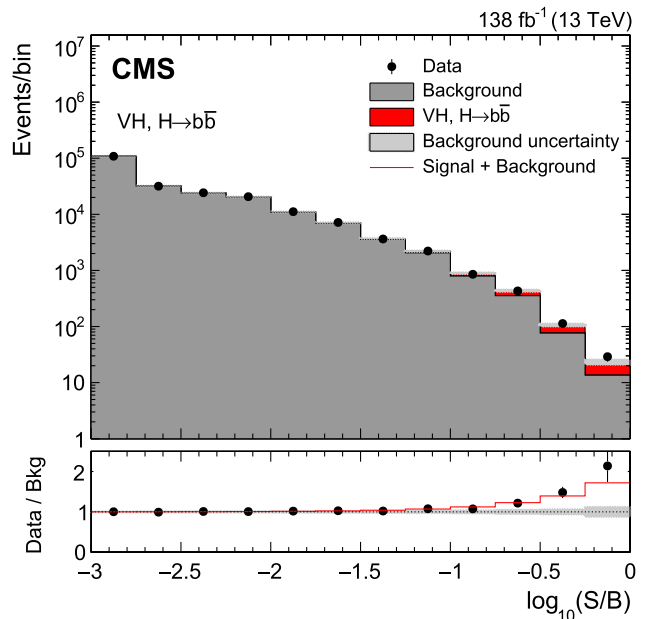


FIG. 11. Distributions of signal, background, and observed data event yields sorted into bins of similar signal-to-background ratio, as given by the result of the fit to the multivariate discriminants in the resolved and boosted categories. All events in the signal regions of the 2016–2018 dataset are included. The red histogram indicates the Higgs boson signal assuming SM yields ($\mu = 1$) and the sum of all backgrounds is given by the gray histogram. The lower panel shows the ratio of the observed data to the background expectation, with the total uncertainty in the background prediction indicated by the gray hatching. The red line indicates the sum of signal assuming the SM prediction plus background contribution, divided by the background.

signal strength originating from the various sources of systematic uncertainty. This contribution for a given group of uncertainties is defined as the difference in quadrature between the total uncertainty in the signal strength and the uncertainty in the signal strength with the nuisance parameters of the corresponding group fixed to their best-fit values. The total statistical uncertainty is defined as the uncertainty

TABLE VIII. The sources of systematic uncertainty in the inclusive signal strength measurement and their positive and negative values.

	$\Delta\mu$
Background (theory)	+0.043 – 0.043
Signal (theory)	+0.088 – 0.059
MC sample size	+0.078 – 0.078
Simulation modeling	+0.059 – 0.059
b tagging	+0.050 – 0.046
Jet energy resolution	+0.036 – 0.028
Int. luminosity	+0.032 – 0.027
Jet energy scale	+0.025 – 0.025
Lepton ident.	+0.008 – 0.007
Trigger (\bar{p}_T^{miss})	+0.002 – 0.001

in the signal strength when all the constrained nuisance parameters are fixed to their best-fit values, while the total systematic uncertainty is defined as the difference in quadrature between the total uncertainty in the signal strength and the total statistical uncertainty. Table VIII breaks the total uncertainty down into the following sources.

- (i) Theoretical uncertainties in the signal and background components.
- (ii) Limited size of simulated samples.
- (iii) Simulation modeling, including uncertainty sources associated with the modeling of the $V + \text{jets}$ background components, as discussed in Sec. II. Additionally, the $p_T(V)$ migration uncertainties are included in this category.
- (iv) Experimental uncertainties (b tagging, integrated luminosity, JES and JER, lepton identification, and trigger). The JES and JER components include the dedicated uncertainty in mass scale and smearing that is applied for jets subject to the b jet energy regression.

The limited size of the NLO $V + \text{jets}$ samples is the largest contribution to the overall VH , $H \rightarrow b\bar{b}$ signal strength uncertainty.

A. Cross-check analysis: Extraction of VZ with $Z \rightarrow b\bar{b}$

The VZ process, where the Z boson decays into a $b\bar{b}$ pair, has an identical final state to the VH process with $H \rightarrow b\bar{b}$. Therefore, it is used to cross-check the methodology for the VH , $H \rightarrow b\bar{b}$ analysis. The DNN and BDT discriminants in the resolved and boosted SRs are trained using the simulated diboson sample as signal. All other processes are considered as background. The VZ , $Z \rightarrow b\bar{b}$ analysis makes use of the same event categorization as the VH analysis discussed in Sec. V, with the only modification being the requirement that $M(\text{jj})$ lies in the range 60–120 GeV to define the SR for all channels. The inclusive observed VZ , $Z \rightarrow b\bar{b}$ signal strength is $\mu = 1.25 \pm 0.14$, corresponding to observed and expected significances well above 5 standard deviations. The per-production process signal strengths, μ_{ZZ} and μ_{WZ} , are $1.19 \pm 0.09(\text{stat}) \pm 0.11(\text{syst})$ and $1.61 \pm 0.18(\text{stat}) \pm 0.24(\text{syst})$, respectively.

VIII. SUMMARY

Measurements are presented of the cross section for the associated production of the 125 GeV Higgs boson and a W or Z boson, where the Higgs boson decays to $b\bar{b}$ and the vector bosons decay to leptons. Proton-proton collision data collected by the CMS experiment during 2016–2018 at $\sqrt{s} = 13$ TeV are used, corresponding to an integrated luminosity of 138 fb^{-1} . Five decay channels are analyzed, and both resolved as well as merged-jet topology are employed in each vector boson decay mode. An additional subcategorization in the transverse momentum of the vector boson and the number of additional jets in the

event is applied to maximize the sensitivity of different simplified template cross section bins. The overall signal strength, combining all analysis categories, is found to be $\mu = 1.15^{+0.22}_{-0.20}$. The production of the Higgs boson in association with a vector boson and decays to bottom quark pairs is established with an observed (expected) significance of 6.3 (5.6) standard deviations.

ACKNOWLEDGMENTS

We congratulate our colleagues in the CERN accelerator departments for the excellent performance of the LHC and thank the technical and administrative staffs at CERN and at other CMS institutes for their contributions to the success of the CMS effort. In addition, we gratefully acknowledge the computing centers and personnel of the Worldwide LHC Computing Grid and other centers for delivering so effectively the computing infrastructure essential to our analyses. Finally, we acknowledge the enduring support for the construction and operation of the LHC, the CMS detector, and the supporting computing infrastructure provided by the following funding agencies: SC (Armenia), BMBWF and FWF (Austria); FNRS and FWO (Belgium); CNPq, CAPES, FAPERJ, FAPERGS, and FAPESP (Brazil); MES and BNSF (Bulgaria); CERN; CAS, MoST, and NSFC (China); Minciencias (Colombia); MSES and Croatian Science Foundation (CSF, Croatia); Research and Innovation Foundation (RIF, Cyprus); SENESCYT (Ecuador); Ministry of Education and Research (MoER), ERC PUT and ERDF (Estonia); Academy of Finland, Finnish Ministry of Education and Culture (MEC), and Helsinki Institute of Physics (HIP, Finland); CEA and CNRS/IN2P3 (France); SRNSF (Georgia); BMBF, DFG, and HGF (Germany); GSRI (Greece); NKFIH (Hungary); DAE and DST (India); IPM (Iran); SFI (Ireland); INFN (Italy); MSIP and NRF (Republic of Korea); MES (Latvia); Lithuanian Academy of Sciences (LAS, Lithuania); MOE and UM (Malaysia); BUAP, CINVESTAV, CONACYT, LNS, SEP, and UASLP-FAI (Mexico); MOS (Montenegro); MBIE (New Zealand); PAEC (Pakistan); MES and NSC (Poland); FCT (Portugal); MESTD (Serbia); MCIN/AEI and PCTI (Spain); MOSTR (Sri Lanka); Swiss Funding Agencies (Switzerland); MST (Taipei); MHESI and NSTDA (Thailand); TUBITAK and TENMAK (Turkey); NASU (Ukraine); STFC (United Kingdom); DOE and NSF (USA). Individuals have received support from the Marie-Curie program and the European Research Council and Horizon 2020 Grant, contracts No. 675440, No. 724704, No. 752730, No. 758316, No. 765710, No. 824093, and COST Action No. CA16108 (European Union); the Leventis Foundation; the Alfred P. Sloan Foundation; the Alexander von Humboldt Foundation; the Science Committee, project no. 22rl-037 (Armenia); the Belgian Federal Science Policy Office; the Fonds pour la Formation à la Recherche dans l'Industrie et dans l'Agriculture

(FRIA-Belgium); the Agentschap voor Innovatie door Wetenschap en Technologie (IWT-Belgium); the F.R.S.-FNRS and FWO (Belgium) under the “Excellence of Science—EOS”—be.h project n. 30820817; the Beijing Municipal Science & Technology Commission, No. Z191100007219010 and Fundamental Research Funds for the Central Universities (China); the Ministry of Education, Youth and Sports (MEYS) of the Czech Republic; the Shota Rustaveli National Science Foundation, Grant No. FR-22-985 (Georgia); the Deutsche Forschungsgemeinschaft (DFG), under Germany’s Excellence Strategy—EXC 2121 “Quantum Universe”—390833306, and under project no. 400140256—GRK2497; the Hellenic Foundation for Research and Innovation (HFRI), Project Number 2288 (Greece); the Hungarian Academy of Sciences, the New National Excellence Program—ÚNKP, the NKFIH research Grants No. K 124845, No. K 124850, No. K 128713, No. K 128786, No. K 129058, No. K 131991, No. K 133046, No. K 138136, No. K 143460, No. K 143477, No. 2020-2.2.1-ED-2021-00181, and No. TKP2021-NKTA-64 (Hungary); the Council of Science and Industrial Research, India; ICSC—National

Research Center for High Performance Computing, Big Data and Quantum Computing, funded by the NextGeneration EU program (Italy); the Latvian Council of Science; the Ministry of Education and Science, project no. 2022/WK/14, and the National Science Center, contracts Opus No. 2021/41/B/ST2/01369 and No. 2021/43/B/ST2/01552 (Poland); the Fundação para a Ciência e a Tecnologia, Grant No. CEECIND/01334/2018 (Portugal); the National Priorities Research Program by Qatar National Research Fund; MCIN/AEI/10.13039/501100011033, ERDF “a way of making Europe”, and the Programa Estatal de Fomento de la Investigación Científica y Técnica de Excelencia María de Maeztu, grant No. MDM-2017-0765 and Programa Severo Ochoa del Principado de Asturias (Spain); the Chulalongkorn Academic into Its 2nd Century Project Advancement Project, and the National Science, Research and Innovation Fund via the Program Management Unit for Human Resources & Institutional Development, Research and Innovation, Grant No. B37G660013 (Thailand); the Kavli Foundation; the Nvidia Corporation; the SuperMicro Corporation; the Welch Foundation, contract No. C-1845; and the Weston Havens Foundation (USA).

-
- [1] ATLAS Collaboration, Observation of a new particle in the search for the Standard Model Higgs boson with the ATLAS detector at the LHC, *Phys. Lett. B* **716**, 1 (2012).
- [2] CMS Collaboration, Observation of a new boson at a mass of 125 GeV with the CMS experiment at the LHC, *Phys. Lett. B* **716**, 30 (2012).
- [3] CMS Collaboration, Observation of a new boson with mass near 125 GeV in pp collisions at $\sqrt{s} = 7$ and 8 TeV, *J. High Energy Phys.* **06** (2013) 081.
- [4] F. Englert and R. Brout, Broken symmetry and the mass of gauge vector mesons, *Phys. Rev. Lett.* **13**, 321 (1964).
- [5] P. W. Higgs, Broken symmetries, massless particles and gauge fields, *Phys. Lett.* **12**, 132 (1964).
- [6] P. W. Higgs, Broken symmetries and the masses of gauge bosons, *Phys. Rev. Lett.* **13**, 508 (1964).
- [7] G. S. Guralnik, C. R. Hagen, and T. W. B. Kibble, Global conservation laws and massless particles, *Phys. Rev. Lett.* **13**, 585 (1964).
- [8] P. W. Higgs, Spontaneous symmetry breakdown without massless bosons, *Phys. Rev.* **145**, 1156 (1966).
- [9] T. W. B. Kibble, Symmetry breaking in non-Abelian gauge theories, *Phys. Rev.* **155**, 1554 (1967).
- [10] ATLAS Collaboration, Measurement of Higgs boson production in the diphoton decay channel in pp collisions at center-of-mass energies of 7 and 8 TeV with the ATLAS detector, *Phys. Rev. D* **90**, 112015 (2014).
- [11] CMS Collaboration, Observation of the diphoton decay of the Higgs boson and measurement of its properties, *Eur. Phys. J. C* **74**, 3076 (2014).
- [12] ATLAS Collaboration, Measurements of Higgs boson production and couplings in the four-lepton channel in pp collisions at center-of-mass energies of 7 and 8 TeV with the ATLAS detector, *Phys. Rev. D* **91**, 012006 (2015).
- [13] CMS Collaboration, Measurement of the properties of a Higgs boson in the four-lepton final state, *Phys. Rev. D* **89**, 092007 (2014).
- [14] ATLAS Collaboration, Observation and measurement of Higgs boson decays to WW^* with the ATLAS detector, *Phys. Rev. D* **92**, 012006 (2015).
- [15] ATLAS Collaboration, Study of $(W/Z)H$ production and Higgs boson couplings using $H \rightarrow WW^*$ decays with the ATLAS detector, *J. High Energy Phys.* **08** (2015) 137.
- [16] CMS Collaboration, Measurement of Higgs boson production and properties in the WW decay channel with leptonic final states, *J. High Energy Phys.* **01** (2014) 096.
- [17] ATLAS Collaboration, Evidence for the Higgs boson Yukawa coupling to tau leptons with the ATLAS detector, *J. High Energy Phys.* **04** (2015) 117.
- [18] CMS Collaboration, Evidence for the 125 GeV Higgs boson decaying to a pair of τ leptons, *J. High Energy Phys.* **05** (2014) 104.
- [19] CMS Collaboration, Observation of Higgs boson decays to a pair of tau leptons, *Phys. Lett. B* **779**, 283 (2017).
- [20] CMS Collaboration, Measurements of properties of the Higgs boson decaying to a W boson pair in pp collisions at $\sqrt{s} = 13$ TeV, *Phys. Lett. B* **791**, 96 (2019).

- [21] ATLAS Collaboration, Observation of $H \rightarrow b\bar{b}$ decays and VH production with the ATLAS detector, *Phys. Lett. B* **786**, 59 (2018).
- [22] CMS Collaboration, Observation of $t\bar{t}H$ production, *Phys. Rev. Lett.* **120**, 231801 (2018).
- [23] ATLAS Collaboration, Observation of Higgs boson production in association with a top quark pair at the LHC with the ATLAS detector, *Phys. Lett. B* **784**, 173 (2018).
- [24] ATLAS Collaboration, A detailed map of Higgs boson interactions by the ATLAS experiment ten years after the discovery, *Nature (London)* **607**, 52 (2022).
- [25] CMS Collaboration, A portrait of the Higgs boson by the CMS experiment ten years after the discovery, *Nature (London)* **607**, 60 (2022).
- [26] CMS Collaboration, Evidence for Higgs boson decay to a pair of muons, *J. High Energy Phys.* **01** (2021) 148.
- [27] CMS Collaboration, Observation of Higgs boson decay to bottom quarks, *Phys. Rev. Lett.* **121**, 121801 (2018).
- [28] LHC Higgs Cross Section Working Group, Handbook of LHC Higgs Cross Sections: 4. Deciphering the Nature of the Higgs sector (CERN, Geneva, 2017), [10.23731/CYRM-2017-002](https://arxiv.org/abs/10.23731/CYRM-2017-002).
- [29] J. R. Andersen *et al.*, Les Houches 2015: Physics at TeV colliders standard model working group report, in *Proceedings of the 9th Les Houches Workshop on Physics at TeV Colliders (PhysTeV 2015) Les Houches, France, 2015* (2016), [arXiv:1605.04692](https://arxiv.org/abs/1605.04692).
- [30] ATLAS Collaboration, Measurements of WH and ZH production in the $H \rightarrow b\bar{b}$ decay channel in pp collisions at 13 TeV with the ATLAS detector, *Eur. Phys. J. C* **81**, 178 (2021).
- [31] CMS Collaboration, Precision luminosity measurement in proton-proton collisions at $\sqrt{s} = 13$ TeV in 2015 and 2016 at CMS, *Eur. Phys. J. C* **81**, 800 (2021).
- [32] CMS Collaboration, CMS luminosity measurement for the 2017 data-taking period at $\sqrt{s} = 13$ TeV, CMS physics analysis summary, Report No. CMS-PAS-LUM-17-004, 2018, <https://cds.cern.ch/record/2621960>.
- [33] CMS Collaboration, CMS luminosity measurement for the 2018 data-taking period at $\sqrt{s} = 13$ TeV, CMS Physics Analysis Summary, Report No. CMS-PAS-LUM-18-002, 2019, <https://cds.cern.ch/record/2676164>.
- [34] CMS Collaboration, Search for the standard model Higgs boson produced in association with a W or a Z boson and decaying to bottom quarks, *Phys. Rev. D* **89**, 012003 (2014).
- [35] CMS Collaboration, Evidence for the Higgs boson decay to a bottom quark-antiquark pair, *Phys. Lett. B* **780**, 501 (2018).
- [36] ATLAS Collaboration, Measurement of the associated production of a Higgs boson decaying into b -quarks with a vector boson at high transverse momentum in pp collisions at $\sqrt{s} = 13$ TeV with the ATLAS detector, *Phys. Lett. B* **816**, 136204 (2021).
- [37] HEPData record for this analysis (2023), [10.17182/hepdata.145636](https://hepdata.cern.ch/record/10.17182/hepdata.145636).
- [38] CMS Collaboration, The CMS trigger system, *J. Instrum.* **12**, P01020 (2017).
- [39] CMS Collaboration, The CMS experiment at the CERN LHC, *J. Instrum.* **3**, S08004 (2008).
- [40] P. Nason, A new method for combining NLO QCD with shower Monte Carlo algorithms, *J. High Energy Phys.* **11** (2004) 040.
- [41] S. Frixione, P. Nason, and C. Oleari, Matching NLO QCD computations with parton shower simulations: The POWHEG method, *J. High Energy Phys.* **11** (2007) 070.
- [42] S. Alioli, P. Nason, C. Oleari, and E. Re, A general framework for implementing NLO calculations in shower Monte Carlo programs: The POWHEG BOX, *J. High Energy Phys.* **06** (2010) 043.
- [43] K. Hamilton, P. Nason, and G. Zanderighi, MINLO: Multi-scale improved NLO, *J. High Energy Phys.* **10** (2012) 155.
- [44] G. Luisoni, P. Nason, C. Oleari, and F. Tramontano, $HW/HZ + 0$ and 1 jet at NLO with the POWHEG BOX interfaced to GoSam and their merging within MiNLO, *J. High Energy Phys.* **10** (2013) 083.
- [45] J. Alwall, R. Frederix, S. Frixione, V. Hirschi, F. Maltoni, O. Mattelaer, H. S. Shao, T. Stelzer, P. Torrielli, and M. Zaro, The automated computation of tree-level and next-to-leading order differential cross sections, and their matching to parton shower simulations, *J. High Energy Phys.* **07** (2014) 079.
- [46] R. Frederix and S. Frixione, Merging meets matching in MC@NLO, *J. High Energy Phys.* **12** (2012) 061.
- [47] J. Alwall *et al.*, Comparative study of various algorithms for the merging of parton showers and matrix elements in hadronic collisions, *Eur. Phys. J. C* **53**, 473 (2008).
- [48] S. Kallweit, J. M. Lindert, P. Maierhofer, S. Pozzorini, and M. Schonherr, NLO QCD + EW predictions for $V +$ jets including off-shell vector-boson decays and multijet merging, *J. High Energy Phys.* **04** (2016) 021.
- [49] G. Ferrera, M. Grazzini, and F. Tramontano, Higher-order QCD effects for associated WH production and decay at the LHC, *J. High Energy Phys.* **04** (2014) 039.
- [50] G. Ferrera, M. Grazzini, and F. Tramontano, Associated ZH production at hadron colliders: The fully differential NNLO QCD calculation, *Phys. Lett. B* **740**, 51 (2015).
- [51] O. Brein, R. V. Harlander, and T. J. E. Zirke, $vh@nnlo$ —Higgs Strahlung at hadron colliders, *Comput. Phys. Commun.* **184**, 998 (2013).
- [52] R. V. Harlander, S. Liebler, and T. Zirke, Higgs Strahlung at the Large Hadron Collider in the 2-Higgs-Doublet Model, *J. High Energy Phys.* **02** (2013) 023.
- [53] A. Denner, S. Dittmaier, S. Kallweit, and A. Mück, HAWK 2.0: A Monte Carlo program for Higgs production in vector-boson fusion and Higgs Strahlung at hadron colliders, *Comput. Phys. Commun.* **195**, 161 (2015).
- [54] M. Czakon and A. Mitov, Top++: A program for the calculation of the top-pair cross-section at hadron colliders, *Comput. Phys. Commun.* **185**, 2930 (2014).
- [55] R. D. Ball *et al.* (NNPDF Collaboration), Parton distributions for the LHC run II, *J. High Energy Phys.* **04** (2015) 040.
- [56] T. Sjöstrand, S. Mrenna, and P. Z. Skands, An introduction to PYTHIA 8.2, *Comput. Phys. Commun.* **191**, 159 (2015).
- [57] CMS Collaboration, Event generator tunes obtained from underlying event and multiparton scattering measurements, *Eur. Phys. J. C* **76**, 155 (2016).
- [58] P. Skands, S. Carrazza, and J. Rojo, Tuning PYTHIA 8.1: The Monash 2013 tune, *Eur. Phys. J. C* **74**, 3024 (2014).
- [59] S. Agostinelli *et al.* (GEANT4 Collaboration), GEANT4—a simulation toolkit, *Nucl. Instrum. Methods Phys. Res., Sect. A* **506**, 250 (2003).

- [60] CMS Collaboration, Particle-flow reconstruction and global event description with the CMS detector, *J. Instrum.* **12**, P10003 (2017).
- [61] CMS Collaboration, Technical proposal for the Phase-II upgrade of the Compact Muon Solenoid, CMS Technical Proposal, Report No. CERN-LHCC-2015-010, CMS-TDR-15-02, 2015.
- [62] W. Waltenberger, R. Frühwirth, and P. Vanlaer, Adaptive vertex fitting, *J. Phys. G* **34**, N343 (2007).
- [63] CMS Collaboration, Electron and photon reconstruction and identification with the CMS experiment at the CERN LHC, *J. Instrum.* **16**, P05014 (2021).
- [64] CMS Collaboration, Performance of the CMS muon detector and muon reconstruction with proton-proton collisions at $\sqrt{s} = 13$ TeV, *J. Instrum.* **13**, P06015 (2018).
- [65] CMS Collaboration, Jet energy scale and resolution in the CMS experiment in pp collisions at 8 TeV, *J. Instrum.* **12**, P02014 (2017).
- [66] CMS Collaboration, Identification of heavy-flavour jets with the CMS detector in pp collisions at 13 TeV, *J. Instrum.* **13**, P05011 (2018).
- [67] CMS Collaboration, A deep neural network for simultaneous estimation of b-jet energy and resolution, *Comput. Software Big Sci.* **4**, 10 (2020).
- [68] M. Cacciari, G. P. Salam, and G. Soyez, The anti- k_T jet clustering algorithm, *J. High Energy Phys.* **04** (2008) 063.
- [69] A. Larkoski, S. Marzani, G. Soyez, and J. Thaler, Soft drop, *J. High Energy Phys.* **05** (2014) 146.
- [70] CMS Collaboration, W and top tagging scale factors for run 2 data, CMS detector performance note, Report No. CMS-DP-2020-025, 2020.
- [71] CMS Collaboration, Performance of missing transverse momentum reconstruction in proton-proton collisions at $\sqrt{s} = 13$ TeV using the CMS detector, *J. Instrum.* **14**, P07004 (2019).
- [72] A. D. Bukin, Fitting function for asymmetric peaks, [arXiv:0711.4449](https://arxiv.org/abs/0711.4449).
- [73] I. J. Goodfellow, Y. Bengio, and A. Courville, *Deep Learning* (MIT Press, Cambridge, MA, USA, 2016).
- [74] P. K. Diederik and B. Jimmy, Adam: A method for stochastic optimisation, [arXiv:1412.6980](https://arxiv.org/abs/1412.6980).
- [75] J. Butterworth *et al.*, PDF4LHC recommendations for LHC run II, *J. Phys. G* **43**, 040 (2016).
- [76] CMS Collaboration, Measurement of the inclusive and differential WZ production cross sections, polarization angles, and triple gauge couplings in pp collisions at $\sqrt{s} = 13$ TeV, *J. High Energy Phys.* **07** (2022) 032.
- [77] CMS Collaboration, Measurements of $pp \rightarrow ZZ$ production cross sections and constraints on anomalous triple gauge couplings at $\sqrt{s} = 13$ TeV, *Eur. Phys. J. C* **81**, 200 (2021).
- [78] CMS Collaboration, Measurement of the inelastic proton-proton cross section at $\sqrt{s} = 13$ TeV, *J. High Energy Phys.* **07** (2018) 161.
- [79] R. Barlow and C. Beeston, Fitting using finite Monte Carlo samples, *Comput. Phys. Commun.* **77**, 219 (1993).

A. Tumasyan^{1,b}, W. Adam², J. W. Andrejkovic², T. Bergauer², S. Chatterjee², K. Damanakis², M. Dragicevic², A. Escalante Del Valle², P. S. Hussain², M. Jeitler^{2,c}, N. Krammer², L. Lechner², D. Liko², I. Mikulec², P. Paulitsch², J. Schieck^{2,c}, R. Schöffbeck², D. Schwarz², M. Sonawane², S. Templ², W. Waltenberger², C.-E. Wulz^{2,c}, M. R. Darwish^{3,d}, T. Janssen^{3,d}, T. Kello^{3,e}, H. Rejeb Sfar³, P. Van Mechelen³, E. S. Bols⁴, J. D'Hondt⁴, A. De Moor⁴, M. Delcourt⁴, H. El Faham⁴, S. Lowette⁴, A. Morton⁴, D. Müller⁴, A. R. Sahasransu⁴, S. Tavernier⁴, W. Van Doninck⁴, S. Van Putte⁴, D. Vannerom⁴, B. Clerbaux⁵, G. De Lentdecker⁵, L. Favart⁵, D. Hohov⁵, J. Jaramillo⁵, K. Lee⁵, M. Mahdavihorrani⁵, I. Makarenko⁵, A. Malara⁵, S. Paredes⁵, L. Pétré⁵, N. Postiau⁵, L. Thomas⁵, M. Vanden Bemden⁵, C. Vander Velde⁵, P. Vanlaer⁵, D. Dobur⁶, J. Knolle⁶, L. Lambrecht⁶, G. Mestdach⁶, C. Rendón⁶, A. Samalan⁶, K. Skovpen⁶, M. Tytgat⁶, N. Van Den Bossche⁶, B. Vermassen⁶, L. Wezenbeek⁶, A. Benecke⁷, G. Bruno⁷, F. Bury⁷, C. Caputo⁷, P. David⁷, C. Delaere⁷, I. S. Donertas⁷, A. Giammanco⁷, K. Jaffel⁷, Sa. Jain⁷, V. Lemaître⁷, K. Mondal⁷, A. Taliencio⁷, T. T. Tran⁷, P. Vischia⁷, S. Wertz⁷, G. A. Alves⁸, E. Coelho⁸, C. Hensel⁸, A. Moraes⁸, P. Rebello Teles⁸, W. L. Aldá Júnior⁹, M. Alves Gallo Pereira⁹, M. Barroso Ferreira Filho⁹, H. Brandao Malbouisson⁹, W. Carvalho⁹, J. Chinellato^{9,f}, E. M. Da Costa⁹, G. G. Da Silveira^{9,g}, D. De Jesus Damiao⁹, V. Dos Santos Sousa⁹, S. Fonseca De Souza⁹, J. Martins^{9,h}, C. Mora Herrera⁹, K. Mota Amarilo⁹, L. Mundim⁹, H. Nogima⁹, A. Santoro⁹, S. M. Silva Do Amaral⁹, A. Sznajder⁹, M. Thiel⁹, A. Vilela Pereira⁹, C. A. Bernardes^{10,g}, L. Calligaris¹⁰, T. R. Fernandez Perez Tomei¹⁰, E. M. Gregores¹⁰, P. G. Mercadante¹⁰, S. F. Novaes¹⁰, Sandra S. Padula¹⁰, A. Aleksandrov¹¹, G. Antchev¹¹, R. Hadjiiska¹¹, P. Iaydjiev¹¹, M. Misheva¹¹, M. Rodozov¹¹, M. Shopova¹¹, G. Sultanov¹¹, A. Dimitrov¹², T. Ivanov¹², L. Litov¹², B. Pavlov¹², P. Petkov¹², A. Petrov¹², E. Shumka¹², S. Thakur¹³, T. Cheng¹⁴, T. Javaid^{14,i}, M. Mittal¹⁴, L. Yuan¹⁴, M. Ahmad¹⁵, G. Bauer^{15,j}, Z. Hu¹⁵, S. Lezki¹⁵, K. Yi^{15,k}, G. M. Chen^{16,i}, H. S. Chen^{16,i}, M. Chen^{16,i}, F. Iemmi¹⁶, C. H. Jiang¹⁶, A. Kapoor¹⁶, H. Liao¹⁶, Z.-A. Liu^{16,l}, V. Milosevic¹⁶, F. Monti¹⁶, R. Sharma¹⁶, J. Tao¹⁶, J. Thomas-Wilsker¹⁶, J. Wang¹⁶, H. Zhang¹⁶, J. Zhao¹⁶, A. Agapitos¹⁷

Y. An¹⁷, Y. Ban¹⁷, A. Levin¹⁷, C. Li¹⁷, Q. Li¹⁷, X. Lyu¹⁷, Y. Mao¹⁷, S. J. Qian¹⁷, X. Sun¹⁷, D. Wang¹⁷, J. Xiao¹⁷, H. Yang¹⁷, M. Lu¹⁸, Z. You¹⁸, N. Lu¹⁹, X. Gao^{20,e}, D. Leggat²⁰, H. Okawa²⁰, Y. Zhang²⁰, Z. Lin²¹, C. Lu²¹, M. Xiao²¹, C. Avila²², D. A. Barbosa Trujillo²², A. Cabrera²², C. Florez²², J. Fraga²², J. Mejia Guisao²³, F. Ramirez²³, M. Rodriguez²³, J. D. Ruiz Alvarez²³, D. Giljanovic²⁴, N. Godinovic²⁴, D. Lelas²⁴, I. Puljak²⁴, Z. Antunovic²⁵, M. Kovac²⁵, T. Sculac²⁵, V. Brigljevic²⁶, B. K. Chitroda²⁶, D. Ferencek²⁶, S. Mishra²⁶, M. Roguljic²⁶, A. Starodumov^{26,m}, T. Susa²⁶, A. Attikis²⁷, K. Christoforou²⁷, S. Konstantinou²⁷, J. Mousa²⁷, C. Nicolaou²⁷, F. Ptochos²⁷, P. A. Razis²⁷, H. Rykaczewski²⁷, H. Saka²⁷, A. Stepennov²⁷, M. Finger^{28,m}, M. Finger Jr.^{28,m}, A. Kveton²⁸, E. Ayala²⁹, E. Carrera Jarrin³⁰, Y. Assran^{31,n,o}, S. Elgammal^{31,o}, M. A. Mahmoud³², Y. Mohammed³², S. Bhowmik³³, R. K. Dewanjee³³, K. Ehataht³³, M. Kadastik³³, T. Lange³³, S. Nandan³³, C. Nielsen³³, J. Pata³³, M. Raidal³³, L. Tani³³, C. Veelken³³, P. Eerola³⁴, H. Kirschenmann³⁴, K. Osterberg³⁴, M. Voutilainen³⁴, S. Bharthuar³⁵, E. Brücken³⁵, F. Garcia³⁵, J. Havukainen³⁵, M. S. Kim³⁵, R. Kinnunen³⁵, T. Lampén³⁵, K. Lassila-Perini³⁵, S. Lehti³⁵, T. Lindén³⁵, M. Lotti³⁵, L. Martikainen³⁵, M. Myllymäki³⁵, M. m. Rantanen³⁵, H. Siikonen³⁵, E. Tuominen³⁵, J. Tuominiemi³⁵, P. Luukka³⁶, H. Petrow³⁶, T. Tuuva^{36,a}, C. Amendola³⁷, M. Besancon³⁷, F. Couderc³⁷, M. Dejardin³⁷, D. Denegri³⁷, J. L. Faure³⁷, F. Ferri³⁷, S. Ganjour³⁷, P. Gras³⁷, G. Hamel de Monchenault³⁷, V. Lohezic³⁷, J. Malcles³⁷, J. Rander³⁷, A. Rosowsky³⁷, M. Ö. Sahin³⁷, A. Savoy-Navarro^{37,p}, P. Simkina³⁷, M. Titov³⁷, C. Baldenegro Barrera³⁸, F. Beaudette³⁸, A. Buchot Perraguin³⁸, P. Busson³⁸, A. Cappati³⁸, C. Charlot³⁸, F. Damas³⁸, O. Davignon³⁸, B. Diab³⁸, G. Falmagne³⁸, B. A. Fontana Santos Alves³⁸, S. Ghosh³⁸, R. Granier de Cassagnac³⁸, A. Hakimi³⁸, B. Harikrishnan³⁸, G. Liu³⁸, J. Motta³⁸, M. Nguyen³⁸, C. Ochando³⁸, L. Portales³⁸, R. Salerno³⁸, U. Sarkar³⁸, J. B. Sauvan³⁸, Y. Sirois³⁸, A. Tarabini³⁸, E. Vernazza³⁸, A. Zabi³⁸, A. Zghiche³⁸, J.-L. Agram^{39,q}, J. Andrea³⁹, D. Apparuto³⁹, D. Bloch³⁹, G. Bourgatte³⁹, J.-M. Brom³⁹, E. C. Chabert³⁹, C. Collard³⁹, D. Darej³⁹, U. Goerlach³⁹, C. Grimault³⁹, A.-C. Le Bihan³⁹, P. Van Hove³⁹, S. Beauceron⁴⁰, B. Blancon⁴⁰, G. Boudoul⁴⁰, A. Carle⁴⁰, N. Chanon⁴⁰, J. Choi⁴⁰, D. Contardo⁴⁰, P. Depasse⁴⁰, C. Dozen^{40,r}, H. El Mamouni⁴⁰, J. Fay⁴⁰, S. Gascon⁴⁰, M. Gouzevitch⁴⁰, G. Grenier⁴⁰, B. Ille⁴⁰, I. B. Laktineh⁴⁰, M. Lethuillier⁴⁰, L. Mirabito⁴⁰, S. Perries⁴⁰, L. Torterotot⁴⁰, M. Vander Donckt⁴⁰, P. Verdier⁴⁰, S. Viret⁴⁰, D. Lomidze⁴¹, I. Lomidze⁴¹, Z. Tsamalaidze^{41,m}, V. Botta⁴², L. Feld⁴², K. Klein⁴², M. Lipinski⁴², D. Meuser⁴², A. Pauls⁴², N. Röwert⁴², M. Teroerde⁴², S. Diekmann⁴³, A. Dodonova⁴³, N. Eich⁴³, D. Eliseev⁴³, M. Erdmann⁴³, P. Fackeldey⁴³, D. Fasanella⁴³, B. Fischer⁴³, T. Hebbeker⁴³, K. Hoepfner⁴³, F. Ivone⁴³, M. y. Lee⁴³, L. Mastrolorenzo⁴³, M. Merschmeyer⁴³, A. Meyer⁴³, S. Mondal⁴³, S. Mukherjee⁴³, D. Noll⁴³, A. Novak⁴³, F. Nowotny⁴³, A. Pozdnyakov⁴³, Y. Rath⁴³, W. Redjeb⁴³, F. Rehm⁴³, H. Reithler⁴³, A. Schmidt⁴³, S. C. Schuler⁴³, A. Sharma⁴³, A. Stein⁴³, F. Torres Da Silva De Araujo^{43,s}, L. Vigilante⁴³, S. Wiedenbeck⁴³, S. Zaleski⁴³, C. Dziwok⁴⁴, G. Flügge⁴⁴, W. Haj Ahmad^{44,t}, O. Hlushchenko⁴⁴, T. Kress⁴⁴, A. Nowack⁴⁴, O. Pooth⁴⁴, A. Stahl⁴⁴, T. Ziemons⁴⁴, A. Zotz⁴⁴, H. Aarup Petersen⁴⁵, M. Aldaya Martin⁴⁵, J. Alimena⁴⁵, P. Asmuss⁴⁵, S. Baxter⁴⁵, M. Bayatmakou⁴⁵, H. Becerril Gonzalez⁴⁵, O. Behnke⁴⁵, S. Bhattacharya⁴⁵, F. Blekman^{45,u}, K. Borras^{45,v}, D. Brunner⁴⁵, A. Campbell⁴⁵, A. Cardini⁴⁵, C. Cheng⁴⁵, F. Colombina⁴⁵, S. Consuegra Rodríguez⁴⁵, G. Correia Silva⁴⁵, M. De Silva⁴⁵, G. Eckerlin⁴⁵, D. Eckstein⁴⁵, L. I. Estevez Banos⁴⁵, O. Filatov⁴⁵, E. Gallo^{45,u}, A. Geiser⁴⁵, A. Giralaldi⁴⁵, G. Greau⁴⁵, A. Grohsjean⁴⁵, V. Guglielmi⁴⁵, M. Guthoff⁴⁵, A. Jafari^{45,w}, N. Z. Jomhari⁴⁵, B. Kaech⁴⁵, M. Kasemann⁴⁵, H. Kaveh⁴⁵, C. Kleinwort⁴⁵, R. Kogler⁴⁵, M. Komm⁴⁵, D. Krücker⁴⁵, W. Lange⁴⁵, D. Leyva Pernia⁴⁵, K. Lipka^{45,x}, W. Lohmann^{45,y}, R. Mankel⁴⁵, I.-A. Melzer-Pellmann⁴⁵, M. Mendizabal Morentin⁴⁵, J. Metwally⁴⁵, A. B. Meyer⁴⁵, G. Milella⁴⁵, M. Mormile⁴⁵, A. Mussgiller⁴⁵, A. Nürnberg⁴⁵, Y. Otari⁴⁵, D. Pérez Adán⁴⁵, E. Ranken⁴⁵, A. Raspereza⁴⁵, B. Ribeiro Lopes⁴⁵, J. Rübenach⁴⁵, A. Saggio⁴⁵, M. Savitskyi⁴⁵, M. Scham^{45,z,v}, V. Scheurer⁴⁵, S. Schnake^{45,v}, P. Schütze⁴⁵, C. Schwanenberger^{45,u}, M. Shchedrolosiev⁴⁵, R. E. Sosa Ricardo⁴⁵, D. Stafford⁴⁵, N. Tonon^{45,a}, M. Van De Klundert⁴⁵, F. Vazzoler⁴⁵, A. Velyka⁴⁵, A. Ventura Barroso⁴⁵, R. Walsh⁴⁵, D. Walter⁴⁵, Q. Wang⁴⁵, Y. Wen⁴⁵, K. Wichmann⁴⁵, L. Wiens^{45,v}, C. Wissing⁴⁵, S. Wuchterl⁴⁵, Y. Yang⁴⁵, A. Zimmermann Castro Santos⁴⁵, A. Albrecht⁴⁶, S. Albrecht⁴⁶, M. Antonello⁴⁶, S. Bein⁴⁶, L. Benato⁴⁶, M. Bonanomi⁴⁶, P. Connor⁴⁶, K. De Leo⁴⁶, M. Eich⁴⁶, K. El Morabit⁴⁶, F. Feindt⁴⁶, A. Fröhlich⁴⁶, C. Garbers⁴⁶, E. Garutti⁴⁶, M. Hajheidari⁴⁶, J. Haller⁴⁶, A. Hinzmann⁴⁶, H. R. Jabusch⁴⁶, G. Kasieczka⁴⁶, P. Keicher⁴⁶, R. Klanner⁴⁶, W. Korcari⁴⁶, T. Kramer⁴⁶, V. Kutzner⁴⁶, F. Labe⁴⁶, J. Lange⁴⁶, A. Lobanov⁴⁶, C. Matthies⁴⁶

- A. Mehta⁴⁶, L. Moureaux⁴⁶, M. Mrowietz⁴⁶, A. Nigamova⁴⁶, Y. Nissan⁴⁶, A. Paasch⁴⁶, K. J. Pena Rodriguez⁴⁶, T. Quadfasel⁴⁶, M. Rieger⁴⁶, O. Rieger⁴⁶, D. Savoie⁴⁶, J. Schindler⁴⁶, P. Schleper⁴⁶, M. Schröder⁴⁶, J. Schwandt⁴⁶, M. Sommerhalder⁴⁶, H. Stadie⁴⁶, G. Steinbrück⁴⁶, A. Tews⁴⁶, M. Wolf⁴⁶, S. Brommer⁴⁷, M. Burkart⁴⁷, E. Butz⁴⁷, T. Chwalek⁴⁷, A. Dierlamm⁴⁷, A. Droll⁴⁷, N. Faltermann⁴⁷, M. Giffels⁴⁷, J. O. Gosewisch⁴⁷, A. Gottmann⁴⁷, F. Hartmann^{47,aa}, M. Horzela⁴⁷, U. Husemann⁴⁷, M. Klute⁴⁷, R. Koppenhöfer⁴⁷, M. Link⁴⁷, A. Lintuluoto⁴⁷, S. Maier⁴⁷, S. Mitra⁴⁷, Th. Müller⁴⁷, M. Neukum⁴⁷, M. Oh⁴⁷, G. Quast⁴⁷, K. Rabbertz⁴⁷, J. Rauser⁴⁷, I. Shvetsov⁴⁷, H. J. Simonis⁴⁷, N. Trevisani⁴⁷, R. Ulrich⁴⁷, J. van der Linden⁴⁷, R. F. Von Cube⁴⁷, M. Wassmer⁴⁷, S. Wieland⁴⁷, R. Wolf⁴⁷, S. Wozniowski⁴⁷, S. Wunsch⁴⁷, X. Zuo⁴⁷, G. Anagnostou⁴⁸, P. Assiouras⁴⁸, G. Daskalakis⁴⁸, A. Kyriakis⁴⁸, A. Stakia⁴⁸, M. Diamantopoulou⁴⁹, D. Karasavvas⁴⁹, P. Kontaxakis⁴⁹, A. Manousakis-Katsikakis⁴⁹, A. Panagiotou⁴⁹, I. Papavergou⁴⁹, N. Saoulidou⁴⁹, K. Theofilatos⁴⁹, E. Tziaferi⁴⁹, K. Vellidis⁴⁹, I. Zisopoulos⁴⁹, G. Bakas⁵⁰, T. Chatzistavrou⁵⁰, G. Karapostoli⁵⁰, K. Kousouris⁵⁰, I. Papakrivopoulos⁵⁰, G. Tsiolitis⁵⁰, A. Zacharopoulou⁵⁰, K. Adamidis⁵¹, I. Bestintzanos⁵¹, I. Evangelou⁵¹, C. Foudas⁵¹, P. Gianneios⁵¹, C. Kamtsikis⁵¹, P. Katsoulis⁵¹, P. Kokkas⁵¹, P. G. Kosmoglou Kioseoglou⁵¹, N. Manthos⁵¹, I. Papadopoulos⁵¹, J. Strologas⁵¹, M. Bartók^{52,bb}, G. Bencze⁵², C. Hajdu⁵², D. Horvath^{52,cc,dd}, F. Sikler⁵², V. Veszpremi⁵², M. Csanád⁵³, K. Farkas⁵³, M. M. A. Gadallah^{53,ee}, S. Lökös^{53,ff}, P. Major⁵³, K. Mandal⁵³, G. Pásztor⁵³, A. J. Rádl^{53,gg}, O. Surányi⁵³, G. I. Veres⁵³, N. Beni⁵⁴, S. Czellar⁵⁴, J. Karacsi^{54,bb}, J. Molnar⁵⁴, Z. Szillasi⁵⁴, D. Teyssier⁵⁴, P. Raics⁵⁵, B. Ujvari^{55,hh}, G. Zilizi⁵⁵, T. Csorgo^{56,gg}, F. Nemes^{56,gg}, T. Novak⁵⁶, J. Babbar⁵⁷, S. Bansal⁵⁷, S. B. Beri⁵⁷, V. Bhatnagar⁵⁷, G. Chaudhary⁵⁷, S. Chauhan⁵⁷, N. Dhingra^{57,ii}, R. Gupta⁵⁷, A. Kaur⁵⁷, A. Kaur⁵⁷, H. Kaur⁵⁷, M. Kaur⁵⁷, S. Kumar⁵⁷, P. Kumari⁵⁷, M. Meena⁵⁷, K. Sandeep⁵⁷, T. Sheokand⁵⁷, J. B. Singh^{57,jj}, A. Singla⁵⁷, A. Ahmed⁵⁸, A. Bhardwaj⁵⁸, A. Chhetri⁵⁸, B. C. Choudhary⁵⁸, A. Kumar⁵⁸, M. Naimuddin⁵⁸, K. Ranjan⁵⁸, S. Saumya⁵⁸, S. Baradia⁵⁹, S. Barman^{59,kk}, S. Bhattacharya⁵⁹, D. Bhowmik⁵⁹, S. Dutta⁵⁹, S. Dutta⁵⁹, B. Gumber^{59,ll}, M. Maity^{59,kk}, P. Palit⁵⁹, G. Saha⁵⁹, B. Sahu⁵⁹, S. Sarkar⁵⁹, P. K. Behera⁶⁰, S. C. Behera⁶⁰, S. Chatterjee⁶⁰, P. Kalbhor⁶⁰, J. R. Komaragiri^{60,mm}, D. Kumar^{60,mm}, A. Muhammad⁶⁰, L. Panwar^{60,mm}, R. Pradhan⁶⁰, P. R. Pujahari⁶⁰, N. R. Saha⁶⁰, A. Sharma⁶⁰, A. K. Sikdar⁶⁰, S. Verma⁶⁰, K. Naskar⁶⁰, T. Aziz⁶², I. Das⁶², S. Dugad⁶², M. Kumar⁶², G. B. Mohanty⁶², P. Suryadevara⁶², S. Banerjee⁶³, M. Guchait⁶³, S. Karmakar⁶³, S. Kumar⁶³, G. Majumder⁶³, K. Mazumdar⁶³, S. Mukherjee⁶³, A. Thachayath⁶³, S. Bahinipati^{64,oo}, A. K. Das⁶⁴, C. Kar⁶⁴, P. Mal⁶⁴, T. Mishra⁶⁴, V. K. Muraleedharan Nair Bindhu^{64,pp}, A. Nayak^{64,pp}, P. Saha⁶⁴, S. K. Swain⁶⁴, D. Vats^{64,pp}, A. Alpana⁶⁵, S. Dube⁶⁵, B. Kansal⁶⁵, A. Laha⁶⁵, S. Pandey⁶⁵, A. Rastogi⁶⁵, S. Sharma⁶⁵, H. Bakhshiansohi^{66,qq,rr}, E. Khazaie^{66,rr}, M. Zeinali^{66,ss}, S. Chenarani^{67,tt}, S. M. Etesami⁶⁷, M. Khakzad⁶⁷, M. Mohammadi Najafabadi⁶⁷, M. Grunewald⁶⁸, M. Abbrescia^{69a,69b}, R. Aly^{69a,69b,uu}, C. Aruta^{69a,69b}, A. Colaleo^{69a}, D. Creanza^{69a,69c}, L. Cristella^{69a,69b}, N. De Filippis^{69a,69c}, M. De Palma^{69a,69b}, A. Di Florio^{69a,69b}, W. Elmetenawee^{69a,69b}, F. Errico^{69a,69b}, L. Fiore^{69a}, G. Iaselli^{69a,69c}, G. Maggi^{69a,69c}, M. Maggi^{69a}, I. Margjeka^{69a,69b}, V. Mastrapasqua^{69a,69b}, S. My^{69a,69b}, S. Nuzzo^{69a,69b}, A. Pellecchia^{69a,69b}, A. Pompili^{69a,69b}, G. Pugliese^{69a,69c}, R. Radogna^{69a}, D. Ramos^{69a}, A. Ranieri^{69a}, G. Selvaggi^{69a,69b}, L. Silvestris^{69a}, F. M. Simone^{69a,69b}, Ü. Sözbilir^{69a}, A. Stamerra^{69a}, R. Venditti^{69a}, P. Verwilligen^{69a}, G. Abbiendi^{70a}, C. Battilana^{70a,70b}, D. Bonacorsi^{70a,70b}, L. Borgonovi^{70a}, L. Brigliadori^{70a}, R. Campanini^{70a,70b}, P. Capiluppi^{70a,70b}, A. Castro^{70a,70b}, F. R. Cavallo^{70a}, M. Cuffiani^{70a,70b}, G. M. Dallavalle^{70a}, T. Diotallevi^{70a,70b}, F. Fabbri^{70a}, A. Fanfani^{70a,70b}, P. Giacomelli^{70a}, L. Giommi^{70a,70b}, C. Grandi^{70a}, L. Guiducci^{70a,70b}, S. Lo Meo^{70a,vv}, L. Lunerti^{70a,70b}, S. Marcellini^{70a}, G. Masetti^{70a}, F. L. Navarria^{70a,70b}, A. Perrotta^{70a}, F. Primavera^{70a,70b}, A. M. Rossi^{70a,70b}, T. Rovelli^{70a,70b}, G. P. Siroli^{70a,70b}, S. Costa^{71a,71b,ww}, A. Di Mattia^{71a}, R. Potenza^{71a,71b}, A. Tricomi^{71a,71b,ww}, C. Tuve^{71a,71b}, G. Barbagli^{72a}, G. Bardelli^{72a,72b}, B. Camaiani^{72a,72b}, A. Cassese^{72a}, R. Ceccarelli^{72a,72b}, V. Ciulli^{72a,72b}, C. Civinini^{72a}, R. D'Alessandro^{72a,72b}, E. Focardi^{72a,72b}, G. Latino^{72a,72b}, P. Lenzi^{72a,72b}, M. Lizzo^{72a,72b}, M. Meschini^{72a}, S. Paoletti^{72a}, G. Sguazzoni^{72a}, L. Viliani^{72a}, L. Benussi⁷³, S. Bianco⁷³, S. Meola^{73,xx}, D. Piccolo⁷³, M. Bozzo^{74a,74b}, P. Chatagnon^{74a}, F. Ferro^{74a}, E. Robutti^{74a}, S. Tosi^{74a,74b}, A. Benaglia^{75a}, G. Boldrini^{75a}, F. Brivio^{75a,75b}, F. Ceteorelli^{75a,75b}, F. De Guio^{75a,75b}, M. E. Dinardo^{75a,75b}, P. Dini^{75a}, S. Gennai^{75a}, A. Ghezzi^{75a,75b}, P. Govoni^{75a,75b}, L. Guzzi^{75a,75b}, M. T. Lucchini^{75a,75b}, M. Malberti^{75a}, S. Malvezzi^{75a}, A. Massironi^{75a}, D. Menasce^{75a}, L. Moroni^{75a}, M. Paganoni^{75a,75b}, D. Pedrini^{75a}, B. S. Pinolini^{75a}, S. Ragazzi^{75a,75b}, N. Redaelli^{75a}, T. Tabarelli de Fatis^{75a,75b}

D. Zuolo^{75a,75b} S. Buontempo^{76a} F. Carnevali^{76a,76b} N. Cavallo^{76a,76c} A. De Iorio^{76a,76b} F. Fabozzi^{76a,76c}
 A. O. M. Iorio^{76a,76b} L. Lista^{76a,76b,yy} P. Paolucci^{76a,aa} B. Rossi^{76a} C. Sciacca^{76a,76b} P. Azzi^{77a}
 N. Bacchetta^{77a,zz} D. Bisello^{77a,77b} P. Bortignon^{77a} A. Bragagnolo^{77a,77b} R. Carlin^{77a,77b} P. Checchia^{77a}
 T. Dorigo^{77a} F. Gasparini^{77a,77b} G. Govi^{77a} A. Gozzelino^{77a} G. Grosso^{77a} L. Layer^{77a,aaa} E. Lusiani^{77a}
 M. Margoni^{77a,77b} J. Pazzini^{77a,77b} P. Ronchese^{77a,77b} R. Rossin^{77a,77b} F. Simonetto^{77a,77b} G. Strong^{77a}
 M. Tosi^{77a,77b} H. Yarar^{77a,77b} M. Zanetti^{77a,77b} P. Zotto^{77a,77b} A. Zucchetta^{77a,77b} G. Zumerle^{77a,77b}
 S. Abu Zeid^{78a,bbb} C. Aimè^{78a,78b} A. Braghieri^{78a} S. Calzaferri^{78a,78b} D. Fiorina^{78a,78b} P. Montagna^{78a,78b}
 V. Re^{78a} C. Riccardi^{78a,78b} P. Salvini^{78a} I. Vai^{78a} P. Vitulo^{78a,78b} P. Asenov^{79a,ccc} G. M. Bilei^{79a}
 D. Ciangottini^{79a,79b} L. Fanò^{79a,79b} M. Magherini^{79a,79b} G. Mantovani^{79a,79b} V. Mariani^{79a,79b} M. Menichelli^{79a}
 F. Moscatelli^{79a,ccc} A. Piccinelli^{79a,79b} M. Presilla^{79a,79b} A. Rossi^{79a,79b} A. Santocchia^{79a,79b} D. Spiga^{79a}
 T. Tedeschi^{79a,79b} P. Azzurri^{80a} G. Bagliesi^{80a} V. Bertacchi^{80a,80c} R. Bhattacharya^{80a} L. Bianchini^{80a,80b}
 T. Boccali^{80a} E. Bossini^{80a,80b} D. Bruschini^{80a,80c} R. Castaldi^{80a} M. A. Ciocci^{80a,80b} V. D'Amante^{80a,80d}
 R. Dell'Orso^{80a} S. Donato^{80a} A. Giassi^{80a} F. Ligabue^{80a,80c} D. Matos Figueiredo^{80a} A. Messineo^{80a,80b}
 M. Musich^{80a,80b} F. Palla^{80a} S. Parolia^{80a} G. Ramirez-Sanchez^{80a,80c} A. Rizzi^{80a,80b} G. Rolandi^{80a,80c}
 S. Roy Chowdhury^{80a} T. Sarkar^{80a} A. Scribano^{80a} P. Spagnolo^{80a} R. Tenchini^{80a} G. Tonelli^{80a,80b}
 N. Turini^{80a,80d} A. Venturi^{80a} P. G. Verdini^{80a} P. Barria^{81a} M. Campana^{81a,81b} F. Cavallari^{81a} D. Del Re^{81a,81b}
 E. Di Marco^{81a} M. Diemoz^{81a} E. Longo^{81a,81b} P. Meridiani^{81a} G. Organtini^{81a,81b} F. Pandolfi^{81a}
 R. Paramatti^{81a,81b} C. Quaranta^{81a,81b} S. Rahatlou^{81a,81b} C. Rovelli^{81a} F. Santanastasio^{81a,81b} L. Soffi^{81a}
 R. Tramontano^{81a,81b} N. Amapane^{82a,82b} R. Arcidiacono^{82a,82c} S. Argiro^{82a,82b} M. Arnedo^{82a,82c} N. Bartosik^{82a}
 R. Bellan^{82a,82b} A. Bellora^{82a,82b} C. Biino^{82a} N. Cartiglia^{82a} M. Costa^{82a,82b} R. Covarelli^{82a,82b} N. Demaria^{82a}
 M. Grippo^{82a,82b} B. Kiani^{82a,82b} F. Legger^{82a} C. Mariotti^{82a} S. Maselli^{82a} A. Mecca^{82a,82b} E. Migliore^{82a,82b}
 M. Monteno^{82a} R. Mulargia^{82a} M. M. Obertino^{82a,82b} G. Ortona^{82a} L. Pacher^{82a,82b} N. Pastrone^{82a}
 M. Pelliccioni^{82a} M. Ruspa^{82a,82c} K. Shchelina^{82a} F. Siviero^{82a,82b} V. Sola^{82a,82b} A. Solano^{82a,82b}
 D. Soldi^{82a,82b} A. Staiano^{82a} M. Tornago^{82a,82b} D. Trocino^{82a} G. Umoret^{82a,82b} A. Vagnerini^{82a,82b}
 E. Vlasov^{82a,82b} S. Belforte^{83a} V. Candelise^{83a,83b} M. Casarsa^{83a} F. Cossutti^{83a} G. Della Ricca^{83a,83b}
 G. Sorrentino^{83a,83b} S. Dogra⁸⁴ C. Huh⁸⁴ B. Kim⁸⁴ D. H. Kim⁸⁴ G. N. Kim⁸⁴ J. Kim⁸⁴ J. Lee⁸⁴
 S. W. Lee⁸⁴ C. S. Moon⁸⁴ Y. D. Oh⁸⁴ S. I. Pak⁸⁴ M. S. Ryu⁸⁴ S. Sekmen⁸⁴ Y. C. Yang⁸⁴ H. Kim⁸⁵
 D. H. Moon⁸⁵ E. Asilar⁸⁶ T. J. Kim⁸⁶ J. Park⁸⁶ S. Choi⁸⁷ S. Han⁸⁷ B. Hong⁸⁷ K. Lee⁸⁷ K. S. Lee⁸⁷ J. Lim⁸⁷
 J. Park⁸⁷ S. K. Park⁸⁷ J. Yoo⁸⁷ J. Goh⁸⁸ H. S. Kim⁸⁹ Y. Kim⁸⁹ S. Lee⁸⁹ J. Almond⁹⁰ J. H. Bhyun⁹⁰ J. Choi⁹⁰
 S. Jeon⁹⁰ J. Kim⁹⁰ J. S. Kim⁹⁰ S. Ko⁹⁰ H. Kwon⁹⁰ H. Lee⁹⁰ S. Lee⁹⁰ B. H. Oh⁹⁰ S. B. Oh⁹⁰ H. Seo⁹⁰
 U. K. Yang⁹⁰ I. Yoon⁹⁰ W. Jang⁹¹ D. Y. Kang⁹¹ Y. Kang⁹¹ D. Kim⁹¹ S. Kim⁹¹ B. Ko⁹¹ J. S. H. Lee⁹¹
 Y. Lee⁹¹ J. A. Merlin⁹¹ I. C. Park⁹¹ Y. Roh⁹¹ D. Song⁹¹ I. J. Watson⁹¹ S. Yang⁹¹ S. Ha⁹² H. D. Yoo⁹²
 M. Choi⁹³ M. R. Kim⁹³ H. Lee⁹³ Y. Lee⁹³ I. Yu⁹³ T. Beyrouthy⁹⁴ Y. Maghrbi⁹⁴ K. Dreimanis⁹⁵ G. Pikurs⁹⁵
 A. Potrebko⁹⁵ M. Seidel⁹⁵ V. Veckalns^{95,ddd} M. Ambrozias⁹⁶ A. Carvalho Antunes De Oliveira⁹⁶
 A. Juodagalvis⁹⁶ A. Rinkevicius⁹⁶ G. Tamulaitis⁹⁶ N. Bin Norjoharuddeen⁹⁷ S. Y. Hoh^{97,eee} I. Yusuff^{97,eee}
 Z. Zolkapli⁹⁷ J. F. Benitez⁹⁸ A. Castaneda Hernandez⁹⁸ H. A. Encinas Acosta⁹⁸ L. G. Gallegos Maríñez⁹⁸
 M. León Coello⁹⁸ J. A. Murillo Quijada⁹⁸ A. Sehrawat⁹⁸ L. Valencia Palomo⁹⁸ G. Ayala⁹⁹
 H. Castilla-Valdez⁹⁹ I. Heredia-De La Cruz^{99,fff} R. Lopez-Fernandez⁹⁹ C. A. Mondragon Herrera⁹⁹
 D. A. Perez Navarro⁹⁹ A. Sánchez Hernández⁹⁹ C. Oropeza Barrera¹⁰⁰ F. Vazquez Valencia¹⁰⁰ I. Pedraza¹⁰¹
 H. A. Salazar Ibarguen¹⁰¹ C. Uribe Estrada¹⁰¹ I. Bujanja¹⁰² J. Mijuskovic^{102,ggg} N. Raicevic¹⁰² A. Ahmad¹⁰³
 M. I. Asghar¹⁰³ A. Awais¹⁰³ M. I. M. Awan¹⁰³ M. Gul¹⁰³ H. R. Hoorani¹⁰³ W. A. Khan¹⁰³ V. Avati¹⁰⁴
 L. Grzanka¹⁰⁴ M. Malawski¹⁰⁴ H. Bialkowska¹⁰⁵ M. Bluj¹⁰⁵ B. Boimska¹⁰⁵ M. Górski¹⁰⁵ M. Kazana¹⁰⁵
 M. Szleper¹⁰⁵ P. Zalewski¹⁰⁵ K. Bunkowski¹⁰⁶ K. Doroba¹⁰⁶ A. Kalinowski¹⁰⁶ M. Konecki¹⁰⁶
 J. Krolikowski¹⁰⁶ M. Araujo¹⁰⁷ P. Bargassa¹⁰⁷ D. Bastos¹⁰⁷ A. Boletti¹⁰⁷ P. Faccioli¹⁰⁷ M. Gallinaro¹⁰⁷
 J. Hollar¹⁰⁷ N. Leonardo¹⁰⁷ T. Niknejad¹⁰⁷ M. Pisano¹⁰⁷ J. Seixas¹⁰⁷ J. Varela¹⁰⁷ P. Adzic^{108,hhh}
 M. Dordevic¹⁰⁸ P. Milenovic¹⁰⁸ J. Milosevic¹⁰⁸ M. Aguilar-Benitez¹⁰⁹ J. Alcaraz Maestre¹⁰⁹ M. Barrio Luna¹⁰⁹
 Cristina F. Bedoya¹⁰⁹ M. Cepeda¹⁰⁹ M. Cerrada¹⁰⁹ N. Colino¹⁰⁹ B. De La Cruz¹⁰⁹ A. Delgado Peris¹⁰⁹
 D. Fernández Del Val¹⁰⁹ J. P. Fernández Ramos¹⁰⁹ J. Flix¹⁰⁹ M. C. Fouz¹⁰⁹ O. Gonzalez Lopez¹⁰⁹
 S. Goy Lopez¹⁰⁹ J. M. Hernandez¹⁰⁹ M. I. Josa¹⁰⁹ J. León Holgado¹⁰⁹ D. Moran¹⁰⁹ C. Perez Dengra¹⁰⁹

A. Pérez-Calero Yzquierdo¹⁰⁹, J. Puerta Pelayo¹⁰⁹, I. Redondo¹⁰⁹, D.D. Redondo Ferrero¹⁰⁹, L. Romero¹⁰⁹, S. Sánchez Navas¹⁰⁹, J. Sastre¹⁰⁹, L. Urda Gómez¹⁰⁹, J. Vazquez Escobar¹⁰⁹, C. Willmott¹⁰⁹, J.F. de Trocóniz¹¹⁰, B. Alvarez Gonzalez¹¹¹, J. Cuevas¹¹¹, J. Fernandez Menendez¹¹¹, S. Folgueras¹¹¹, I. Gonzalez Caballero¹¹¹, J.R. González Fernández¹¹¹, E. Palencia Cortezon¹¹¹, C. Ramón Álvarez¹¹¹, V. Rodríguez Bouza¹¹¹, A. Soto Rodríguez¹¹¹, A. Trapote¹¹¹, C. Vico Villalba¹¹¹, J.A. Brochero Cifuentes¹¹², I.J. Cabrillo¹¹², A. Calderon¹¹², J. Duarte Campderros¹¹², M. Fernandez¹¹², C. Fernandez Madrazo¹¹², A. García Alonso¹¹², G. Gomez¹¹², C. Lasaos García¹¹², C. Martinez Rivero¹¹², P. Martinez Ruiz del Arbol¹¹², F. Matorras¹¹², P. Matorras Cuevas¹¹², J. Piedra Gomez¹¹², C. Prieels¹¹², L. Scodellaro¹¹², I. Vila¹¹², J.M. Vizan Garcia¹¹², M.K. Jayananda¹¹³, B. Kailasapathy^{113,iii}, D.U.J. Sonnadara¹¹³, D.D.C. Wickramaratna¹¹³, W.G.D. Dharmaratna^{114,iii}, K. Liyanage¹¹⁴, N. Perera¹¹⁴, N. Wickramage¹¹⁴, D. Abbaneo¹¹⁵, E. Auffray¹¹⁵, G. Auzinger¹¹⁵, J. Baechler¹¹⁵, P. Baillon^{115,a}, D. Barney¹¹⁵, J. Bendavid¹¹⁵, A. Bermúdez Martínez¹¹⁵, M. Bianco¹¹⁵, B. Bilin¹¹⁵, A.A. Bin Anuar¹¹⁵, A. Bocci¹¹⁵, E. Brondolin¹¹⁵, C. Caillol¹¹⁵, T. Camporesi¹¹⁵, G. Cerminara¹¹⁵, N. Chernyavskaya¹¹⁵, S.S. Chhibra¹¹⁵, S. Choudhury¹¹⁵, M. Cipriani¹¹⁵, D. d'Enterria¹¹⁵, A. Dabrowski¹¹⁵, A. David¹¹⁵, A. De Roeck¹¹⁵, M.M. Defranchis¹¹⁵, M. Deile¹¹⁵, M. Dobson¹¹⁵, M. Dünser¹¹⁵, N. Dupont¹¹⁵, F. Fallavollita^{115,kkk}, A. Florent¹¹⁵, L. Forthomme¹¹⁵, G. Franzoni¹¹⁵, W. Funk¹¹⁵, S. Ghosh¹¹⁵, S. Giani¹¹⁵, D. Gigi¹¹⁵, K. Gill¹¹⁵, F. Glege¹¹⁵, L. Gouskos¹¹⁵, E. Govorkova¹¹⁵, M. Haranko¹¹⁵, J. Hegeman¹¹⁵, V. Innocente¹¹⁵, T. James¹¹⁵, P. Janot¹¹⁵, J. Kaspar¹¹⁵, J. Kieseler¹¹⁵, N. Kratochwil¹¹⁵, S. Laurila¹¹⁵, P. Lecoq¹¹⁵, E. Leutgeb¹¹⁵, C. Lourenço¹¹⁵, B. Maier¹¹⁵, L. Malgeri¹¹⁵, M. Mannelli¹¹⁵, A.C. Marini¹¹⁵, F. Meijers¹¹⁵, S. Mersi¹¹⁵, E. Meschi¹¹⁵, F. Moortgat¹¹⁵, M. Mulders¹¹⁵, S. Orfanelli¹¹⁵, L. Orsini¹¹⁵, F. Pantaleo¹¹⁵, E. Perez¹¹⁵, M. Peruzzi¹¹⁵, A. Petrilli¹¹⁵, G. Petrucciani¹¹⁵, A. Pfeiffer¹¹⁵, M. Pierini¹¹⁵, D. Piparo¹¹⁵, M. Pitt¹¹⁵, H. Qu¹¹⁵, T. Quast¹¹⁵, D. Rabady¹¹⁵, A. Racz¹¹⁵, G. Reales Gutiérrez¹¹⁵, M. Rovere¹¹⁵, H. Sakulin¹¹⁵, J. Salfeld-Nebgen¹¹⁵, S. Scarfi¹¹⁵, M. Selvaggi¹¹⁵, A. Sharma¹¹⁵, P. Silva¹¹⁵, P. Sphicas^{115,iii}, A.G. Stahl Leitner¹¹⁵, S. Summers¹¹⁵, K. Tatar¹¹⁵, D. Treille¹¹⁵, P. Tropea¹¹⁵, A. Tsiros¹¹⁵, J. Wanczyk^{115,mmm}, K.A. Wozniak¹¹⁵, W.D. Zeuner¹¹⁵, L. Caminada^{116,nnn}, A. Ebrahimi¹¹⁶, W. Erdmann¹¹⁶, R. Horisberger¹¹⁶, Q. Ingram¹¹⁶, H.C. Kaestli¹¹⁶, D. Kotlinski¹¹⁶, C. Lange¹¹⁶, M. Missiroli^{116,nnn}, L. Noehte^{116,nnn}, T. Rohe¹¹⁶, T.K. Aarrestad¹¹⁷, K. Androsov^{117,mmm}, M. Backhaus¹¹⁷, A. Calandri¹¹⁷, K. Datta¹¹⁷, A. De Cosa¹¹⁷, G. Dissertori¹¹⁷, M. Dittmar¹¹⁷, M. Donegà¹¹⁷, F. Eble¹¹⁷, M. Galli¹¹⁷, K. Gedia¹¹⁷, F. Glessgen¹¹⁷, T.A. Gómez Espinosa¹¹⁷, C. Grab¹¹⁷, D. Hits¹¹⁷, W. Luster¹¹⁷, A.-M. Lyon¹¹⁷, R.A. Manzoni¹¹⁷, L. Marchese¹¹⁷, C. Martin Perez¹¹⁷, A. Mascellani^{117,mmm}, F. Nessi-Tedaldi¹¹⁷, J. Niedziela¹¹⁷, F. Pauss¹¹⁷, V. Perovic¹¹⁷, S. Pigazzini¹¹⁷, M.G. Ratti¹¹⁷, M. Reichmann¹¹⁷, C. Reissel¹¹⁷, T. Reitenspiess¹¹⁷, B. Ristic¹¹⁷, F. Riti¹¹⁷, D. Ruini¹¹⁷, D.A. Sanz Becerra¹¹⁷, R. Seidita¹¹⁷, J. Steggemann^{117,mmm}, D. Valsecchi¹¹⁷, R. Wallny¹¹⁷, C. Amsler^{118,ooo}, P. Bärtzsch¹¹⁸, C. Botta¹¹⁸, D. Brzhechko¹¹⁸, M.F. Canelli¹¹⁸, K. Cormier¹¹⁸, A. De Wit¹¹⁸, R. Del Burgo¹¹⁸, J.K. Heikkilä¹¹⁸, M. Huwiler¹¹⁸, W. Jin¹¹⁸, A. Jofrehei¹¹⁸, B. Kilminster¹¹⁸, S. Leontsinis¹¹⁸, S.P. Liechti¹¹⁸, A. Macchiolo¹¹⁸, P. Meiring¹¹⁸, V.M. Mikuni¹¹⁸, U. Molinatti¹¹⁸, I. Neutelings¹¹⁸, A. Reimers¹¹⁸, P. Robmann¹¹⁸, S. Sanchez Cruz¹¹⁸, K. Schweiger¹¹⁸, M. Senger¹¹⁸, Y. Takahashi¹¹⁸, C. Adloff^{119,ppp}, C.M. Kuo¹¹⁹, W. Lin¹¹⁹, P.K. Rout¹¹⁹, P.C. Tiwari^{119,mm}, S.S. Yu¹¹⁹, L. Ceard¹²⁰, Y. Chao¹²⁰, K.F. Chen¹²⁰, P. s. Chen¹²⁰, H. Cheng¹²⁰, W.-S. Hou¹²⁰, R. Khurana¹²⁰, G. Kole¹²⁰, Y. y. Li¹²⁰, R.-S. Lu¹²⁰, E. Paganis¹²⁰, A. Psallidas¹²⁰, A. Steen¹²⁰, H. y. Wu¹²⁰, E. Yazgan¹²⁰, C. Asawatangtrakuldee¹²¹, N. Srimanobhas¹²¹, V. Wachirapusanand¹²¹, D. Agyel¹²², F. Boran¹²², Z.S. Demiroglu¹²², F. Dolek¹²², I. Dumanoglu^{122,qqq}, E. Eskut¹²², Y. Guler^{122,rrr}, E. Gupinar Guler^{122,rrr}, C. Isik¹²², O. Kara¹²², A. Kayis Topaksu¹²², U. Kiminsu¹²², G. Onengut¹²², K. Ozdemir^{122,sss}, A. Polatoz¹²², A.E. Simsek¹²², B. Tali^{122,ttt}, U.G. Tok¹²², S. Turkcapar¹²², E. Uslan¹²², I.S. Zorbakir¹²², G. Karapinar^{123,uuu}, K. Ocalan^{123,vvv}, M. Yalvac^{123,www}, B. Akgun¹²⁴, I.O. Atakisi¹²⁴, E. Gülmez¹²⁴, M. Kaya^{124,xxx}, O. Kaya^{124,yyy}, S. Tekten^{124,zzz}, A. Cakir¹²⁵, K. Cankocak^{125,qqq}, Y. Komurcu¹²⁵, S. Sen^{125,aaaa}, O. Aydilek¹²⁶, S. Cerci^{126,ttt}, B. Haciosahinoglu¹²⁶, I. Hos^{126,bbbb}, B. Isildak^{126,cccc}, B. Kaynak¹²⁶, S. Ozkorucuklu¹²⁶, C. Simsek¹²⁶, D. Sunar Cerci^{126,ttt}, B. Grynyov¹²⁷, L. Levchuk¹²⁸, D. Anthony¹²⁹, J.J. Brooke¹²⁹, A. Bundock¹²⁹, E. Clement¹²⁹, D. Cussans¹²⁹, H. Flacher¹²⁹, M. Glowacki¹²⁹, J. Goldstein¹²⁹, H.F. Heath¹²⁹, L. Kreczko¹²⁹, B. Krikler¹²⁹, S. Paramesvaran¹²⁹, S. Seif El Nasr-Storey¹²⁹, V.J. Smith¹²⁹, N. Stylianou^{129,dddd}, K. Walkingshaw Pass¹²⁹, R. White¹²⁹, A.H. Ball¹³⁰, K.W. Bell¹³⁰, A. Belyaev^{130,eeee}, C. Brew¹³⁰, R.M. Brown¹³⁰

D. J. A. Cockerill¹³⁰, C. Cooke¹³⁰, K. V. Ellis¹³⁰, K. Harder¹³⁰, S. Harper¹³⁰, M.-L. Holmberg^{130,ffff}, Sh. Jain¹³⁰,
 J. Linacre¹³⁰, K. Manolopoulos¹³⁰, D. M. Newbold¹³⁰, E. Olaiya¹³⁰, D. Petyt¹³⁰, T. Reis¹³⁰, G. Salvi¹³⁰, T. Schuh¹³⁰,
 C. H. Shepherd-Themistocleous¹³⁰, I. R. Tomalin¹³⁰, T. Williams¹³⁰, R. Bainbridge¹³¹, P. Bloch¹³¹,
 S. Bonomally¹³¹, J. Borg¹³¹, C. E. Brown¹³¹, O. Buchmuller¹³¹, V. Cacchio¹³¹, C. A. Carrillo Montoya¹³¹,
 V. Cepaitis¹³¹, G. S. Chahal^{131,gggg}, D. Colling¹³¹, J. S. Dancu¹³¹, P. Dauncey¹³¹, G. Davies¹³¹, J. Davies¹³¹,
 M. Della Negra¹³¹, S. Fayer¹³¹, G. Fedi¹³¹, G. Hall¹³¹, M. H. Hassanshahi¹³¹, A. Howard¹³¹, G. Iles¹³¹,
 J. Langford¹³¹, L. Lyons¹³¹, A.-M. Magnan¹³¹, S. Malik¹³¹, A. Martelli¹³¹, M. Mieskolainen¹³¹, D. G. Monk¹³¹,
 J. Nash^{131,hhhh}, M. Pesaresi¹³¹, B. C. Radburn-Smith¹³¹, D. M. Raymond¹³¹, A. Richards¹³¹, A. Rose¹³¹, E. Scott¹³¹,
 C. Seez¹³¹, R. Shukla¹³¹, A. Tapper¹³¹, K. Uchida¹³¹, G. P. Uttley¹³¹, L. H. Vage¹³¹, T. Virdee^{131,aa},
 M. Vojinovic¹³¹, N. Wardle¹³¹, S. N. Webb¹³¹, D. Winterbottom¹³¹, K. Coldham¹³², J. E. Cole¹³², A. Khan¹³²,
 P. Kyberd¹³², I. D. Reid¹³², S. Abdullin¹³³, A. Brinkerhoff¹³³, B. Caraway¹³³, J. Dittmann¹³³, K. Hatakeyama¹³³,
 A. R. Kanuganti¹³³, B. McMaster¹³³, M. Saunders¹³³, S. Sawant¹³³, C. Sutantawibul¹³³, M. Toms¹³³,
 J. Wilson¹³³, R. Bartek¹³⁴, A. Dominguez¹³⁴, C. Huerta Escamilla¹³⁴, R. Uniyal¹³⁴, A. M. Vargas Hernandez¹³⁴,
 R. Chudasama¹³⁵, S. I. Cooper¹³⁵, D. Di Croce¹³⁵, S. V. Gleyzer¹³⁵, C. Henderson¹³⁵, C. U. Perez¹³⁵,
 P. Rumerio^{135,iii}, E. Usai¹³⁵, C. West¹³⁵, A. Akpinar¹³⁶, A. Albert¹³⁶, D. Arcaro¹³⁶, C. Cosby¹³⁶,
 Z. Demiragli¹³⁶, C. Erice¹³⁶, E. Fontanesi¹³⁶, D. Gastler¹³⁶, S. May¹³⁶, J. Rohlf¹³⁶, K. Salyer¹³⁶, D. Sperka¹³⁶,
 D. Spitzbart¹³⁶, I. Suarez¹³⁶, A. Tsatsos¹³⁶, S. Yuan¹³⁶, G. Benelli¹³⁷, X. Coubez^{137,v}, D. Cutts¹³⁷, M. Hadley¹³⁷,
 U. Heintz¹³⁷, J. M. Hogan^{137,jjjj}, T. Kwon¹³⁷, G. Landsberg¹³⁷, K. T. Lau¹³⁷, D. Li¹³⁷, J. Luo¹³⁷, M. Narain¹³⁷,
 N. Pervan¹³⁷, S. Sagir^{137,kkkk}, F. Simpson¹³⁷, W. Y. Wong¹³⁷, X. Yan¹³⁷, D. Yu¹³⁷, W. Zhang¹³⁷, S. Abbott¹³⁸,
 J. Bonilla¹³⁸, C. Brainerd¹³⁸, R. Breedon¹³⁸, M. Calderon De La Barca Sanchez¹³⁸, M. Chertok¹³⁸, J. Conway¹³⁸,
 P. T. Cox¹³⁸, R. Erbacher¹³⁸, G. Haza¹³⁸, F. Jensen¹³⁸, O. Kukral¹³⁸, G. Mocellin¹³⁸, M. Mulhearn¹³⁸,
 D. Pellett¹³⁸, B. Regnery¹³⁸, Y. Yao¹³⁸, F. Zhang¹³⁸, M. Bachtis¹³⁹, R. Cousins¹³⁹, A. Datta¹³⁹, J. Hauser¹³⁹,
 M. Ignatenko¹³⁹, M. A. Iqbal¹³⁹, T. Lam¹³⁹, E. Manca¹³⁹, W. A. Nash¹³⁹, D. Saltzberg¹³⁹, B. Stone¹³⁹,
 V. Valuev¹³⁹, R. Clare¹⁴⁰, J. W. Gary¹⁴⁰, M. Gordon¹⁴⁰, G. Hanson¹⁴⁰, O. R. Long¹⁴⁰, N. Manganeli¹⁴⁰,
 W. Si¹⁴⁰, S. Wimpenny¹⁴⁰, J. G. Branson¹⁴¹, S. Cittolin¹⁴¹, S. Cooperstein¹⁴¹, D. Diaz¹⁴¹, J. Duarte¹⁴¹,
 R. Gerosa¹⁴¹, L. Giannini¹⁴¹, J. Guiang¹⁴¹, R. Kansal¹⁴¹, V. Krutelyov¹⁴¹, R. Lee¹⁴¹, J. Letts¹⁴¹,
 M. Masciovecchio¹⁴¹, F. Mokhtar¹⁴¹, M. Pieri¹⁴¹, M. Quinnan¹⁴¹, B. V. Sathia Narayanan¹⁴¹, V. Sharma¹⁴¹,
 M. Tadel¹⁴¹, E. Vourliotis¹⁴¹, F. Würthwein¹⁴¹, Y. Xiang¹⁴¹, A. Yagil¹⁴¹, N. Amin¹⁴², C. Campagnari¹⁴²,
 M. Citron¹⁴², G. Collura¹⁴², A. Dorsett¹⁴², J. Incandela¹⁴², M. Kilpatrick¹⁴², J. Kim¹⁴², A. J. Li¹⁴²,
 P. Masterson¹⁴², H. Mei¹⁴², M. Oshiro¹⁴², J. Richman¹⁴², U. Sarica¹⁴², R. Schmitz¹⁴², F. Setti¹⁴²,
 J. Sheplock¹⁴², P. Siddireddy¹⁴², D. Stuart¹⁴², S. Wang¹⁴², A. Bornheim¹⁴³, O. Cerri¹⁴³, I. Dutta¹⁴³, A. Latorre¹⁴³,
 J. M. Lawhorn¹⁴³, J. Mao¹⁴³, H. B. Newman¹⁴³, T. Q. Nguyen¹⁴³, M. Spiropulu¹⁴³, J. R. Vlimant¹⁴³,
 C. Wang¹⁴³, S. Xie¹⁴³, R. Y. Zhu¹⁴³, J. Alison¹⁴⁴, S. An¹⁴⁴, M. B. Andrews¹⁴⁴, P. Bryant¹⁴⁴, V. Dutta¹⁴⁴,
 T. Ferguson¹⁴⁴, A. Harilal¹⁴⁴, C. Liu¹⁴⁴, T. Mudholkar¹⁴⁴, S. Murthy¹⁴⁴, M. Paulini¹⁴⁴, A. Roberts¹⁴⁴,
 A. Sanchez¹⁴⁴, W. Terrill¹⁴⁴, J. P. Cumalat¹⁴⁵, W. T. Ford¹⁴⁵, A. Hassani¹⁴⁵, G. Karathanasis¹⁴⁵, E. MacDonald¹⁴⁵,
 F. Marini¹⁴⁵, A. Perloff¹⁴⁵, C. Savard¹⁴⁵, N. Schonbeck¹⁴⁵, K. Stenson¹⁴⁵, K. A. Ulmer¹⁴⁵, S. R. Wagner¹⁴⁵,
 N. Zipper¹⁴⁵, J. Alexander¹⁴⁶, S. Bright-Thonney¹⁴⁶, X. Chen¹⁴⁶, D. J. Cranshaw¹⁴⁶, J. Fan¹⁴⁶, X. Fan¹⁴⁶,
 D. Gadkari¹⁴⁶, S. Hogan¹⁴⁶, J. Monroy¹⁴⁶, J. R. Patterson¹⁴⁶, J. Reichert¹⁴⁶, M. Reid¹⁴⁶, A. Ryd¹⁴⁶, J. Thom¹⁴⁶,
 P. Wittich¹⁴⁶, R. Zou¹⁴⁶, M. Albrow¹⁴⁷, M. Alyari¹⁴⁷, G. Apollinari¹⁴⁷, A. Apresyan¹⁴⁷, L. A. T. Bauerdick¹⁴⁷,
 D. Berry¹⁴⁷, J. Berryhill¹⁴⁷, P. C. Bhat¹⁴⁷, K. Burkett¹⁴⁷, J. N. Butler¹⁴⁷, A. Canepa¹⁴⁷, G. B. Cerati¹⁴⁷,
 H. W. K. Cheung¹⁴⁷, F. Chlebana¹⁴⁷, K. F. Di Petrillo¹⁴⁷, J. Dickinson¹⁴⁷, V. D. Elvira¹⁴⁷, Y. Feng¹⁴⁷,
 J. Freeman¹⁴⁷, A. Gandrakota¹⁴⁷, Z. Gece¹⁴⁷, L. Gray¹⁴⁷, D. Green¹⁴⁷, S. Grünendahl¹⁴⁷, D. Guerrero¹⁴⁷,
 O. Gutsche¹⁴⁷, R. M. Harris¹⁴⁷, R. Heller¹⁴⁷, T. C. Herwig¹⁴⁷, J. Hirschauer¹⁴⁷, L. Horyn¹⁴⁷, B. Jayatilaka¹⁴⁷,
 S. Jindariani¹⁴⁷, M. Johnson¹⁴⁷, U. Joshi¹⁴⁷, T. Klijsma¹⁴⁷, B. Klima¹⁴⁷, K. H. M. Kwok¹⁴⁷, S. Lammel¹⁴⁷,
 D. Lincoln¹⁴⁷, R. Lipton¹⁴⁷, T. Liu¹⁴⁷, C. Madrid¹⁴⁷, K. Maeshima¹⁴⁷, C. Mantilla¹⁴⁷, D. Mason¹⁴⁷,
 P. McBride¹⁴⁷, P. Merkel¹⁴⁷, S. Mrenna¹⁴⁷, S. Nahn¹⁴⁷, J. Ngadiuba¹⁴⁷, D. Noonan¹⁴⁷, S. Norberg¹⁴⁷,
 V. Papadimitriou¹⁴⁷, N. Pastika¹⁴⁷, K. Pedro¹⁴⁷, C. Pena¹⁴⁷, F. Ravera¹⁴⁷, A. Reinsvold Hall^{147,mmmm},
 L. Ristori¹⁴⁷, E. Sexton-Kennedy¹⁴⁷, N. Smith¹⁴⁷, A. Soha¹⁴⁷, L. Spiegel¹⁴⁷, J. Strait¹⁴⁷, L. Taylor¹⁴⁷,
 S. Tkaczyk¹⁴⁷, N. V. Tran¹⁴⁷, L. Uplegger¹⁴⁷, E. W. Vaandering¹⁴⁷, I. Zoi¹⁴⁷, P. Avery¹⁴⁸, D. Bourilkov¹⁴⁸

- L. Cadamuro¹⁴⁸, P. Chang¹⁴⁸, V. Cherepanov¹⁴⁸, R. D. Field¹⁴⁸, E. Koenig¹⁴⁸, M. Kolosova¹⁴⁸, J. Konigsberg¹⁴⁸, A. Korytov¹⁴⁸, E. Kuznetsova^{148,nnnn}, K. H. Lo¹⁴⁸, K. Matchev¹⁴⁸, N. Menendez¹⁴⁸, G. Mitselmakher¹⁴⁸, A. Muthirakalayil Madhu¹⁴⁸, N. Rawal¹⁴⁸, D. Rosenzweig¹⁴⁸, S. Rosenzweig¹⁴⁸, K. Shi¹⁴⁸, J. Wang¹⁴⁸, Z. Wu¹⁴⁸, T. Adams¹⁴⁹, A. Askew¹⁴⁹, N. Bower¹⁴⁹, R. Habibullah¹⁴⁹, V. Hagopian¹⁴⁹, T. Kolberg¹⁴⁹, G. Martinez¹⁴⁹, H. Prosper¹⁴⁹, O. Viazlo¹⁴⁹, M. Wulansatiti¹⁴⁹, R. Yohay¹⁴⁹, J. Zhang¹⁴⁹, M. M. Baarmand¹⁵⁰, S. Butalla¹⁵⁰, T. Elkafrawy^{150,bbb}, M. Hohmann¹⁵⁰, R. Kumar Verma¹⁵⁰, M. Rahmani¹⁵⁰, F. Yumiceva¹⁵⁰, M. R. Adams¹⁵¹, R. Cavanaugh¹⁵¹, S. Dittmer¹⁵¹, O. Evdokimov¹⁵¹, C. E. Gerber¹⁵¹, D. J. Hofman¹⁵¹, D. S. Lemos¹⁵¹, A. H. Merrit¹⁵¹, C. Mills¹⁵¹, G. Oh¹⁵¹, T. Roy¹⁵¹, S. Rudrabhatla¹⁵¹, M. B. Tonjes¹⁵¹, N. Varelas¹⁵¹, X. Wang¹⁵¹, Z. Ye¹⁵¹, J. Yoo¹⁵¹, M. Alhuseini¹⁵², K. Dilsiz^{152,oooo}, L. Emediato¹⁵², G. Karaman¹⁵², O. K. Köseyan¹⁵², J.-P. Merlo¹⁵², A. Mestvirishvili^{152,pppp}, J. Nachtman¹⁵², O. Neogi¹⁵², H. Ogul^{152,qqqq}, Y. Onel¹⁵², A. Penzo¹⁵², C. Snyder¹⁵², E. Tiras^{152,rrrr}, O. Amram¹⁵³, B. Blumenfeld¹⁵³, L. Corcodilos¹⁵³, J. Davis¹⁵³, A. V. Gritsan¹⁵³, S. Kyriacou¹⁵³, P. Maksimovic¹⁵³, J. Roskes¹⁵³, S. Sekhar¹⁵³, M. Swartz¹⁵³, T. Á. Vámi¹⁵³, A. Abreu¹⁵⁴, L. F. Alcerro Alcerro¹⁵⁴, J. Anguiano¹⁵⁴, P. Baringer¹⁵⁴, A. Bean¹⁵⁴, Z. Flowers¹⁵⁴, J. King¹⁵⁴, G. Krintiras¹⁵⁴, M. Lazarovits¹⁵⁴, C. Le Mahieu¹⁵⁴, C. Lindsey¹⁵⁴, J. Marquez¹⁵⁴, N. Minafra¹⁵⁴, M. Murray¹⁵⁴, M. Nickel¹⁵⁴, C. Rogan¹⁵⁴, C. Royon¹⁵⁴, R. Salvatico¹⁵⁴, S. Sanders¹⁵⁴, C. Smith¹⁵⁴, Q. Wang¹⁵⁴, G. Wilson¹⁵⁴, B. Allmond¹⁵⁵, S. Duric¹⁵⁵, A. Ivanov¹⁵⁵, K. Kaadze¹⁵⁵, A. Kalogeropoulos¹⁵⁵, D. Kim¹⁵⁵, Y. Maravin¹⁵⁵, T. Mitchell¹⁵⁵, A. Modak¹⁵⁵, K. Nam¹⁵⁵, D. Roy¹⁵⁵, F. Rebassoo¹⁵⁶, D. Wright¹⁵⁶, E. Adams¹⁵⁷, A. Baden¹⁵⁷, O. Baron¹⁵⁷, A. Belloni¹⁵⁷, A. Bethani¹⁵⁷, S. C. Eno¹⁵⁷, N. J. Hadley¹⁵⁷, S. Jabeen¹⁵⁷, R. G. Kellogg¹⁵⁷, T. Koeth¹⁵⁷, Y. Lai¹⁵⁷, S. Lascio¹⁵⁷, A. C. Mignerey¹⁵⁷, S. Nabili¹⁵⁷, C. Palmer¹⁵⁷, C. Papageorgakis¹⁵⁷, L. Wang¹⁵⁷, K. Wong¹⁵⁷, W. Busza¹⁵⁸, I. A. Cali¹⁵⁸, Y. Chen¹⁵⁸, M. D'Alfonso¹⁵⁸, J. Eysermans¹⁵⁸, C. Freer¹⁵⁸, G. Gomez-Ceballos¹⁵⁸, M. Goncharov¹⁵⁸, P. Harris¹⁵⁸, M. Hu¹⁵⁸, D. Kovalskyi¹⁵⁸, J. Krupa¹⁵⁸, Y.-J. Lee¹⁵⁸, K. Long¹⁵⁸, C. Mironov¹⁵⁸, C. Paus¹⁵⁸, D. Rankin¹⁵⁸, C. Roland¹⁵⁸, G. Roland¹⁵⁸, Z. Shi¹⁵⁸, G. S. F. Stephans¹⁵⁸, J. Wang¹⁵⁸, Z. Wang¹⁵⁸, B. Wyslouch¹⁵⁸, T. J. Yang¹⁵⁸, R. M. Chatterjee¹⁵⁹, B. Crossman¹⁵⁹, J. Hiltbrand¹⁵⁹, B. M. Joshi¹⁵⁹, C. Kapsiak¹⁵⁹, M. Krohn¹⁵⁹, Y. Kubota¹⁵⁹, D. Mahon¹⁵⁹, J. Mans¹⁵⁹, M. Revering¹⁵⁹, R. Rusack¹⁵⁹, R. Saradhy¹⁵⁹, N. Schroeder¹⁵⁹, N. Strobbe¹⁵⁹, M. A. Wadud¹⁵⁹, L. M. Cremaldi¹⁶⁰, K. Bloom¹⁶¹, M. Bryson¹⁶¹, D. R. Claes¹⁶¹, C. Fangmeier¹⁶¹, L. Finco¹⁶¹, F. Golf¹⁶¹, C. Joo¹⁶¹, R. Kamalieddin¹⁶¹, I. Kravchenko¹⁶¹, I. Reed¹⁶¹, J. E. Siado¹⁶¹, G. R. Snow^{161,a}, W. Tabb¹⁶¹, A. Wightman¹⁶¹, F. Yan¹⁶¹, A. G. Zecchinelli¹⁶¹, G. Agarwal¹⁶², H. Bandyopadhyay¹⁶², L. Hay¹⁶², I. Iashvili¹⁶², A. Kharchilava¹⁶², C. McLean¹⁶², M. Morris¹⁶², D. Nguyen¹⁶², J. Pekkanen¹⁶², S. Rappoccio¹⁶², A. Williams¹⁶², G. Alverson¹⁶³, E. Barberis¹⁶³, Y. Haddad¹⁶³, Y. Han¹⁶³, A. Krishna¹⁶³, J. Li¹⁶³, J. Lidrych¹⁶³, G. Madigan¹⁶³, B. Marzocchi¹⁶³, D. M. Morse¹⁶³, V. Nguyen¹⁶³, T. Orimoto¹⁶³, A. Parker¹⁶³, L. Skinnari¹⁶³, A. Tishelman-Charny¹⁶³, T. Wamorkar¹⁶³, B. Wang¹⁶³, A. Wisecarver¹⁶³, D. Wood¹⁶³, S. Bhattacharya¹⁶⁴, J. Bueghly¹⁶⁴, Z. Chen¹⁶⁴, A. Gilbert¹⁶⁴, K. A. Hahn¹⁶⁴, Y. Liu¹⁶⁴, N. Odell¹⁶⁴, M. H. Schmitt¹⁶⁴, M. Velasco¹⁶⁴, R. Band¹⁶⁵, R. Bucci¹⁶⁵, M. Cremonesi¹⁶⁵, A. Das¹⁶⁵, R. Goldouzian¹⁶⁵, M. Hildreth¹⁶⁵, K. Hurtado Anampa¹⁶⁵, C. Jessop¹⁶⁵, K. Lannon¹⁶⁵, J. Lawrence¹⁶⁵, N. Loukas¹⁶⁵, L. Lutton¹⁶⁵, J. Mariano¹⁶⁵, N. Marinelli¹⁶⁵, I. Mcalister¹⁶⁵, T. McCauley¹⁶⁵, C. Mcgrady¹⁶⁵, K. Mohrman¹⁶⁵, C. Moore¹⁶⁵, Y. Musienko^{165,m}, R. Ruchti¹⁶⁵, A. Townsend¹⁶⁵, M. Wayne¹⁶⁵, H. Yockey¹⁶⁵, M. Zarucki¹⁶⁵, L. Zygala¹⁶⁵, B. Bylsma¹⁶⁶, M. Carrigan¹⁶⁶, L. S. Durkin¹⁶⁶, C. Hill¹⁶⁶, M. Joyce¹⁶⁶, A. Lesauvage¹⁶⁶, M. Nunez Ornelas¹⁶⁶, K. Wei¹⁶⁶, B. L. Winer¹⁶⁶, B. R. Yates¹⁶⁶, F. M. Addesa¹⁶⁷, P. Das¹⁶⁷, G. Dezoort¹⁶⁷, P. Elmer¹⁶⁷, A. Frankenthal¹⁶⁷, B. Greenberg¹⁶⁷, N. Haubrich¹⁶⁷, S. Higginbotham¹⁶⁷, G. Kopp¹⁶⁷, S. Kwan¹⁶⁷, D. Lange¹⁶⁷, A. Loeliger¹⁶⁷, D. Marlow¹⁶⁷, I. Ojalvo¹⁶⁷, J. Olsen¹⁶⁷, D. Stickland¹⁶⁷, C. Tully¹⁶⁷, S. Malik¹⁶⁸, A. S. Bakshi¹⁶⁹, V. E. Barnes¹⁶⁹, R. Chawla¹⁶⁹, S. Das¹⁶⁹, L. Gutay¹⁶⁹, M. Jones¹⁶⁹, A. W. Jung¹⁶⁹, D. Kondratyev¹⁶⁹, A. M. Koshy¹⁶⁹, M. Liu¹⁶⁹, G. Negro¹⁶⁹, N. Neumeister¹⁶⁹, G. Paspalaki¹⁶⁹, S. Piperov¹⁶⁹, A. Purohit¹⁶⁹, J. F. Schulte¹⁶⁹, M. Stojanovic¹⁶⁹, J. Thieman¹⁶⁹, A. K. Viridi¹⁶⁹, F. Wang¹⁶⁹, R. Xiao¹⁶⁹, W. Xie¹⁶⁹, J. Dolen¹⁷⁰, N. Parashar¹⁷⁰, D. Acosta¹⁷¹, A. Baty¹⁷¹, T. Carnahan¹⁷¹, S. Dildick¹⁷¹, K. M. Ecklund¹⁷¹, P. J. Fernández Manteca¹⁷¹, S. Freed¹⁷¹, P. Gardner¹⁷¹, F. J. M. Geurts¹⁷¹, A. Kumar¹⁷¹, W. Li¹⁷¹, B. P. Padley¹⁷¹, R. Redjimi¹⁷¹, J. Rotter¹⁷¹, S. Yang¹⁷¹, E. Yigitbasi¹⁷¹, Y. Zhang¹⁷¹, A. Bodek¹⁷², P. de Barbaro¹⁷², R. Demina¹⁷², J. L. Dulemba¹⁷², C. Fallon¹⁷², A. Garcia-Bellido¹⁷², O. Hindrichs¹⁷², A. Khukhunaishvili¹⁷², P. Parygin¹⁷², E. Popova¹⁷², R. Taus¹⁷², G. P. Van Onsem¹⁷², K. Goulios¹⁷³, B. Chiarito¹⁷⁴, J. P. Chou¹⁷⁴, Y. Gershtein¹⁷⁴, E. Halkiadakis¹⁷⁴, A. Hart¹⁷⁴, M. Heindl¹⁷⁴

D. Jaroslowski¹⁷⁴, O. Karacheban^{174,y}, I. Laflotte¹⁷⁴, A. Lath¹⁷⁴, R. Montalvo¹⁷⁴, K. Nash¹⁷⁴, M. Osherson¹⁷⁴,
H. Routray¹⁷⁴, S. Salur¹⁷⁴, S. Schnetzer¹⁷⁴, S. Somalwar¹⁷⁴, R. Stone¹⁷⁴, S. A. Thayil¹⁷⁴, S. Thomas¹⁷⁴,
H. Wang¹⁷⁴, H. Acharya¹⁷⁵, A. G. Delannoy¹⁷⁵, S. Fiorendi¹⁷⁵, T. Holmes¹⁷⁵, E. Nibigira¹⁷⁵, S. Spanier¹⁷⁵,
O. Bouhali^{176,ssss}, M. Dalchenko¹⁷⁶, A. Delgado¹⁷⁶, R. Eusebi¹⁷⁶, J. Gilmore¹⁷⁶, T. Huang¹⁷⁶, T. Kamon^{176,ttt},
H. Kim¹⁷⁶, S. Luo¹⁷⁶, S. Malhotra¹⁷⁶, R. Mueller¹⁷⁶, D. Overton¹⁷⁶, D. Rathjens¹⁷⁶, A. Safonov¹⁷⁶,
N. Akchurin¹⁷⁷, J. Damgov¹⁷⁷, V. Hegde¹⁷⁷, K. Lamichhane¹⁷⁷, S. W. Lee¹⁷⁷, T. Mengke¹⁷⁷, S. Muthumuni¹⁷⁷,
T. Peltola¹⁷⁷, I. Volobouev¹⁷⁷, A. Whitbeck¹⁷⁷, E. Appelt¹⁷⁸, S. Greene¹⁷⁸, A. Gurrola¹⁷⁸, W. Johns¹⁷⁸,
A. Melo¹⁷⁸, F. Romeo¹⁷⁸, P. Sheldon¹⁷⁸, S. Tuo¹⁷⁸, J. Velkovska¹⁷⁸, J. Viinikainen¹⁷⁸, B. Cardwell¹⁷⁹,
B. Cox¹⁷⁹, G. Cummings¹⁷⁹, J. Hakala¹⁷⁹, R. Hirosky¹⁷⁹, A. Ledovskoy¹⁷⁹, A. Li¹⁷⁹, C. Neu¹⁷⁹,
C. E. Perez Lara¹⁷⁹, P. E. Karchin¹⁸⁰, A. Aravind¹⁸¹, S. Banerjee¹⁸¹, K. Black¹⁸¹, T. Bose¹⁸¹, S. Dasu¹⁸¹,
I. De Bruyn¹⁸¹, P. Everaerts¹⁸¹, C. Galloni¹⁸¹, H. He¹⁸¹, M. Herndon¹⁸¹, A. Herve¹⁸¹, C. K. Koraka¹⁸¹,
A. Lanaro¹⁸¹, R. Loveless¹⁸¹, J. Madhusudanan Sreekala¹⁸¹, A. Mallampalli¹⁸¹, A. Mohammadi¹⁸¹, S. Mondal¹⁸¹,
G. Parida¹⁸¹, D. Pinna¹⁸¹, A. Savin¹⁸¹, V. Shang¹⁸¹, V. Sharma¹⁸¹, W. H. Smith¹⁸¹, D. Teague¹⁸¹, H. F. Tsoi¹⁸¹,
W. Vetens¹⁸¹, A. Warden¹⁸¹, S. Afanasiev¹⁸², V. Andreev¹⁸², Yu. Andreev¹⁸², T. Aushev¹⁸², M. Azarkin¹⁸²,
A. Babaev¹⁸², A. Belyaev¹⁸², V. Blinov^{182,m}, E. Boos¹⁸², V. Borshch¹⁸², D. Budkouski¹⁸², V. Bunichev¹⁸²,
V. Chekhovskiy¹⁸², R. Chistov^{182,m}, M. Danilov^{182,m}, A. Dermenev¹⁸², T. Dimova^{182,m}, I. Dremin¹⁸²,
M. Dubinin^{182,llll}, L. Dudko¹⁸², V. Epshteyn¹⁸², G. Gavrilo¹⁸², V. Gavrilo¹⁸², S. Gninenko¹⁸²,
V. Golovtsov¹⁸², N. Golubev¹⁸², I. Golutvin¹⁸², I. Gorbunov¹⁸², A. Gribushin¹⁸², Y. Ivanov¹⁸², V. Kachanov¹⁸²,
L. Kardapoltsev^{182,m}, V. Karjavine¹⁸², A. Karneyev¹⁸², V. Kim^{182,m}, M. Kirakosyan¹⁸², D. Kirpichnikov¹⁸²,
M. Kirsanov¹⁸², V. Klyukhin¹⁸², O. Kodolova^{182,uuuu}, D. Konstantinov¹⁸², V. Korenkov¹⁸², A. Kozyrev^{182,m},
N. Krasnikov¹⁸², A. Lanev¹⁸², P. Levchenko¹⁸², A. Litomin¹⁸², N. Lychkovskaya¹⁸², V. Makarenko¹⁸²,
A. Malakhov¹⁸², V. Matveev^{182,m,m}, V. Murzin¹⁸², A. Nikitenko^{182,vvvv,uuuu}, S. Obraztsov¹⁸², A. Oskin¹⁸²,
I. Ovtin^{182,m}, V. Palichik¹⁸², V. Perelygin¹⁸², M. Perfilov¹⁸², S. Petrushanko¹⁸², S. Polikarpov^{182,m}, V. Popov¹⁸²,
O. Radchenko^{182,m}, M. Savina¹⁸², V. Savrin¹⁸², V. Shalae¹⁸², S. Shmatov¹⁸², S. Shulha¹⁸², Y. Skovpen^{182,m},
S. Slabospitskii¹⁸², V. Smirnov¹⁸², D. Sosnov¹⁸², V. Sulimov¹⁸², E. Tcherniaev¹⁸², A. Terkulov¹⁸²,
O. Teryaev¹⁸², I. Tlisova¹⁸², A. Toropin¹⁸², L. Uvarov¹⁸², A. Uzunian¹⁸², A. Vorobyev^{182,a}, N. Voytishin¹⁸²,
B. S. Yuldashev^{182,wwww}, A. Zarubin¹⁸², I. Zhizhin¹⁸² and A. Zhokin¹⁸²

(CMS Collaboration)

¹Yerevan Physics Institute, Yerevan, Armenia²Institut für Hochenergiephysik, Vienna, Austria³Universiteit Antwerpen, Antwerpen, Belgium⁴Vrije Universiteit Brussel, Brussel, Belgium⁵Université Libre de Bruxelles, Bruxelles, Belgium⁶Ghent University, Ghent, Belgium⁷Université Catholique de Louvain, Louvain-la-Neuve, Belgium⁸Centro Brasileiro de Pesquisas Físicas, Rio de Janeiro, Brazil⁹Universidade do Estado do Rio de Janeiro, Rio de Janeiro, Brazil¹⁰Universidade Estadual Paulista, Universidade Federal do ABC, São Paulo, Brazil¹¹Institute for Nuclear Research and Nuclear Energy, Bulgarian Academy of Sciences, Sofia, Bulgaria¹²University of Sofia, Sofia, Bulgaria¹³Instituto De Alta Investigación, Universidad de Tarapacá, Casilla 7 D, Arica, Chile¹⁴Beihang University, Beijing, China¹⁵Department of Physics, Tsinghua University, Beijing, China¹⁶Institute of High Energy Physics, Beijing, China¹⁷State Key Laboratory of Nuclear Physics and Technology, Peking University, Beijing, China¹⁸Sun Yat-Sen University, Guangzhou, China¹⁹University of Science and Technology of China, Hefei, China²⁰Institute of Modern Physics and Key Laboratory of Nuclear Physics and Ion-beam Application (MOE)—Fudan University, Shanghai, China²¹Zhejiang University, Hangzhou, Zhejiang, China²²Universidad de Los Andes, Bogota, Colombia

- ²³*Universidad de Antioquia, Medellin, Colombia*
- ²⁴*University of Split, Faculty of Electrical Engineering, Mechanical Engineering and Naval Architecture, Split, Croatia*
- ²⁵*University of Split, Faculty of Science, Split, Croatia*
- ²⁶*Institute Rudjer Boskovic, Zagreb, Croatia*
- ²⁷*University of Cyprus, Nicosia, Cyprus*
- ²⁸*Charles University, Prague, Czech Republic*
- ²⁹*Escuela Politecnica Nacional, Quito, Ecuador*
- ³⁰*Universidad San Francisco de Quito, Quito, Ecuador*
- ³¹*Academy of Scientific Research and Technology of the Arab Republic of Egypt, Egyptian Network of High Energy Physics, Cairo, Egypt*
- ³²*Center for High Energy Physics (CHEP-FU), Fayoum University, El-Fayoum, Egypt*
- ³³*National Institute of Chemical Physics and Biophysics, Tallinn, Estonia*
- ³⁴*Department of Physics, University of Helsinki, Helsinki, Finland*
- ³⁵*Helsinki Institute of Physics, Helsinki, Finland*
- ³⁶*Lappeenranta-Lahti University of Technology, Lappeenranta, Finland*
- ³⁷*IRFU, CEA, Université Paris-Saclay, Gif-sur-Yvette, France*
- ³⁸*Laboratoire Leprince-Ringuet, CNRS/IN2P3, Ecole Polytechnique, Institut Polytechnique de Paris, Palaiseau, France*
- ³⁹*Université de Strasbourg, CNRS, IPHC UMR 7178, Strasbourg, France*
- ⁴⁰*Institut de Physique des 2 Infinis de Lyon (IP2I), Villeurbanne, France*
- ⁴¹*Georgian Technical University, Tbilisi, Georgia*
- ⁴²*RWTH Aachen University, I. Physikalisches Institut, Aachen, Germany*
- ⁴³*RWTH Aachen University, III. Physikalisches Institut A, Aachen, Germany*
- ⁴⁴*RWTH Aachen University, III. Physikalisches Institut B, Aachen, Germany*
- ⁴⁵*Deutsches Elektronen-Synchrotron, Hamburg, Germany*
- ⁴⁶*University of Hamburg, Hamburg, Germany*
- ⁴⁷*Karlsruher Institut fuer Technologie, Karlsruhe, Germany*
- ⁴⁸*Institute of Nuclear and Particle Physics (INPP), NCSR Demokritos, Aghia Paraskevi, Greece*
- ⁴⁹*National and Kapodistrian University of Athens, Athens, Greece*
- ⁵⁰*National Technical University of Athens, Athens, Greece*
- ⁵¹*University of Ioánnina, Ioánnina, Greece*
- ⁵²*HUN-REN Wigner Research Centre for Physics, Budapest, Hungary*
- ⁵³*MTA-ELTE Lendület CMS Particle and Nuclear Physics Group, Eötvös Loránd University, Budapest, Hungary*
- ⁵⁴*Institute of Nuclear Research ATOMKI, Debrecen, Hungary*
- ⁵⁵*Institute of Physics, University of Debrecen, Debrecen, Hungary*
- ⁵⁶*Karoly Robert Campus, MATE Institute of Technology, Gyongyos, Hungary*
- ⁵⁷*Panjab University, Chandigarh, India*
- ⁵⁸*University of Delhi, Delhi, India*
- ⁵⁹*Saha Institute of Nuclear Physics, HBNI, Kolkata, India*
- ⁶⁰*Indian Institute of Technology Madras, Madras, India*
- ⁶¹*Bhabha Atomic Research Centre, Mumbai, India*
- ⁶²*Tata Institute of Fundamental Research-A, Mumbai, India*
- ⁶³*Tata Institute of Fundamental Research-B, Mumbai, India*
- ⁶⁴*National Institute of Science Education and Research, An OCC of Homi Bhabha National Institute, Bhubaneswar, Odisha, India*
- ⁶⁵*Indian Institute of Science Education and Research (IISER), Pune, India*
- ⁶⁶*Isfahan University of Technology, Isfahan, Iran*
- ⁶⁷*Institute for Research in Fundamental Sciences (IPM), Tehran, Iran*
- ⁶⁸*University College Dublin, Dublin, Ireland*
- ^{69a}*INFN Sezione di Bari, Bari, Italy*
- ^{69b}*Università di Bari, Bari, Italy*
- ^{69c}*Politecnico di Bari, Bari, Italy*
- ^{70a}*INFN Sezione di Bologna, Bologna, Italy*
- ^{70b}*Università di Bologna, Bologna, Italy*
- ^{71a}*INFN Sezione di Catania, Catania, Italy*
- ^{71b}*Università di Catania, Catania, Italy*
- ^{72a}*INFN Sezione di Firenze, Firenze, Italy*
- ^{72b}*Università di Firenze, Firenze, Italy*

- ⁷³*INFN Laboratori Nazionali di Frascati, Frascati, Italy*
^{74a}*INFN Sezione di Genova, Genova, Italy*
^{74b}*Università di Genova, Genova, Italy*
^{75a}*INFN Sezione di Milano-Bicocca, Milano, Italy*
^{75b}*Università di Milano-Bicocca, Milano, Italy*
^{76a}*INFN Sezione di Napoli, Napoli, Italy*
^{76b}*Università di Napoli 'Federico II', Napoli, Italy*
^{76c}*Università della Basilicata, Potenza, Italy*
^{76d}*Scuola Superiore Meridionale (SSM), Napoli, Italy*
^{77a}*INFN Sezione di Padova, Padova, Italy*
^{77b}*Università di Padova, Padova, Italy*
^{77c}*Università di Trento, Trento, Italy*
^{78a}*INFN Sezione di Pavia, Pavia, Italy*
^{78b}*Università di Pavia, Pavia, Italy*
^{79a}*INFN Sezione di Perugia, Perugia, Italy*
^{79b}*Università di Perugia, Perugia, Italy*
^{80a}*INFN Sezione di Pisa, Pisa, Italy*
^{80b}*Università di Pisa, Pisa, Italy*
^{80c}*Scuola Normale Superiore di Pisa, Pisa, Italy*
^{80d}*Università di Siena, Siena, Italy*
^{81a}*INFN Sezione di Roma, Roma, Italy*
^{81b}*Sapienza Università di Roma, Roma, Italy*
^{82a}*INFN Sezione di Torino, Torino, Italy*
^{82b}*Università di Torino, Torino, Italy*
^{82c}*Università del Piemonte Orientale, Novara, Italy*
^{83a}*INFN Sezione di Trieste, Trieste, Italy*
^{83b}*Università di Trieste, Trieste, Italy*
⁸⁴*Kyungpook National University, Daegu, Korea*
⁸⁵*Chonnam National University, Institute for Universe and Elementary Particles, Kwangju, Korea*
⁸⁶*Hanyang University, Seoul, Korea*
⁸⁷*Korea University, Seoul, Korea*
⁸⁸*Kyung Hee University, Department of Physics, Seoul, Korea*
⁸⁹*Sejong University, Seoul, Korea*
⁹⁰*Seoul National University, Seoul, Korea*
⁹¹*University of Seoul, Seoul, Korea*
⁹²*Yonsei University, Department of Physics, Seoul, Korea*
⁹³*Sungkyunkwan University, Suwon, Korea*
⁹⁴*College of Engineering and Technology, American University of the Middle East (AUM),
Dasman, Kuwait*
⁹⁵*Riga Technical University, Riga, Latvia*
⁹⁶*Vilnius University, Vilnius, Lithuania*
⁹⁷*National Centre for Particle Physics, Universiti Malaya, Kuala Lumpur, Malaysia*
⁹⁸*Universidad de Sonora (UNISON), Hermosillo, Mexico*
⁹⁹*Centro de Investigación y de Estudios Avanzados del IPN, Mexico City, Mexico*
¹⁰⁰*Universidad Iberoamericana, Mexico City, Mexico*
¹⁰¹*Benemerita Universidad Autónoma de Puebla, Puebla, Mexico*
¹⁰²*University of Montenegro, Podgorica, Montenegro*
¹⁰³*National Centre for Physics, Quaid-I-Azam University, Islamabad, Pakistan*
¹⁰⁴*AGH University of Krakow, Faculty of Computer Science, Electronics and Telecommunications,
Krakow, Poland*
¹⁰⁵*National Centre for Nuclear Research, Swierk, Poland*
¹⁰⁶*Institute of Experimental Physics, Faculty of Physics, University of Warsaw, Warsaw, Poland*
¹⁰⁷*Laboratório de Instrumentação e Física Experimental de Partículas, Lisboa, Portugal*
¹⁰⁸*VINCA Institute of Nuclear Sciences, University of Belgrade, Belgrade, Serbia*
¹⁰⁹*Centro de Investigaciones Energéticas Medioambientales y Tecnológicas (CIEMAT), Madrid, Spain*
¹¹⁰*Universidad Autónoma de Madrid, Madrid, Spain*
¹¹¹*Universidad de Oviedo, Instituto Universitario de Ciencias y Tecnologías Espaciales de Asturias
(ICTEA), Oviedo, Spain*
¹¹²*Instituto de Física de Cantabria (IFCA), CSIC-Universidad de Cantabria, Santander, Spain*
¹¹³*University of Colombo, Colombo, Sri Lanka*

- ¹¹⁴*University of Ruhuna, Department of Physics, Matara, Sri Lanka*
- ¹¹⁵*CERN, European Organization for Nuclear Research, Geneva, Switzerland*
- ¹¹⁶*Paul Scherrer Institut, Villigen, Switzerland*
- ¹¹⁷*ETH Zurich—Institute for Particle Physics and Astrophysics (IPA), Zurich, Switzerland*
- ¹¹⁸*Universität Zürich, Zurich, Switzerland*
- ¹¹⁹*National Central University, Chung-Li, Taiwan*
- ¹²⁰*National Taiwan University (NTU), Taipei, Taiwan*
- ¹²¹*High Energy Physics Research Unit, Department of Physics, Faculty of Science, Chulalongkorn University, Bangkok, Thailand*
- ¹²²*Çukurova University, Physics Department, Science and Art Faculty, Adana, Turkey*
- ¹²³*Middle East Technical University, Physics Department, Ankara, Turkey*
- ¹²⁴*Bogazici University, Istanbul, Turkey*
- ¹²⁵*Istanbul Technical University, Istanbul, Turkey*
- ¹²⁶*Istanbul University, Istanbul, Turkey*
- ¹²⁷*Institute for Scintillation Materials of National Academy of Science of Ukraine, Kharkiv, Ukraine*
- ¹²⁸*National Science Centre, Kharkiv Institute of Physics and Technology, Kharkiv, Ukraine*
- ¹²⁹*University of Bristol, Bristol, United Kingdom*
- ¹³⁰*Rutherford Appleton Laboratory, Didcot, United Kingdom*
- ¹³¹*Imperial College, London, United Kingdom*
- ¹³²*Brunel University, Uxbridge, United Kingdom*
- ¹³³*Baylor University, Waco, Texas, USA*
- ¹³⁴*Catholic University of America, Washington, DC, USA*
- ¹³⁵*The University of Alabama, Tuscaloosa, Alabama, USA*
- ¹³⁶*Boston University, Boston, Massachusetts, USA*
- ¹³⁷*Brown University, Providence, Rhode Island, USA*
- ¹³⁸*University of California, Davis, Davis, California, USA*
- ¹³⁹*University of California, Los Angeles, California, USA*
- ¹⁴⁰*University of California, Riverside, Riverside, California, USA*
- ¹⁴¹*University of California, San Diego, La Jolla, California, USA*
- ¹⁴²*University of California, Santa Barbara—Department of Physics, Santa Barbara, California, USA*
- ¹⁴³*California Institute of Technology, Pasadena, California, USA*
- ¹⁴⁴*Carnegie Mellon University, Pittsburgh, Pennsylvania, USA*
- ¹⁴⁵*University of Colorado Boulder, Boulder, Colorado, USA*
- ¹⁴⁶*Cornell University, Ithaca, New York, USA*
- ¹⁴⁷*Fermi National Accelerator Laboratory, Batavia, Illinois, USA*
- ¹⁴⁸*University of Florida, Gainesville, Florida, USA*
- ¹⁴⁹*Florida State University, Tallahassee, Florida, USA*
- ¹⁵⁰*Florida Institute of Technology, Melbourne, Florida, USA*
- ¹⁵¹*University of Illinois Chicago, Chicago, USA, Chicago, USA*
- ¹⁵²*The University of Iowa, Iowa City, Iowa, USA*
- ¹⁵³*Johns Hopkins University, Baltimore, Maryland, USA*
- ¹⁵⁴*The University of Kansas, Lawrence, Kansas, USA*
- ¹⁵⁵*Kansas State University, Manhattan, Kansas, USA*
- ¹⁵⁶*Lawrence Livermore National Laboratory, Livermore, California, USA*
- ¹⁵⁷*University of Maryland, College Park, Maryland, USA*
- ¹⁵⁸*Massachusetts Institute of Technology, Cambridge, Massachusetts, USA*
- ¹⁵⁹*University of Minnesota, Minneapolis, Minnesota, USA*
- ¹⁶⁰*University of Mississippi, Oxford, Mississippi, USA*
- ¹⁶¹*University of Nebraska-Lincoln, Lincoln, Nebraska, USA*
- ¹⁶²*State University of New York at Buffalo, Buffalo, New York, USA*
- ¹⁶³*Northeastern University, Boston, Massachusetts, USA*
- ¹⁶⁴*Northwestern University, Evanston, Illinois, USA*
- ¹⁶⁵*University of Notre Dame, Notre Dame, Indiana, USA*
- ¹⁶⁶*The Ohio State University, Columbus, Ohio, USA*
- ¹⁶⁷*Princeton University, Princeton, New Jersey, USA*
- ¹⁶⁸*University of Puerto Rico, Mayaguez, Puerto Rico, USA*
- ¹⁶⁹*Purdue University, West Lafayette, Indiana, USA*
- ¹⁷⁰*Purdue University Northwest, Hammond, Indiana, USA*
- ¹⁷¹*Rice University, Houston, Texas, USA*
- ¹⁷²*University of Rochester, Rochester, New York, USA*

- ¹⁷³*The Rockefeller University, New York, New York, USA*
¹⁷⁴*Rutgers, The State University of New Jersey, Piscataway, New Jersey, USA*
¹⁷⁵*University of Tennessee, Knoxville, Tennessee, USA*
¹⁷⁶*Texas A&M University, College Station, Texas, USA*
¹⁷⁷*Texas Tech University, Lubbock, Texas, USA*
¹⁷⁸*Vanderbilt University, Nashville, Tennessee, USA*
¹⁷⁹*University of Virginia, Charlottesville, Virginia, USA*
¹⁸⁰*Wayne State University, Detroit, Michigan, USA*
¹⁸¹*University of Wisconsin—Madison, Madison, Wisconsin, USA*
¹⁸²*An institute or international laboratory covered by a cooperation agreement with CERN*

^aDeceased.

^bAlso at Yerevan State University, Yerevan, Armenia.

^cAlso at TU Wien, Vienna, Austria.

^dAlso at Institute of Basic and Applied Sciences, Faculty of Engineering, Arab Academy for Science, Technology and Maritime Transport, Alexandria, Egypt.

^eAlso at Université Libre de Bruxelles, Bruxelles, Belgium.

^fAlso at Universidade Estadual de Campinas, Campinas, Brazil.

^gAlso at Federal University of Rio Grande do Sul, Porto Alegre, Brazil.

^hAlso at UFMS, Nova Andradina, Brazil.

ⁱAlso at University of Chinese Academy of Sciences, Beijing, China.

^jAlso at Nanjing Normal University, Nanjing, China.

^kAlso at The University of Iowa, Iowa City, Iowa, USA.

^lAlso at University of Chinese Academy of Sciences, Beijing, China.

^mAlso at Another institute or international laboratory covered by a cooperation agreement with CERN.

ⁿAlso at Suez University, Suez, Egypt.

^oAlso at British University in Egypt, Cairo, Egypt.

^pAlso at Purdue University, West Lafayette, Indiana, USA.

^qAlso at Université de Haute Alsace, Mulhouse, France.

^rAlso at Department of Physics, Tsinghua University, Beijing, China.

^sAlso at The University of the State of Amazonas, Manaus, Brazil.

^tAlso at Erzincan Binali Yildirim University, Erzincan, Turkey.

^uAlso at University of Hamburg, Hamburg, Germany.

^vAlso at RWTH Aachen University, III. Physikalisches Institut A, Aachen, Germany.

^wAlso at Isfahan University of Technology, Isfahan, Iran.

^xAlso at Bergische University Wuppertal (BUW), Wuppertal, Germany.

^yAlso at Brandenburg University of Technology, Cottbus, Germany.

^zAlso at Forschungszentrum Jülich, Juelich, Germany.

^{aa}Also at CERN, European Organization for Nuclear Research, Geneva, Switzerland.

^{bb}Also at Institute of Physics, University of Debrecen, Debrecen, Hungary.

^{cc}Also at Institute of Nuclear Research ATOMKI, Debrecen, Hungary.

^{dd}Also at Universitatea Babeș-Bolyai—Facultatea de Fizica, Cluj-Napoca, Romania.

^{ee}Also at Physics Department, Faculty of Science, Assiut University, Assiut, Egypt.

^{ff}Also at Karoly Robert Campus, MATE Institute of Technology, Gyongyos, Hungary.

^{gg}Also at HUN-REN Wigner Research Centre for Physics, Budapest, Hungary.

^{hh}Also at Faculty of Informatics, University of Debrecen, Debrecen, Hungary.

ⁱⁱAlso at Punjab Agricultural University, Ludhiana, India.

^{jj}Also at UPES—University of Petroleum and Energy Studies, Dehradun, India.

^{kk}Also at University of Visva-Bharati, Santiniketan, India.

^{ll}Also at University of Hyderabad, Hyderabad, India.

^{mm}Also at Indian Institute of Science (IISc), Bangalore, India.

ⁿⁿAlso at Indian Institute of Technology (IIT), Mumbai, India.

^{oo}Also at IIT Bhubaneswar, Bhubaneswar, India.

^{pp}Also at Institute of Physics, Bhubaneswar, India.

^{qq}Also at Deutsches Elektronen-Synchrotron, Hamburg, Germany.

^{rr}Also at Department of Physics, Isfahan University of Technology, Isfahan, Iran.

^{ss}Also at Sharif University of Technology, Tehran, Iran.

^{tt}Also at Department of Physics, University of Science and Technology of Mazandaran, Behshahr, Iran.

^{uu}Also at Helwan University, Cairo, Egypt.

^{vv}Also at Italian National Agency for New Technologies, Energy and Sustainable Economic Development, Bologna, Italy.

- ^{ww} Also at Centro Siciliano di Fisica Nucleare e di Struttura Della Materia, Catania, Italy.
- ^{xx} Also at Università degli Studi Guglielmo Marconi, Roma, Italy.
- ^{yy} Also at Scuola Superiore Meridionale, Università di Napoli 'Federico II', Napoli, Italy.
- ^{zz} Also at Fermi National Accelerator Laboratory, Batavia, Illinois, USA.
- ^{aaa} Also at Università di Napoli 'Federico II', Napoli, Italy.
- ^{bbb} Also at Ain Shams University, Cairo, Egypt.
- ^{ccc} Also at Consiglio Nazionale delle Ricerche—Istituto Officina dei Materiali, Perugia, Italy.
- ^{ddd} Also at Riga Technical University, Riga, Latvia.
- ^{eee} Also at Department of Applied Physics, Faculty of Science and Technology, Universiti Kebangsaan Malaysia, Bangi, Malaysia.
- ^{fff} Also at Consejo Nacional de Ciencia y Tecnología, Mexico City, Mexico.
- ^{ggg} Also at IRFU, CEA, Université Paris-Saclay, Gif-sur-Yvette, France.
- ^{hhh} Also at Faculty of Physics, University of Belgrade, Belgrade, Serbia.
- ⁱⁱⁱ Also at Trincomalee Campus, Eastern University, Sri Lanka, Nilaveli, Sri Lanka.
- ^{jjj} Also at Saegis Campus, Nugegoda, Sri Lanka.
- ^{kkk} Also at INFN Sezione di Pavia, Università di Pavia, Pavia, Italy.
- ^{lll} Also at National and Kapodistrian University of Athens, Athens, Greece.
- ^{mmm} Also at Ecole Polytechnique Fédérale Lausanne, Lausanne, Switzerland.
- ⁿⁿⁿ Also at Universität Zürich, Zurich, Switzerland.
- ^{ooo} Also at Stefan Meyer Institute for Subatomic Physics, Vienna, Austria.
- ^{ppp} Also at Laboratoire d'Annecy-le-Vieux de Physique des Particules, IN2P3-CNRS, Annecy-le-Vieux, France.
- ^{qqq} Also at Near East University, Research Center of Experimental Health Science, Mersin, Turkey.
- ^{rrr} Also at Konya Technical University, Konya, Turkey.
- ^{sss} Also at Izmir Bakircay University, Izmir, Turkey.
- ^{ttt} Also at Adiyaman University, Adiyaman, Turkey.
- ^{uuu} Also at Istanbul Gedik University, Istanbul, Turkey.
- ^{vvv} Also at Necmettin Erbakan University, Konya, Turkey.
- ^{www} Also at Bozok Universitetesi Rektörlüğü, Yozgat, Turkey.
- ^{xxx} Also at Marmara University, Istanbul, Turkey.
- ^{yyy} Also at Milli Savunma University, Istanbul, Turkey.
- ^{zzz} Also at Kafkas University, Kars, Turkey.
- ^{aaaa} Also at Hacettepe University, Ankara, Turkey.
- ^{bbbb} Also at Istanbul University—Cerrahpasa, Faculty of Engineering, Istanbul, Turkey.
- ^{cccc} Also at Ozyegin University, Istanbul, Turkey.
- ^{dddd} Also at Vrije Universiteit Brussel, Brussel, Belgium.
- ^{eeee} Also at School of Physics and Astronomy, University of Southampton, Southampton, United Kingdom.
- ^{ffff} Also at University of Bristol, Bristol, United Kingdom.
- ^{gggg} Also at IPPP Durham University, Durham, United Kingdom.
- ^{hhhh} Also at Monash University, Faculty of Science, Clayton, Australia.
- ⁱⁱⁱⁱ Also at Università di Torino, Torino, Italy.
- ^{jjjj} Also at Bethel University, St. Paul, Minnesota, USA.
- ^{kkkk} Also at Karamanoğlu Mehmetbey University, Karaman, Turkey.
- ^{llll} Also at California Institute of Technology, Pasadena, California, USA.
- ^{mmmm} Also at United States Naval Academy, Annapolis, Maryland, USA.
- ⁿⁿⁿⁿ Also at University of Florida, Gainesville, Florida, USA.
- ^{oooo} Also at Bingol University, Bingol, Turkey.
- ^{pppp} Also at Georgian Technical University, Tbilisi, Georgia.
- ^{qqqq} Also at Sinop University, Sinop, Turkey.
- ^{rrrr} Also at Erciyes University, Kayseri, Turkey.
- ^{ssss} Also at Texas A&M University at Qatar, Doha, Qatar.
- ^{tttt} Also at Kyungpook National University, Daegu, Korea.
- ^{uuuu} Also at Yerevan Physics Institute, Yerevan, Armenia.
- ^{vvvv} Also at Imperial College, London, United Kingdom.
- ^{wwww} Also at Institute of Nuclear Physics of the Uzbekistan Academy of Sciences, Tashkent, Uzbekistan.